1-1-1991

A spectroscopic study of three FU Orionis objects : accretion disks and wind signatures.

Alan David Welty
University of Massachusetts Amherst

A SPECTROSCOPIC STUDY OF THREE FU ORIONIS OBJECTS: ACCRETION DISKS AND WIND SIGNATURES

A Dissertation Presented

by

ALAN DAVID WELTY

Submitted to the Graduate School of the
University of Massachusetts in partial fulfillment
of the requirements for the degree of

DOCTOR OF PHILOSOPHY

February 1991

Department of Physics and Astronomy

A SPECTROSCOPIC STUDY OF THREE FU ORIONIS OBJECTS:

ACCRETION DISKS AND WIND SIGNATURES

A Dissertation Presented

by

ALAN DAVID WELTY

Approved as to style and content by:

Stephen E. Strom, Chairman

Suzan Edwards, Member

Ronald L. Snell, Member

David Van Blerkom, Member

Robert V. Krotkov, Outside Member

Robert B. Hallock, Department Head
Department of Physics and Astronomy

to my family

Emily, Daniel, and Andrew

ACKNOWLEDGMENTS

Many people have contributed to this work in many ways.

In the broader context of my life, it seems that my mother, Miriam Szanyi, has been an important player. She brought me into the world and gave me direction in life. Her criticism was always constructive. She was always encouraging.

My reasons for becoming an astronomer, other than childhood interest, are something of a mystery to me. However, it is probably more than just coincidence that my choice of career is the same as that of my older brother Daniel, whom I look up to in many ways.

I had the good fortune to have a series of excellent math and science teachers in junior and senior high school in Bethlehem, PA. Mr. Checkley, Mr. Jackson, Mr. Nemeth, Mr. Wetcher, Mrs. Buzzard, and, in particular, Miss Helms gave me a vision that math and science are interesting, important, and fun.

My early education in astronomy was given to me by Stewart Sharpless and Judy Pipher, at the University of Rochester. Jack Fix and Bob Mutel, of the University of Iowa, built on that foundation and gave me needed encouragement. I didn't embarrass myself the *first* time...

The rumors were such that I should be indebted to the Department of Physics and Astronomy of the University of Iowa for its part in making possible my move to Massachusetts, and the opportunity to work with people here. True or not, I have a feeling that it didn't matter in my case.

Thanks are due to the Kitt Peak support staff for their efforts toward productive observing runs at the Mayall telescope, and to the IRAF group for a wonderful product. The secretarial staff at UMass was also very helpful and cheerful during my years here.

The students and faculty of the Five College Astronomy Department have left their mark on this document. The title page and abstract heading would not have been the same without them. It seems a small price to pay for the fond memories and friendships. In particular,

Pat Knezek and Lynne Hillenbrand were terrific office mates, and Diane Dutkevitch gave my ears a reason for being. They and the darts gang (TJ, Jzak, Brothers Ted and James) helped me retain some sanity.

Conversations with Karen Strom, Ron Snell, and David Van Blerkom, whether about this work or other topics dear to their hearts, were always useful and enjoyable. These individuals contribute greatly to the wonderful overall character of the astronomy department at UMass.

Input and encouragement from Lee Hartmann and Scott Kenyon of the Center for Astrophysics, Suzan Edwards of the FCAD/Smith College, and Steve Strom of the FCAD/UMass were essential for the completion of this work. They provided superb examples for a young astronomer to follow, and much free entertainment.

Steve Strom deserves special recognition and thanks for his involvement. A dream of mine, to be involved in star formation research, had been all but lost. He revived the dream, helped enormously in making it a reality, and paid me for it for more than three years. Through it all he was patient and understanding, and able to motivate me. He saw me as more than just a laborer. He thought of my needs, and the needs of my family, and acted accordingly. His example and his friendship will always be special to me.

The heroic endurance of my wife, Emily, through six years of being married to a graduate student, cannot go unrecognized. She has held up under the burden, one much heavier than she expected. Through it all she supplied me with love and strength to keep going. And she brought our two beautiful boys into the world.

ABSTRACT

A SPECTROSCOPIC STUDY OF THREE FU ORIONIS OBJECTS:
ACCRETION DISKS AND WIND SIGNATURES

FEBRUARY 1991

ALAN DAVID WELTY, B.S., UNIVERSITY OF ROCHESTER

M.S., UNIVERSITY OF IOWA

Ph.D., UNIVERSITY OF MASSACHUSETTS

Directed by: Professor Stephen E. Strom

It has been suggested that in outburst, FU Ori objects (FUors) are luminous accretion disks surrounding young, low luminosity stars. We obtained high resolution, high signal-to-noise, 3985–4920 Å, 4940–6830 Å, and 8030–9510 Å spectra of V1057 Cyg, Z CMa, and FU Ori at the Mayall telescope at KPNO to examine predictions of the accretion disk model of Kenyon, Hartmann, and Hewett (1988).

Synthetic disk spectra are calculated assuming the temperature gradient, $T(R)$, of a classical accretion disk, and assuming that disk photospheres can be modeled by adding contributions from concentric disk annuli represented by spectra of supergiant stars having $T_{eff} \approx T(R)$. Given the simplicity of the model, we find surprising agreement between observed and synthetic spectra.

We examine variation of absorption linewidth with wavelength for synthetic and FUor spectra, and find good correlations for the model and two FUors. We also investigate variation of linewidth with lower excitation potential, and find a subtle effect, less useful as a disk diagnostic.

We subtract synthetic spectra from object spectra to investigate overall goodness of fit. For V1057 Cyg and Z CMa, the percentage of lines fit to $\lesssim 10$ mÅ accuracy rises from $\sim$50% at 4000 Å to $\gtrsim$80% at 5000–6800 Å. At 8000–9000 Å, the goodness of fit is $\sim$50%;

the decline attributed to disk flaring. For FU Ori, the goodness of fit is ~10% at 4000 Å, rising to ~80% longward of 5700 Å.

We examine residual features in V1057 Cyg and Z CMa. Most of the strongest features are either emission or P Cygni lines, suggesting origin in powerful winds driven by these objects. For FU Ori, most residuals are absorption features, as expected if FU Ori has lower surface gravity than do supergiants, or if wind absorption is particularly strong.

The signal-to-noise ratio in Z CMa's residual spectrum is sufficient to examine the P Cygni structure in lines of a large range of optical depths. We leave detailed analysis to a subsequent paper, but point here to unusual line structure that may arise in a rotating wind, suggesting that FUor winds carry large amounts of angular momentum.

TABLE OF CONTENTS

LIST OF TABLES

LIST OF FIGURES

CHAPTER 1

INTRODUCTION

The FU Orionis Phenomenon

During the five decades since the 1936 flare-up of FU Ori, a variety of explanations for that event, and similar ones, have been proposed. Herbig (1966) was apparently the first to suggest that the dramatic increase in brightness was intrinsic to FU Ori itself, rather than removal of obscuration from our line of sight. Because FU Ori was not observed adequately either before or immediately after its outburst, and because it was a unique object, efforts directed toward understanding its nature were necessarily limited. This situation has changed dramatically during the past two decades. About a half dozen more FU Ori objects, or "FUors," have been identified (Welin 1971a; Grasdalen 1973; Herbig 1977; Elias 1978; Graham and Frogel 1985; Carr, Harvey, and Lester 1986; Mundt *et al.* 1985; Stocke *et al.* 1988; Hartmann *et al.* 1989; Eislöffel, Hessman, and Mundt 1990). Table 1 lists these objects, their (recent) V magnitudes, and 1950 coordinates. It is now generally accepted that FU Ori eruptions are intrinsic to pre–main-sequence objects, and constitute an important phase of early stellar evolution, but are *not* primarily changes in the forming stars themselves. The currently popular scenario suggests that FU Ori eruptions are accretion events in *circumstellar disks*. To understand this evolution in thinking, it is instructive first to review the early observations of the two most studied members of the class (to be studied here also): FU Orionis and V1057 Cygni. We will also briefly review observations of our third program object, Z Canis Majoris.

Early Observations of FU Orionis

FU Ori, a pre–main-sequence object in the dark cloud B35, which is part of the λ Ori star-forming complex, had been an irregular variable, with a typical full amplitude of $1.1 m_{pg}$,

Table 1. FU Orionis object V magnitudes and epoch 1950 coordinates. The following objects comprise the FU Ori class of objects. Magnitudes and coordinates are as given in the respective discovery papers, or Herbig and Bell (1988), whichever data are more recent. No V magnitude is given for L1551 IRS 5, which is an optically invisible object.

Name	V	α	δ
FU Ori	9.24	05 42 38.0	+09 03 03
V1057 Cyg	11.70	20 57 06.2	+44 03 46
V1515 Cyg	12.56	20 22 03.2	+42 02 40
V1735 Cyg	18.5	21 45 26.9	+47 18 08
V346 Nor	16.3	16 28 56.8	−44 49 08
Z CMa	9.35	07 01 22.5	−11 28 36
BBW 76	12.41	07 48 40.3	−32 58 43
L1551 IRS 5		04 28 40.0	+18 01 52

as judged from Harvard Patrol plates, when in 1936 it began its increase in brightness of six magnitutes (photographic), from ∼16 to 9.7, in a period of two to nine months (Hoffleit 1939), probably close to 120 days (Herbig 1966). The post-maximum B magnitude light curve published by Herbig (1977, Figure 1, and references therein) shows the following behavior. After remaining near maximum light for two years, there was a sudden (∼90 day) fading of ∼1 mag, followed by slow oscillation (Δt ∼10 yr, Δm ∼0.5 mag) that ended by 1960. Over the next fifteen years, FU Ori faded another 0.2 mag. By 1985, the B magnitude was 10.57 (Herbig and Bell 1988, and references therein). Thus it appears FU Ori has faded at an average rate of ∼0.16 mag/decade, but is still ∼5.5 magnitudes brighter than its pre-outburst brightness.

The FU Ori discovery announcement (Wachmann 1939) mentioned fan-shaped nebulosity that had not been present before the outburst. The earliest published post-outburst large scale photograph of the nebula, which shows the nebula essentially the same as in more recent photographs, was taken 2.1 years after the outburst (Dieckvoss 1939, Herbig 1966). It shows nebulosity extending 2.′5 from FU Ori, consistent with the plane-of-sky light travel time of 2.′1 yr^{-1}, assuming a distance of 500 parsecs to the λ Ori region. Herbig (1977) noted that a partial ring of nebulosity is also present.

Early (1962 and 1963) blue and red spectrograms of FU Ori revealed a composite spectrum: a "diffuse" component at the velocity of the surrounding interstellar material, and narrower "shell" features displaced to shorter wavelengths by $\sim 80\,\mathrm{km\,s^{-1}}$. The diffuse component, presumed to originate in a stellar photosphere, was assigned an F2:p I–II spectral type. The peculiarity arose from the observation that Cr I and Al I lines were too weak for that type. Shell components were strong in Ca I and Ca II, Na I, Cr I, Sr II, Ti II, Sc II, and low excitation Fe I lines. The Balmer and Na I D lines were particularly strong in the shell component, and extended to greater blue-shifted velocities (Herbig 1966). Based on the persistence of the shell features, Grasdalen (1973) argued that they are signatures of continuous mass loss, rather than discrete ejection episodes.

In view of the currently accepted model for FUors in the post-outburst state, Grasdalen (1973), discussing the presumed rotational widths of the photospheric lines, made the following historically interesting remark: "The disturbing point is that, at least for FU Ori, the breadth of the lines depends on wavelength..." While he did not specify the sense or origin of the wavelength variation of linewidth, which may have changed in detail since the first few years after outburst, variation of linewidth with wavelength has become the linch-pin for the accretion disk hypothesis for FU Ori objects.

The Outburst and Evolution of V1057 Cygni

In 1957 Herbig (1958) discovered many emission-Hα stars in the H II region NGC 7000 (the North America Nebula) in Cygnus. Among these was Lk Hα 190, a star roughly centered in a small dark cloud in the nebula. Subsequent observations revealed (Wenzel 1963) and confirmed (Robinson and Harwood 1971, Welin 1971b) irregular light variations; the star was designated V1057 Cyg in the *General Catalog of Variable Stars* (Kukarkin *et al.* 1969). Believed to be a T Tauri star (TTS) based on one low dispersion spectrogram (Herbig 1958), the irregular variability (amplitude $\sim 1.1 m_{pg}$), and intimate association with other pre–main-sequence objects, V1057 Cyg became the second known FUor in 1969, reaching maximum

light in mid-1970. It remains the only FU Ori object for which there is significant knowledge of the pre-outburst state.

The eruption of V1057 Cyg was almost as dramatic as that of FU Ori. In about one year, it increased by ~5.5 magnitudes in the photographic band (Welin 1971a). Unlike FU Ori, which has remained close to maximum light for more than fifty years, V1057 Cyg has faded more rapidly. From early 1971 to 1986, its V magnitude has dimmed by ~2.3 mag, but has remained at ~11.7 since that time (Kenyon 1989, private communication).

Like FU Ori, V1057 Cyg developed a reflection nebula shortly after the outburst (Welin 1971a). The time development of the nebula was not observed here either, and we can only use the initial observation to place an upper limit for the distance to V1057 Cyg at 900 pc (Grasdalen 1973). Grasdalen (1973) also derived a distance of 575 pc by plotting color excess *vs.* distance modulus for stars near the line of sight to V1057 Cyg. A sharp increase in color excess, attributed to the cloud material, was seen at a distance modulus of ~8.8. This value is still in common use in the literature (*e. g.*, KHH).

The pre-outburst spectrum of V1057 Cyg was suggestive of a late-type T Tauri star (Herbig 1958). A blue spectrum taken by Welin at roughly maximum light revealed a very different situation. It, and others taken a few months after, show an early A type, high luminosity object. Two years later, the blue spectral type had changed to early F (Herbig 1977), and currently is late F to early G. Herbig (1977) also noticed that spectral types determined from red (6000–6600 Å) spectrograms, while concurring with the blue in indicating cooling with time, were consistently later than in the blue region by roughly one spectral class.

Absorption line radial velocities also showed a curious wavelength dependent effect. The metallic lines from the first blue spectrograms of early 1971 showed a large negative velocity, -40 to $-50\,\mathrm{km\,s^{-1}}$ (heliocentric). The radial velocity shifted toward $-20\,\mathrm{km\,s^{-1}}$ during the 1971 observing season, and stabilized at $\sim -13\,\mathrm{km\,s^{-1}}$ by 1973. During this period and through 1975 the red region radial velocity showed only a scatter around $-15\,\mathrm{km\,s^{-1}}$

(Herbig 1977). The heliocentric velocity determined from our spectra (1986 Oct, 1986 Dec, 1988 Nov, and 1989 Dec) are $\sim -15\,\mathrm{km\,s^{-1}}$ at all optical wavelengths. Molecular (Lo and Bechis 1974, Bechis and Lo 1975, Minn and Greenberg 1973) and Hα (Hippelein 1973) line studies indicate that the surrounding interstellar material is at about the same velocity.

Observations of Z Canis Majoris

The observed history of Z CMa is different than for FU Ori and V1057 Cyg in that no $\gtrsim$5 mag optical outburst has been observed. It has exhibited irregular optical variability with a range of $\sim$2 mag (Covino *et al.* 1984). Its membership in the FU Ori class is based on spectroscopic similarities to other FUors. These similarities include strong blue-shifted Balmer and Na I D absorption features (Finkenzeller and Jankovics 1984, Finkenzeller and Mundt 1984), doubled absorption profiles (Hartmann *et al.* 1989), and the presence of 2.3 μm first-overtone v'–v'' = 2–0 CO absorption.

An arc, or partial ring of nebulosity similar to those associated with other FUors, is seen in images of Z CMa (see Poetzel, Mundt, and Ray 1989). Recently, bipolar outflow from Z CMa, indicated by a jet and string of 15 Herbig-Haro objects, has been discovered (Poetzel, Mundt, and Ray 1989).

Z CMa was formerly classified as an Ae/Be star, whose spectrum seemed to have late B and F type components (Strom *et al.* 1972). The B type component depended on the great strength of the Balmer absorption lines, which are certainly formed in an outflowing wind (Covino *et al.* 1984), and on the presence of He I absorption lines not found by other observers (*e.g.*, Herbig 1960, Covino *et al.* 1984, Finkenzeller and Jankovics 1984, and Finkenzeller and Mundt 1984). Hartmann *et al.* (1989) estimate an F5 I spectral type for the 2650 Å region based on *IUE* spectra, consistent with other FUors in outburst.

As with FU Ori and V1057 Cyg, Z CMa absorption line radial velocities ($\sim +30\,\mathrm{km\,s^{-1}}$, heliocentric, Hartmann *et al.* 1989) are nearly the same as neighboring interstellar material ($\sim +32\,\mathrm{km\,s^{-1}}$ from CO, Edwards and Snell 1982, Cantó *et al.* 1984; 30–33 $\mathrm{km\,s^{-1}}$ from

interstellar Na I D absorption, Finkenzeller and Mundt 1984). The pre–main-sequence nature of Z CMa is confirmed by this kinematic association with diffuse interstellar material and a strong λ6707 Å absorption line.

Characteristics of the FU Ori Objects

Now that there is a small *class* of FU Ori objects, we can identify characteristics which seem to be common to all members. Those properties include: association with known star-forming regions; strong Li λ6707.7 Å line; doubled absorption line profiles; P Cygni structure in the Balmer and Na I D lines, with absorption edges blue-shifted several hundred $km\,s^{-1}$; earlier spectral type in the optical (F–G) than in the near-infrared (M, based on 2.3 μm first-overtone v'–v'' = 2–0 CO absorption); and the development of ring-shaped reflection nebulae. Goodrich (1987) has reviewed observations of the reflection nebulae associated with the Cygnus region FU Ori objects. A large luminosity increase, the original identifying characteristic, has not been observed for every FU Ori object. In these cases, membership in the class is based on similarities in the spectral characteristics listed here. Details of the respective eruptions are given, if known, in Table 2.

Table 2. Outburst data for the FU Orionis objects. For several objects, outburst information must be determined from sparce photographic plate data, hence the limits present in the table. For some, no outburst has been observed; membership for these objects is based on spectroscopic similarities. Data is from Herbig (1989).

Object	Date of Maximum	Magnitude change	Rise time (days)	Note
FU Ori	1937	6 (pg)	60–380	
V1057 Cyg	1970	5.5 (pg)	390	
V1515 Cyg	1980?	~4 (pg)	<4750	
V1735 Cyg	>1957, <1965	>5 (R)	?	Elias 1-12
V346 Nor	>1984	>2 (V)	≥2555	HH-57 IRS 8
Z CMa	?	?	?	
BBW 76	>1956	?	?	
L1551 IRS 5	?	?	?	

The FU Ori objects drive extremely powerful, high velocity winds. Poetzel, Mundt, and Ray (1990) discovered a series of Herbig-Haro objects and a jet with velocities up to $-620\,\mathrm{km\,s^{-1}}$ associated with Z CMa. Hα profiles of FU Ori, V1057 Cyg, and Z CMa appear in Figure 1, showing blue absorption wings extending to about $-400\,\mathrm{km\,s^{-1}}$, $-800\,\mathrm{km\,s^{-1}}$, and $-1100\,\mathrm{km\,s^{-1}}$, respectively, at the time of our observations (1988 November). Analysis and modeling of the Na I D lines suggests mass loss rates, $\dot{M}$, $\sim 10^{-5} M_\odot\,\mathrm{yr^{-1}}$ for FU Ori, $\sim 10^{-6} M_\odot\,\mathrm{yr^{-1}}$ for V1057 Cyg (Croswell, Hartmann, and Avrett 1987), and $\gtrsim 10^{-5} M_\odot\,\mathrm{yr^{-1}}$ for Z CMa (Hartmann *et al.* 1989). Mass loss rates inferred from strong Hα lines in T Tauri stars ($W_\lambda(\mathrm{H}\alpha) \gg 5$ Å) are typically only $\lesssim 10^{-8}$ to $10^{-7} M_\odot\,\mathrm{yr^{-1}}$ (Hartmann *et al.* 1990, Natta, Giovanardi, and Palla 1988). Herbig's (1966) "shell" lines, many of which are still present, are blue-shifted with respect to the presumed stellar velocity (by $\sim 80\,\mathrm{km\,s^{-1}}$ in FU Ori), and are probably associated with this mass loss.

Although no FUor has been seen to erupt more than once, reasonable arguments can be made that FU Ori events are repetitive. During the past century, at least 6 FU Ori outbursts have occured within about 1 kpc of the Sun, yielding a lower limit to the eruption rate of $0.06\,\mathrm{yr^{-1}}$. If we assume that all FU Ori objects were TTS brighter than $M_{pg} \sim 4$ before outburst (Herbig 1977), and use Herbig's estimate that $\sim$500 such objects exist within 1 kpc, it is estimated that each of those objects will have erupted once after $\lesssim$8300 years. Assuming a lifetime of 3×10^5 years for the candidate objects, each would be required to erupt 36 times to sustain the observed rate of detection (Herbig 1989).

Alternatively, if we assume that all new-born low mass ($M \lesssim 2.5 M_\odot$) stars may experience FU Ori outbursts, and consider the average star formation rate in the solar neighborhood ($\sim 4 - 10 \times 10^{-9}$ stars $\mathrm{pc^{-2}\,yr^{-1}}$, Miller and Scalo 1979), we can estimate eruption frequencies required to support the observed eruption rate for any mass range. We find results consistent with that above if we consider only the mass range included above ($\sim$1.5 to $\sim$2.5 $M_\odot$; Herbig 1989), and conclude that FU Ori eruptions must be repetetive in any case: even

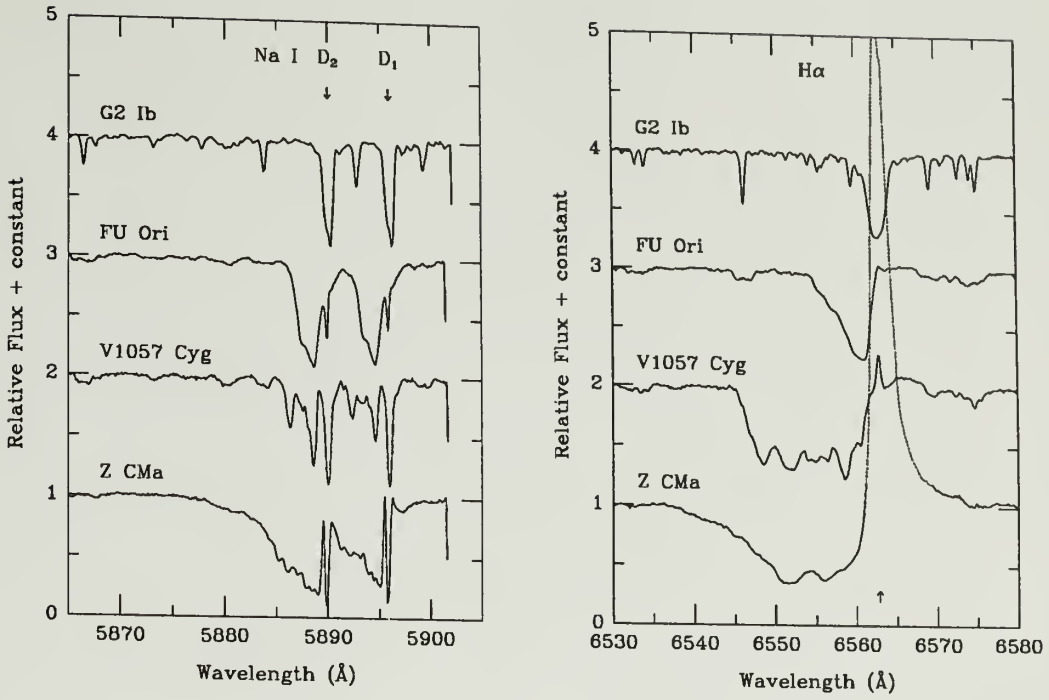

Figure 1. Na I D and Hα lines in FU Ori, V1057 Cyg, and Z CMa. The Na I D lines have been analyzed by Croswell, Hartmann, and Avrett (1987) and Hartmann *et al.* (1989) to estimate mass loss rates for these objects. Components at zero velocity, indicated by arrows, are probably interstellar. The Hα profiles also indicate extensive mass loss, and demonstrate the large velocity attained by the outflowing material. The spectrum of a G2 supergiant is shown in each panel for comparison.

if *all* new-born low mass stars experience FU Ori outbursts, each must erupt an average of ~3 times (Hartmann and Kenyon 1985, HK1 hereafter; Herbig 1989).

Suggested Explanations

During the past 50 years, many explanations for FU Ori events have been suggested. Each was intended to explain existing observations, but as new data were obtained, was found to be inadequate. We will discuss several briefly here. More complete discussion of various suggestions may be found in Herbig (1966, 1977), Grasdalen (1973), and Kenyon, Hartmann, and Hewett (1988, KHH hereafter).

The earliest proposed explanations dealt only with the increase in brightness, since little other data was available. The major ideas in this category were that FU Ori might be a slow nova, or that the star had emerged from an obscuring cloud. The prolonged elevated brightness of FU Ori seemed to rule out the former option (Herbig 1966, and see Payne-Gaposchkin 1957). In the latter case, the only geometrically acceptable situation requires passage through a dense, thin obscuring screen. Such curtains are not known to exist. And this explanation does not explain post-outburst fading of the FUors (Herbig 1966). Grasdalen (1973) argued that rapid clearing of a circumstellar dust shell was highly unlikely.

Another group of suggestions involves dramatic changes in the stars themselves. Among these are Herbig's (1966) suggestion that FU Ori eruptions are due to rapid *collapse* of a proto-star across the forbidden region to the tip of a Hayashi track. Data from before and after the outburst of V1057 Cyg showed that the object *increased* in size during the outburst. Grasdalen (1973) proposed that a structural readjustment of an $8M_{\odot}$ star, ending with the star on its proper radiative-equilibrium track, was responsible for the flare-up of V1057 Cyg. This seems unlikely as the object fades and cools (Herbig 1977). Both ideas are inconsistent with the apparent repetetive nature of the phenomenon.

The observation that optical spectral types of FUors are earlier (F-G) than in the near infrared (M), led Elias (1978) and Mould *et al.* (1978) to suggest that FUors are close binary systems consisting of an M giant orbiting an F–G supergiant, with accretion onto the supergiant producing the outburst. This idea fails because no radial velocity variations expected for a close binary have been detected, and no reasonable mechanism for simultaneous eruption of both stars has been developed.

Larson (1980) suggested that a single star, rotating near break-up could produce variation of spectral type with wavelength, since the bloated equatorial region would be cooler and more rapidly rotating than the polar regions. This scenario will yield a variation of linewidth with wavelength in the opposite sense to that which is observed.

During the past six years, Hartmann and Kenyon and their collaborators have developed a successful model for the post-outburst state of the FU Ori objects. They suggest that an FU Ori outburst is the result of a large increase in the accretion rate through a circumstellar accretion disk (HK1; Hartmann and Kenyon 1987a,b, HK2 and HK3 hereafter; KHH). It is this suggestion that we investigate here.

CHAPTER 2

MOTIVATION AND GOALS

Project Goals

The success of any theory depends on its ability to reproduce and predict observations. Evidence for a key prediction of the accretion disk model, that the radial temperature gradient in the disk and the disk's differential rotation produce an increase of absorption linewidth toward shorter wavelengths (see Chapters 4 and 5 for details), has been observed in FU Ori and V1057 Cyg (HK2, HK3). This is based on cross-correlations of object and model spectra with standard star templates at two wavelengths, 6170 Å and 2.3 μm. Cross-correlations of spectral orders at 5200 Å are much narrower than predicted, though wind components to spectral lines may affect results at short wavelengths (HK2, KHH). Welty *et al.* (1990) presented evidence that the linewidth variation is a *continuous* function of wavelength in V1057 Cyg on the 5820–9300 Å range, in agreement with model prediction.

Conflicting results have been reported for a closely related model prediction, namely, that linewidths should increase with increasing lower excitation potential (see Chapter 4). In his recent review of FU Ori objects, Herbig (1989) cited unpublished spectra in which he found no evidence for such a correlation in FU Ori and V1057 Cyg. Welty *et al.* (1990) have reported detection of this correlation in 12 $\mathrm{km\,s^{-1}}$ resolution echelle spectra of V1057 Cyg, obtained in 1986 October (a $1.16 \pm 0.35\,\mathrm{km\,s^{-1}\,eV^{-1}}$ slope in a 7500–9300 Å spectrum), and 1986 December ($1.10 \pm 0.44\,\mathrm{km\,s^{-1}\,eV^{-1}}$ in a 5820–7640 Å spectrum), in good agreement with model prediction.

The goals of this study are two-fold. The first goal is to compare optical absorption lines predicted by the accretion disk model with observed features. In addition to examining linewidth *vs.* wavelength and linewidth *vs.* excitation potential correlations in greater detail, we will compare line strengths and profiles in synthetic and observed FU Ori object spectra.

A key element of this section will be determination of the best model parameters for each program object (normalization of disk temperature and rotational velocity scales, and radial velocity; see Chapter 4), and acceptable limits on them.

The second goal is to search for spectral features which arise in the FU Ori object winds. To study the wind components in FU Ori object line profiles, we must be able to separate them from the disk contributions. This will be accomplished by subtracting synthetic disk spectra from FU Ori object spectra. If the synthetic disk spectra represented real disk spectra perfectly, these subtractions would leave residual features associated with the wind or any other non-disk components that may be present in the FU Ori systems. Before assuming a residual feature is intrinsic to an FU Ori object, errors in model input parameters (radial and rotational velocities, maximum disk temperature), and sensitivity to physical conditions such as temperature and gravity must be eliminated or accounted for. We will attempt to make use of any residual features that do not appear to suffer from these uncertainties to constrain wind properties. Whether the wind arises from the central star or from the disk itself, is of particular interest.

In recent years there has been growing interest in the notion that winds may arise from disks, rather than from the central stars (*e.g.*, Hartmann and MacGregor 1982, Pudritz and Norman 1983, 1986, Torbett 1984, Uchida and Shibata 1985, Croswell, Hartmann, and Avrett 1987, Shu *et al.* 1988, Pringle 1989). There is evidence that mass loss in T Tauri stars is driven by accretion through circumstellar disks (Cabrit *et al.* 1990). The FU Ori objects, with copious mass loss, and presumably correspondingly large accretion rates, may prove to be an ideal laboratory for investigating this possibility.

Further Motivation

While the accretion disk model for FU Ori objects has gained wide acceptance in the astronomical community, there is reason to continue developing and augmenting it. Until all relevant observations can be satisfactorily accommodated in the theory, it must be regarded

as incomplete. Here we briefly discuss some of the points the model has not adequately addressed. Unless otherwise noted, we will not address these concerns further at this time.

It has been pointed out by Simon and Joyce (1988) that, as V1057 Cyg fades, its infrared magnitudes are not behaving according to model prediction, which says the infrared spectral index should remain constant (*i.e.*, $\lambda F_\lambda \propto \lambda^{-\alpha}, \alpha = 4/3$, should remain true), provided classical viscous accretion disk theory adequately describes the radial temperature gradient, $T(R)$, in the disk, and such accretion remains the dominant source of luminosity. The observations show that the decline has been slower at longer wavelengths. This could simply be the growing relative importance of another source of infrared luminosity, having a different α, as the disk fades. Non-steady accretion, variation of accretion rate with radius in the disk, could also be responsible.

If the FU Ori objects are luminous rotating circumstellar disks, any absorption lines produced in their "photospheres" should possess doubled profiles, owing to the geometry involved. If we imagine the disk as a series of concentric annuli, the largest contributions to the spectrum from each annulus are from the approaching and receding ansae. The duplicity as observed seems to depend on wavelength and line strength, especially in FU Ori and V1057 Cyg (HK2, KHH). There is also evidence (Herbig 1989) that the relative strengths of the two peaks in some doubled profiles are not constant.

Perhaps the most serious concern comes from ultraviolet observations of FU Ori objects. Ultraviolet and optical luminosity equal to the infrared disk luminosity should be emitted by a "boundary layer" between the rapidly rotating ($v_{rot} \sim 250\,\mathrm{km\,s^{-1}}$) inner disk and the presumably more slowly rotating stellar surface (Typical T Tauri star rotational velocities are $\lesssim 25\,\mathrm{km\,s^{-1}}$ [Hartmann *et al.* 1986].). Hartmann *et al.* (1989) report that observed ultraviolet fluxes fall short of those expected for a classical boundary layer by at least an order of magnitude in FU Ori and V1057 Cyg. If the central stars have been spun-up and are rotating near break-up, boundary layer emission would not be expected. This would seem to require

repeated spin-up and spin-down if they are T Tauri stars with disks that experience *multiple* FU Ori outbursts.

In view of the pre–main-sequence status of the FU Ori objects and arguments for the repetitive nature of their outbursts, understanding the physical processes responsible for their peculiar characteristics will continue to be very important in star-formation studies. If, as appears to be the case, the FU Ori eruptions are accretion events in T Tauri star disks, the tremendous accretion rates implied suggest that a significant portion of the final stellar mass is accumulated during these episodes. Whatever the nature of FU Ori outbursts, the powerful winds generated deposit large amounts of energy in, and may therefore have a significant impact on the immediate environment of the forming star (Herbig 1977, KHH). Further study, aimed at determining the applicability of the accretion disk hypothesis to the FU Ori objects and determining better constraints on such models, seems warranted.

CHAPTER 3

OBSERVATIONS AND DATA REDUCTION

Program Requirements

The data required to achieve the goals stated in Chapter 2 must meet several requirements. The spectra must be of adequate spectral resolution, must be characterized by high signal-to-noise ratio (SNR), and must offer relatively complete wavelength coverage over a broad range of wavelength.

Specifically, to obtain useful measurements of linewidths, and to allow adequate analysis of potential residual features, several resolution elements must span each absorption line. In the sample to be discussed here, the object whose absorption lines are narrowest, V1057 Cyg, has an implied rotational velocity, $v \sin i \sim 35\,\mathrm{km\,s^{-1}}$, at optical wavelengths (HK2). Resolution of $\lesssim 15\,\mathrm{km\,s^{-1}}$ would provide five or more resolution elements for each line in the object spectra.

Visual comparison of the data and models of Hartmann and Kenyon (HK2, HK3, KHH) suggests that residual features in difference spectra (object minus model) may appear at the 5% level. A signal-to-noise ratio of ~200 would thus provide a SNR ~10 in the residual features. It should also be noted that Welty *et al.* (1990) attribute much of the scatter in their linewidth *vs.* wavelength and linewidth *vs.* excitation potential plots to the noise in their SNR ~100 data, which are otherwise similar to the data obtained for this work (see below).

Broad wavelength coverage is required for several reasons. A statistically significant number of unblended absorption lines is required for the linewidth *vs.* wavelength and linewidth *vs.* excitation potential tests. The former test also requires a long wavelength baseline for adequate treatment. In the accretion disk models, the wavelength range 4000 Å to 9000 Å corresponds to disk radii from ~1.8 to ~3.1 stellar radii, and probes to some extent the region within ~6 to ~15 stellar radii from the center (see Tables 4 and 5 in Chapter 4).

So we expect, in a Keplerian disk, a decrease of ~24% in linewidth over that wavelength range (see Chapter 5). Should residual features appear in the difference spectra, the presence or lack of wavelength dependent effects will be critical for their interpretation.

Object Selection

The task of selecting objects for this study is manageable, since there are no more than eight recognized FU Ori objects. Some may be eliminated from consideration here for practical reasons. We wish to have spectra obtained with the same instrumentation and methods, to eliminate problems associated with comparing spectra that, for example, do not have identical wavelength coverage and dispersion, especially for the comparison with theoretical models to be discussed in Chapters 4, 5, and 6. Requirements on the nature and quality of data demand that objects be bright. Even for the brightest of these objects (FU Ori itself), the necessary data currently can only be obtained with instrumentation on par with the echelle spectrograph and charge-coupled device detector available at the 4-meter Mayall telescope at the Kitt Peak National Observatory[1]. The impact of the proposed study will be greatest if the objects chosen have a solid record of previous observation, providing a context in which to interpret the data. These constraints dictate, as suggested by the foregoing discussion, that FU Orionis, V1057 Cygni, and Z Canis Majoris be the target objects (see Table 1).

Observations and Data Reduction

Spectra of the desired resolution ($\lesssim 15\,\mathrm{km\,s^{-1}}$), and signal-to-noise ($\gtrsim 200$), can be obtained with the echelle spectrograph and a charge-coupled device (CCD) detector at the Mayall 4-meter telescope at the Kitt Peak National Observatory (KPNO) with integration

[1] Operated by the National Optical Astronomy Observatories, which is operated by the Association of Universities for Research in Astronomy, Inc. (AURA) under cooperative agreement with the National Science Foundation

times of an hour or less per program object. With that instrumentation and desired resolution, observations must be made at three grating settings to cover the 4000–9000 Å range. Spectra of a grid of bright supergiant standard stars, from early F through early M type, required for modeling, can be obtained in a few minutes or less each.

Spectra of FU Ori, V1057 Cyg, Z CMa, and supergiant standards meeting the requirements of this study (see the discussion in Chapter 4) were obtained in 1988 November. Strom and Welty obtained spectra with wavelength coverage of 3985–4920 Å and 8030–9510 Å on 1988 November 19–21. KPNO's TI2 CCD was employed for those observations. Hartmann and Stauffer obtained similar data for this project on the 4940–6830 Å range on 1988 November 30, using KPNO's TI3 CCD. The TI3 CCD chip was used because the TI2 CCD was damaged between the two observing runs. In each case, the UV fast camera was employed, with a 31.6 groove mm^{-1} echelle grating and a 226 groove mm^{-1} cross-disperser, yielding $\sim 12\,km\,s^{-1}$ resolution at all wavelengths observed. A brief log of these observations and other data to be discussed may be found in Table 3.

We did not obtain a 8030–9510 Å spectrum of a rapidly rotating B star, so we are unable to divide out the telluric spectrum, which is significant over much of that region, especially longward of 9000 Å.

Each observing night, in addition to object exposures, various calibration images were obtained. Bias frames were taken to correct for the zero integration time CCD response. Flat-field frames (images obtained by illuminating the spectrograph and detector system with a "bright quartz" lamp) were obtained to correct for pixel-to-pixel variations in CCD sensitivity. Wavelength calibration was obtained by observing the known spectrum of a thorium-argon arc before or after each object exposure. A light-emitting diode was used to pre-flash all exposures to guarantee a background level sufficient to insure linear CCD response at low light levels.

Both the TI2 and the TI3 CCD are 800 × 800 pixel detectors. Each has 0.015 mm pixels, corresponding to 0.38″ on the sky at our decker setting. Our data were binned 2:1

Table 3. Log of FU Ori object observations cited in this work. The 1988 November data are the primary data used herein. Spectra of standard stars were also obtained during each observing run.

Date (UT)	FU Ori	V1057 Cyg	Z CMa
1983 Dec 10			6260–6835 Å[ab]
1983 Dec 12			4720–5330 Å[ab]
1984 Dec 5			6275–6735 Å[a]
1986 Oct 15		7500–9370 Å[ac]	
1986 Dec 15	5820–7580 Å	5820–7580 Å[c]	
1988 Jan 7	5125–6865 Å		
1988 Nov 19	3985–4920 Å		3985–4920 Å
1988 Nov 19	8030–9510 Å[a]		8030–9510 Å[a]
1988 Nov 20		8030–9510 Å[a]	
1988 Nov 21		3985–4920 Å	
1988 Nov 30	4940–6830 Å	4940–6830 Å	4940–6830 Å[d]
1989 Dec 6		4985–6840 Å	4985–6840 Å
1989 Dec 7	4985–6840 Å		
1989 Dec 8	7245–9005 Å[a]	7245–9005 Å[a]	7245–9005 Å[a]

[a] wavelength coverage is not complete
[b] also appears in Hartmann *et al.* (1989)
[c] also appears in Welty *et al.* (1990)
[d] also appears in Hessman *et al.* (1991)

perpendicular to the dispersion axis, yielding 800 × 400 pixel echelle images. This was done primarily to save computer tape and disk space, and has no significant effect on the resultant spectra. Because the echelle orders cross the CCD rows, a sawtooth-like component can easily be introduced into the extracted orders. This problem is potentially more serious for binned data, but can be avoided if extraction task order-following parameters are carefully chosen.

In all cases, the background (sky, scattered solar spectrum) contributes no more than ~5% of the total extracted intensity, except in a number of sharp night sky emission lines (*e.g.*, [O I] and OH lines), and we did not attempt background subtraction. For the 3985–6830 Å data, subtraction of the background is impractical because the narrow decker and 2–3″ seeing left little or no pure background adjacent to the orders. We also wanted to avoid the degradation of signal-to-noise that would be caused by sky subtraction.

The echelle format data were reduced to the final one-dimensional vectors (orders) using the National Optical Astronomy Observatories' Image Reduction and Analysis Facility (IRAF) on the Five College Astronomy Department's Sun386*i* workstations. The CCD images were de-biased and flat-fielded in the usual manner for echelle data. A Thorium-Argon arc spectrum obtained after set-up and before observing provides the absolute wavelength calibration for all exposures and the $0\,\mathrm{km\,s^{-1}}$ reference. The shift between this comparison spectrum and one taken immediately before or after each object exposure, with the telescope pointed at the target, corrects for movement of the CCD detector in its dewar as the telescope moves. We estimate that errors in our shifts between comparison spectra to be $\lesssim 1\,\mathrm{km\,s^{-1}}$. Because the count rates are not important for this work, and due to requirements of the program which calculates model disk spectra, all the object spectral orders were normalized to unit continuum.

The other data to be discussed in the following Chapters (see Table 3) was also obtained with the echelle spectrograph system at the 4-m telescope at Kitt Peak. Minor differences in instrumentation and set up characterized each observing run, and there were trivial differences in reduction techniques. These do not significantly affect the usefulness of any of the data for the present purpose.

CHAPTER 4

ACCRETION DISK MODELING

Background

During the past several years, the suggestion that the FU Ori objects, in the post-outburst state, are luminous accretion disks has gained widespread acceptance in the astronomical community. This acceptance is based largely on evidence presented in a series of papers by Hartmann and Kenyon and their collaborators (*e.g.*, HK1, HK2, HK3, KHH). They show, for FU Ori and V1057 Cyg, that accretion disk models adequately reproduce observed broad-band spectral energy distributions from 4000 Å to $\sim$10 μm, color evolution, spectral features, line profiles, and signatures of differential rotation, and offers natural explanation for the observed variation of spectral type with wavelength.

Method of Model Calculation

The starting point for calculation of synthetic disk spectra begins with the accretion disk formalism developed in the early 1970's by Shakura and Sunyaev (1973) and Lynden-Bell and Pringle (1974, LBP hereafter). In their theory, viscous accretion drives mass and angular momentum transport through a disk. The disk will be self-luminous, deriving energy from the release of gravitational potential energy as material spirals in toward the central object. The total luminosity due to accretion is $L_{acc} = GM_{\star}\dot{M}_{acc}/R_{\star}$, where $M_{\star}$ and $R_{\star}$ are the mass and radius of the central star, respectively, and $\dot{M}_{acc}$ is the mass accretion rate through the disk. Half of this will be radiated by the disk; half is converted to kinetic energy and, if the stellar surface is rotating slowly compared to the inner disk, must ultimately be converted into boundary layer emission.

In this picture, an FU Ori outburst is essentially a dramatic increase in the accretion rate through a circumstellar disk. To match the observed fluxes (see below), the model demands

$\dot{M}_{acc} \sim 10^{-4} M_{\odot} \mathrm{yr}^{-1}$ for objects in outburst (KHH). Accretion rates for T Tauri star disks are estimated to be $\dot{M} \lesssim 10^{-7} M_{\odot}\ \mathrm{yr}^{-1}$ (*e.g.*, Basri and Bertout 1989). The physical mechanism for this proposed increase in accretion rate is not known, but may involve gravitational instability in a massive circumstellar disk ($M_{disk} \lesssim M_{\star}$).

In a steady accretion disk ($\dot{M}_{acc}$ = constant), the energy per unit surface area dissipated at radius R is

$$F_d(R) = \left(\frac{3GM_{\star}\dot{M}_{acc}}{8\pi R_{\star}^3}\right)\left(\frac{R_{\star}}{R}\right)^3\left[1 - \left(\frac{R_{\star}}{R}\right)^{1/2}\right]. \qquad (1)$$

If the energy is radiated locally at the effective temperature, $T_d(R) = [F_d(R)/\sigma]^{1/4}$, this expression provides the temperature, radius relation needed to synthesize the spectrum of a disk (KHH). The maximum temperature in this distribution is given by

$$T_{max} \approx 13{,}000\,\mathrm{K}\left(\frac{M_{\star}}{1M_{\odot}}\right)^{1/4}\left(\frac{\dot{M}_{acc}}{10^{-5}M_{\odot}\mathrm{yr}^{-1}}\right)^{1/4}\left(\frac{R_{\star}}{R_{\odot}}\right)^{-3/4}, \qquad (2)$$

and occurs at $R_{max} = 1.36R_{\star}$ (LBP). Equation (1) implies that the disk temperature declines within this radius, approaching zero at the stellar surface. This behavior is probably unrealistic. The model assumes the inner annulus ($1R_{\star} < R \lesssim 1.5R_{\star}$) radiates the energy required by Equation (1) at T_{max} (KHH).

Broad-Band Energy Distributions

The production of synthetic disk spectra begins with the calculation of "weight tables" for models having different T_{max}. The disk is assumed to be spatially thin and flat (non-flaring). It is divided into concentric annuli, each having inner and outer radii such that standard supergiant effective temperatures may be used to approximate the local effective temperature of each annulus, and further constrained by the radial temperature distribution of a classical accretion disk given above. Supergiant distributions are used because the FU Ori objects appear best matched by absorption spectra of low surface gravity stars, such as

supergiants (Herbig 1966, 1977). Each annulus is assumed to radiate as a supergiant of the specified temperature. For a set of standard wavelengths, the relative contribution of each annulus is calculated, taking geometric factors, primarily the surface area of each annulus, into account. The required optical and ultraviolet spectrophotometry was provided by the stellar spectrum libraries of Wu *et al.* (1983) and Jacoby, Hunter, and Christian (1984). For the coolest annuli, having $T_d < 3500\,\mathrm{K}$ and $R \gtrsim 6R_\star$, blackbody energy distributions were used. Blackbody distributions provide poor representations of optical stellar fluxes, but such cool annuli contribute $\lesssim 10\%$ of the optical flux (KHH). The appropriately weighted supergiant and blackbody distributions are added to produce the predicted distribution for an accretion disk. The weight tables we have used for calculation of the high resolution synthetic disk spectra (see below) are given in Tables 4 and 5, which are portions of Tables 3 and 4, respectively, in KHH.

The accretion disk hypothesis demands an infrared energy distribution with $\lambda F_\lambda \propto \lambda^{-4/3}$, which constitutes infrared emission in excess of that from a star of appropriate optical spectral type alone. In the 4000 Å to 10 μm region, model energy distributions provide a good fit to the observed fluxes for FU Ori and V1057 Cyg (see KHH Figure 2). At longer wavelengths, additional excess emission is present in both objects. In Z CMa, there is emission far in excess of disk model prediction at all infrared wavelengths (see Hartmann *et al.* 1989, Figure 9). In all three objects, the outer portions of flared disks may be reprocessing photons from the inner disk, producing the observed infrared excesses (Hartmann *et al.* 1989).

High Resolution Spectral Synthesis

Calculation of high resolution model disk spectra makes use of the same procedure, with the additional assumption that each annulus radiates the line spectrum of stellar photoshere of the appropriate spectral type. High dispersion spectra of supergiants standard stars are used to represent each annulus. These spectra are obtained with the same equipment and set-up as the object spectra, so instrumental effects are the same in object and model spectra.

Table 4. Weight table for the V1057 Cyg disk model. We list here parameters for each annulus in the model for V1057 Cyg. The first three columns give the spectral type, outer radius, and temperature used for each annulus. The maximum temperature is 6590 K. BB in column 1 indicates that blackbody distributions have been used for the coolest annuli. The remaining columns give the fraction of total flux contributed by each annulus at the specified wavelengths. The sum of the entries in a given column may not be exactly 1.0 due to round-off error. The only parameter left unspecified is the rotational velocity scale. We have adopted $v_{rot} = 48\,\mathrm{km\,s^{-1}}$ at $R = 1R_\star$ for V1057 Cyg.

Type	R_{outer}	Temp	3520 Å	4500 Å	5550 Å	6370 Å	7400 Å	9000 Å
F6	1.50	6590	0.40	0.31	0.21	0.16	0.13	0.12
F7	1.73	6370	0.12	0.15	0.14	0.12	0.11	0.08
F8	1.95	6150	0.19	0.14	0.12	0.10	0.09	0.07
G0	2.14	5800	0.07	0.09	0.09	0.09	0.08	0.06
G1	2.26	5650	0.04	0.04	0.04	0.04	0.04	0.03
G2	2.37	5500	0.02	0.03	0.04	0.04	0.04	0.03
G3	2.55	5370	0.04	0.04	0.05	0.05	0.04	0.04
G5	2.77	5100	0.03	0.04	0.05	0.05	0.04	0.04
K0	2.98	4900	0.01	0.02	0.03	0.04	0.03	0.03
K1	3.20	4700	0.01	0.02	0.03	0.03	0.03	0.03
K2	3.85	4500	0.03	0.06	0.07	0.08	0.08	0.08
K5	4.60	3750	0.01	0.03	0.05	0.07	0.08	0.10
M1	4.86	3600	0.01	0.01	0.01	0.02	0.02	0.03
M2	5.19	3500	0.01	0.01	0.02	0.02	0.03	0.04
BB	5.70	3300	0.01	0.01	0.02	0.02	0.03	0.04
BB	6.28	3100	0.00	0.00	0.01	0.02	0.03	0.04
BB	6.96	2900	0.00	0.00	0.01	0.02	0.03	0.03
BB	7.77	2700	0.00	0.00	0.01	0.01	0.02	0.03
BB	8.73	2500	0.00	0.00	0.00	0.01	0.02	0.02
BB	9.91	2300	0.00	0.00	0.00	0.00	0.01	0.02
BB	11.37	2100	0.00	0.00	0.00	0.00	0.01	0.01
BB	13.22	1900	0.00	0.00	0.00	0.00	0.00	0.01
BB	15.64	1700	0.00	0.00	0.00	0.00	0.00	0.01

Because the disk is assumed to be in rapid Keplerian rotation, these spectra must be broadened according to the projected Keplerian speed in each annulus. The broadening function used is that which is appropriate to a rotating ring:

$$\phi(\Delta\lambda) = [1 - (\Delta\lambda/\Delta\lambda_m)^2]^{-1/2}, \tag{3}$$

where $\Delta\lambda = \lambda - \lambda_0$ is the displacement from line center, and $\Delta\lambda_m = \lambda_0[v_{rot}(R)\sin i]/c$ is the projected displacement due to the rotational velocity v_{rot} at radius R (KHH). This

Table 5. Weight table for FU Ori and Z CMa disk models. The primary difference between this model and that used for V1057 Cyg is the maximum disk temperature, which is 7200 K here. The boundaries between annuli occur at slightly different radii. We have adopted $R = 1 R_\star$ rotational velocities $v_{rot} = 85\,\mathrm{km\,s^{-1}}$ for FU Ori, and $v_{rot} = 115\,\mathrm{km\,s^{-1}}$ for Z CMa.

Type	R_{outer}	Temp	3520 Å	4500 Å	5550 Å	6370 Å	7400 Å	9000 Å
F2	1.46	7200	0.23	0.23	0.17	0.14	0.12	0.09
F3	1.61	7065	0.15	0.11	0.08	0.07	0.05	0.05
F4	1.71	6930	0.09	0.07	0.05	0.04	0.03	0.03
F5	1.83	6800	0.08	0.07	0.06	0.05	0.04	0.03
F6	1.98	6590	0.11	0.09	0.07	0.06	0.05	0.04
F7	2.14	6370	0.05	0.07	0.07	0.07	0.06	0.04
F8	2.35	6150	0.11	0.09	0.08	0.08	0.07	0.06
G0	2.54	5800	0.04	0.06	0.07	0.07	0.07	0.05
G1	2.67	5650	0.03	0.03	0.03	0.04	0.03	0.03
G2	2.80	5500	0.01	0.02	0.03	0.03	0.03	0.02
G3	2.99	5370	0.02	0.03	0.04	0.04	0.04	0.03
G5	3.23	5100	0.02	0.03	0.04	0.04	0.04	0.04
K0	3.46	4900	0.01	0.02	0.03	0.03	0.03	0.03
K1	3.71	4700	0.01	0.02	0.02	0.03	0.03	0.03
K2	4.43	4500	0.02	0.04	0.06	0.07	0.07	0.07
K5	5.28	3750	0.01	0.02	0.04	0.05	0.07	0.09
M1	5.56	3600	0.00	0.00	0.01	0.01	0.02	0.03
M2	5.94	3500	0.00	0.00	0.01	0.02	0.03	0.04
BB	6.51	3300	0.00	0.00	0.01	0.02	0.03	0.04
BB	7.16	3100	0.00	0.00	0.01	0.02	0.03	0.03
BB	7.93	2900	0.00	0.00	0.01	0.01	0.02	0.03
BB	8.84	2700	0.00	0.00	0.00	0.01	0.02	0.03
BB	9.93	2500	0.00	0.00	0.00	0.01	0.01	0.02
BB	11.26	2300	0.00	0.00	0.00	0.00	0.01	0.02
BB	12.90	2100	0.00	0.00	0.00	0.00	0.01	0.01
BB	14.99	1900	0.00	0.00	0.00	0.00	0.00	0.01

function is strongly double peaked, and is responsible for doubled absorption profiles in synthetic spectra.

To remove the differing standard star radial velocities, the standard star spectra are shifted to a common velocity scale before summing their contributions to the model flux. Using one of the intermediate spectral type standards as a template, we cross-correlated the remaining standards with the template to determine the relative shifts among the standards. The absolute scale was determined by measuring wavelengths of individual lines in the template spectrum. All standards were then shifted to $0\,\mathrm{km\,s^{-1}}$ with respect to laboratory wavelengths.

The spectral orders used in these calculations constitute a finer wavelength grid than exists in the weight tables. To account for the variation of weight with wavelength for a given annulus, we linearly interpolate the weight table to approximate the correct weight at each wavelength. The central wavelength of each order is used for the interpolation calculation.

To save observing time and computer disk space, we do not use a complete set of supergiant standards, one for each annulus. Instead, we use a grid of ~six standards covering the range of spectral types required (early to mid F to early M) and let each standard represent several annuli. Table 6 lists the standard stars we observed for each wavelength range, their spectral types, the range of annuli each represents in the models, linewidths, and their total contributions to our final models.

Ideally, we should have observed the same set of standards in the three wavelength ranges (grating settings), and those standards should have been carefully chosen to have the same (narrow) absorption linewidths. The differences in linewidths, due to rotation or macroturbulent broadening or both, among standards in each wavelength range is not very important for FU Ori and Z CMa, which have rotational widths ($\sim$60 km s^{-1} and $\sim$90 km s^{-1}, respectively) much larger than the linewidths in the standards (8 to 23 km s^{-1}). For V1057 Cyg ($v_{rot} \sim 35$ km s^{-1}), however, there may be reason for concern; linewidth differences in the standards may affect model profiles.

Differences in standard star absorption linewidths from one wavelength range to another (see Table 6) are probably the most serious problem introduced by our lack of an ideal set of standards. Average linewidths in the 3985–4920 Å, 4940–6830 Å, and 8030–9510 Å ranges, weighted by their contributions to the total flux of the T_{max} = 7200 K model, are 12.9 km s^{-1}, 10.1 km s^{-1}, and 14.2 km s^{-1}, respectively. The extreme values correspond to linewidth differences of 1.4 km s^{-1}, 0.8 km s^{-1}, and 0.6 km s^{-1} between the 4940–6830 Å and 8030–9510 Å synthetic spectra of V1057 Cyg, FU Ori, and Z CMa, respectively. Therefore it may not be appropriate to use the same rotational velocity scale in the model calculations in the different wavelength ranges.

Table 6. Stars used for high resolution spectral synthesis. Spectra of these stars were obtained during the 1988 November observing runs for the purpose of modeling the FU Ori object spectra. The spectral type of each star is given in column 2. In column 3 we list the "spectral types" of disk annuli that each star represents in the model calculations. Measured linewidths are given in column 4. Columns 5 and 6 list for the T_{max} = 6590 K and 7200 K models, respectively, the total contribution of each star to the continuum level of the synthetic spectra, for 4500 Å, 6370 Å, and 8200 Å, as appropriate.

Star Name	Spectral Type	Spectral Range	Linewidth	Contribution	
		4000–4920 Å Spectra			
α Lep	F0 Ib	F2–F3	12	0.00	0.34
α Per	F5 Ib	F4–F7	16	0.46	0.30
μ Per	G0 Ib	F8–G2	13	0.30	0.20
HR 1327	G5 IIb	G3–G5	9	0.08	0.06
ϵ Gem	G8 Ib	K0	12	0.02	0.02
β Gem	K0 IIIb	K1–2900 K	8	0.14	0.08
		4940–6820 Å Spectra			
SAO 11104	F0 I	F2–F3	9	0.00	0.21
SAO 22328	F6 Ib	F4–F8	9	0.38	0.30
SAO 22740	G2 Ib	G0–G5	10	0.27	0.22
SAO 22820	K0 Ib	K0–K1	13	0.07	0.06
SAO 22785	K5 Ib	K2–K5	9	0.15	0.12
SAO 23207	M3 Iab	M1–2100 K	14	0.12	0.10
		8030–9300 Å Spectra			
δ Cep	F5 Ib	F2–F7	11	0.22	0.32
β Aqr	G0 Ib	F8–G2	13	0.22	0.18
9 Peg	G5 Ib	G3–G5	12	0.08	0.08
56 Ori	K1.5 IIb	K0–K2	11	0.14	0.13
HR 8726	K5 Ib	K5	12	0.09	0.08
μ Cep	M2 Ia	M1–1300 K	23	0.24	0.22

The final concern about the standards is the spectral coverage. In the 4000-4920 Å range, coverage is from F0 to just K0. The lack of later standards is not serious because the K0 contributes only 6% of the continuum flux at 4000 Å, and just 12% at 4920 Å. Similarly, the lack of early F-type standard in the far red will require that our F5 standard represent the $\sim$10% of flux for which a hotter F0 standard would otherwise have been used. Of course, minor errors due to slightly improper spectral type matching between annuli and standards, as with using an incomplete grid of standards, will introduce minor errors in the models in any case.

It will also be noted that our earliest standard for the far red segment of the observations is δ Cep, the prototype Cepheid variable. This star varies from F5 to G2. In our spectrum it is very noticeably earlier than our G0 standard.

Details for the Program Objects

A variety of input data is required for calculation of synthetic disk spectra. In addition to the standard star spectra, which are assigned to annuli as specified in a weight table and Table 6, and broadened according to Equation (3) to the appropriate Keplerian speed, we must specify the maximum disk temperature, T_{max} (*i.e.*, which weight table to use), the projected rotational velocity normalization, $v_{rot}(R = R_\star)\sin i$, and the radial velocity of the object. The values we have adopted, based on goodness of fit tests (Chapter 6), are summarized in Table 7.

Table 7. Input parameters for disk spectrum synthesis. We summarize here the basic parameters needed for model calculation: maximum disk temperature, T_{max}; projected rotational velocity just above the stellar surface, v_{max}; and heliocentric radial velocity, v_{rad} of interstellar material near each object, with references.

	T_{max} (K)	v_{max} (km/s)	v_{rad} (km/s)	v_{rad} reference
V1057 Cyg	6590	48	−15.0	Herbig 1977
Z CMa	7200	115	+32.3	Edwards and Snell 1982
FU Ori	7200	85	+27.5	Edwards and Snell 1982

The weight tables used in this work (Tables 4 and 5) are portions of those from KHH (Tables 3 and 4, respectively). Similar tables, calculated for different T_{max}, were used for some of the tests to be discussed in later sections. Justification for use of the particular models chosen (T_{max} = 7200 K for FU Ori and Z CMa, T_{max} = 6590 K for V1057 Cyg), may be found in KHH and Hartmann *et al.* (1989). Briefly, the choices of T_{max} for FU Ori and V1057 Cyg were dictated by the requirement that synthetic energy distributions match

observed distributions from 4000 Å to $\sim$10 μm. In the case of Z CMa, similarity to FU Ori dictated the choice of T_{max} (Hartmann *et al.* 1989). We verify these values in Chapter 6.

To properly subtract a model spectrum from an object spectrum (Chapter 6), the model must be shifted to the object's radial velocity. There are three components to the required shift. We assume that the object is co-moving with surrounding interstellar material, so the heliocentric velocity of that material, determined from the literature (Herbig 1977 and references therein for V1057 Cyg and FU Ori, Edwards and Snell 1982 for Z CMa; see Table 7), is the first component. Second is the correction for the observatory motion with respect to the sun (heliocentric correction), determined with the reduction software. The final contribution, described in Chapter 3, corrects for movement of the CCD detector in its dewar as the telescope moves. The uncertainty in the second component is negligible for our purposes. We estimate that errors in the shifts between comparison spectra are $\lesssim 1\,\mathrm{km\,s^{-1}}$. The velocities quoted for interstellar material, and the assumption of common motion with that material is the largest uncertainty, but is probably $\lesssim 2\,\mathrm{km\,s^{-1}}$(see Herbig and Bell 1988 and Hartmann *et al.* 1989). In Chapter 6 we verify that these radial velocity shifts are appropriate.

The remaining parameter required for synthetic disk spectrum calculation is the normalization of the rotational velocity distribution. We have calculated cross-correlation functions for the synthetic disk spectra generated using the input parameters listed in Table 7. We find good agreement with cross-correlation peak widths of the object spectra (see Chapter 5) in regions of the spectrum that are relatively unaffected by non-disk components (*i. e.*, 6000–6800 Å; see Chapter 6).

Qualitative Predictions of the Model

Here we will describe the predictions of the accretion disk model qualitatively. These predictions will be examined quantitatively in Chapter 5. The differential rotation and radial temperature gradient of an accretion disk give rise to the key predictions of the model. These predictions are that:

• Spectral type should vary continuously with wavelength, because the hot ($\sim$6500 K) inner portion of such a disk dominates the optical continuum, while the cooler regions farther from the star, by virtue of their large emitting area, provide the largest contribution to the near-infrared continuum. Thus, the optical spectrum should be characterized by an earlier average spectral type than the near-infrared spectrum. This prediction has been well documented since the "early" years of the study of FU Ori objects (Grasdalen 1973, Herbig 1977).

• Absorption linewidths should decrease with increasing wavelength. Because the inner disk dominates the optical continuum, it will also be the region where the dominant contributions to optical absorption lines are formed. Similarly, infrared lines should be formed in the outer regions of the disk. Because the inner disk is rotating faster than the outer regions, optical lines should be broader than infrared lines.

• Absorption linewidths should increase with increasing lower excitation potential (LEP, χ_{low}), because higher excitation levels require the higher temperatures of the inner disk to be populated significantly. This temperature effect is potentially observable due to differential rotation in the disk.

• Absorption lines should have doubled profiles. Equation (3) provides the functional form for the line profile due to a single annulus. The profile for an actual line will be different because several annuli, rotating at different speeds, will contribute to the line.

• Absorption linewidths should increase as the disk fades and cools ($L \propto T^4$). In the disk hypothesis, fading is caused by a decrease in accretion rate through the disk. As this occurs, the radius from which the dominant contribution to the flux at given wavelength comes moves closer to the star. The absorption lines would be formed in material orbiting at higher speed, and would therefore be broader.

In Chapter 5 we present the results of our tests of the linewidth *vs.* wavelength and linewidth *vs.* excitation potential predictions of the accretion disk hypothesis. We will discuss doubling of line profiles briefly as part of our discussion of the goodness of fit of the synthetic spectra, in Chapter 6. Examination of residual features from subtraction of

synthetic disk spectra from our object spectra will be presented in Chapter 7. Observation of these model predictions would constitute important kinematic evidence that FU Ori objects are in fact luminous accretion disks, which dominate the luminosity at optical and near-infrared wavelengths.

CHAPTER 5

TESTS OF ACCRETION DISK MODEL PREDICTIONS

Measurement Techniques

In this Chapter we will examine the evidence for the accretion disk hypothesis predictions of variation of linewidth with wavelength and with lower excitation potential. These predictions will be made quantitative by identifying and measuring the absorption lines in synthetic and object spectra. Unless otherwise noted, the spectra being discussed are those obtained in 1988 November (see Table 3).

We measured widths of individual lines rather than using the cross-correlation technique used in HK1, HK2, HK3 for two primary reasons. First, the two effects may be separated from each other, to some extent. Because linewidth should vary with both wavelength and excitation potential, we will restrict the range of excitation potential when investigating variation of linewidth with wavelength, and examine the linewidth *vs.* excitation potential relationship in restricted wavelength ranges. Second, this method is more straightforward and conceptually simple than the cross-correlation method.

The first step was to identify all the relatively strong ($W_\lambda \gtrsim 50\,$mÅ) absorption lines in our FU Ori object spectra; lines weaker than $\sim$50 mÅ generally cannot be measured with $\lesssim 10\%$ uncertainty, owing to line broadening and finite signal to noise ratio of our data. Line identification was accomplished by comparing object spectra with spectra of standard stars, solar spectrum line lists (Swenson, *et al.* 1970; Moore, Minneart, and Houtgast 1966), and the Revised Multiplet Table (Moore 1959). The region around each strong absorption feature was compared with the corresponding line in a standard star of comparable spectral type to remove blended lines from the list. Lines were considered to be significantly blended, and removed from further consideration if another feature $\gtrsim 10\%$ as strong lay within the typical absorption profile full-width at half maximum for each object.

High spectral resolution observations reveal that line profiles in FU Ori, V1057 Cyg, and Z CMa are doubled, presumably due to line formation in a rotating circumstellar disk (HK2, HK3, KHH, Hartmann *et al.* 1989). The doubling is so pronounced in Z CMa that fitting a gaussian or other simple function is impossible. We should not attempt fitting more complicated functions, since we do not have *a priori* knowledge of the exact functional form of the broadening. Therefore, having set the local continuum, visual examination of line profiles to determine half-intensity points was the method employed for estimating linewidths.

Linewidth Versus Wavelength Results

Here we compare model prediction with observed results for our program objects. Having generated synthetic disk spectra as described in Chapter 4, model predictions can be made quantitative by measuring lines in the synthetic spectra as described above. We present the linewidth *vs.* wavelength results graphically, as $v \sin i$ *vs.* λ. A tabular summary of the results appears in Table 8. The synthetic spectra used were calculated with the best values of T_{max} and $v_{max} (= v_{rot}(R = R_\star) \sin i)$, as determined by our goodness of fit criterion to be discussed in Chapter 6.

V1057 Cygni

The published evidence for variation of linewidth with wavelength in FU Ori objects, consistent with model prediction, is strongest for V1057 Cyg. Using cross-correlation techniques, Hartmann and Kenyon (HK3) showed that absorption lines in the 6160 Å region are broader than at 2.3 μm, and, unlike their results for FU Ori (HK2, KHH), the synthetic spectrum cross-correlation peak widths agreed well at both wavelengths with those of V1057 Cyg itself. Supporting evidence was provided by Welty *et al.* (1990), who found evidence for *continuous* variation of linewidth with wavelength. In those studies, the synthetic disk spectra were calculated with $T_{max} = 6590$ K and $v_{max} = 43.6\,\mathrm{km\,s^{-1}}$.

Table 8. Linewidth *vs.* wavelength results. We present here the slopes and intercepts of least squares fits to the measured linewidth, wavelength pairs for our program objects (1988 November observations) and corresponding models. Also shown are data for the continuum+emission T Tauri star DG Tau, and α Per, an F5 Ib standard star. For the latter two objects, the far red data which enters here was obtained in 1989 December. If there is a Figure that corresponds to an entry, its number appears in column 1. FU Ori is conspicuous in its lack of significant slope and disagreement with model prediction.

Figure	Data Set	Slope ($\mathrm{km\,s^{-1}}$/1000 Å)	σ_{slope}	Intercept ($\mathrm{km\,s^{-1}}$)	σ_{int}	n[a]	r[b]
2a	V1057 Cyg Model	−1.68	0.23	49.8	1.5	63	−0.685
2b	V1057 Cyg	−1.57	0.19	48.3	1.2	63	−0.725
3a	Z CMa Model	−4.17	0.48	114.2	3.2	25	−0.875
3b	Z CMa	−4.30	0.44	116.0	2.9	25	−0.898
4a	FU Ori Model	−2.36	0.43	77.4	2.9	40	−0.665
4b	FU Ori	−0.30	0.30	62.0	2.0	40	−0.156
11a	DG Tau	−0.18	0.29	21.0	2.1	45	−0.091
11b	α Per	−0.09	0.11	17.0	0.7	81	−0.098

[a] n is the number of lines in the data set.
[b] r is the linear correlation coefficient for the data.

In Figure 2a we present the prediction for linewidth variation as a function of wavelength from the synthetic V1057 Cyg spectrum, spanning the 4000–9000 Å region. The synthetic spectrum was calculated using T_{max} = 6590 K and v_{max} = 48 $\mathrm{km\,s^{-1}}$. As in Welty *et al.* (1990), only those lines having 2 eV < χ_{low} < 5 eV have been included so that any effect of a linewidth *vs.* excitation potential correlation (see below) on the linewidth *vs.* wavelength relationship will be reduced.

The slope of the least-squares fit to the points is $-1.68 \pm 0.23\,\mathrm{km\,s^{-1}}$/1000 Å and the intercept is $49.8 \pm 1.5\,\mathrm{km\,s^{-1}}$, yielding a predicted decrease in linewidth of 19.8% from 4000 Å to 9000 Å, in fair agreement with 23.4% estimated directly from the weight table (Table 4) by identifying the half power radii (*i.e.*, for a given wavelength, the radius inside which half the radiation arises). It should be noted that the intercept in Figure 2a is significantly larger than the value $45.0 \pm 1.9\,\mathrm{km\,s^{-1}}$ found by Welty *et al.* (1990), who used the 1986 October and 1986 December spectra. We have used a larger $R = 1R_\star$ rotational velocity normalization in the model calculation than was used in their work (48.0 $\mathrm{km\,s^{-1}}$ compared to 43.6 $\mathrm{km\,s^{-1}}$) due

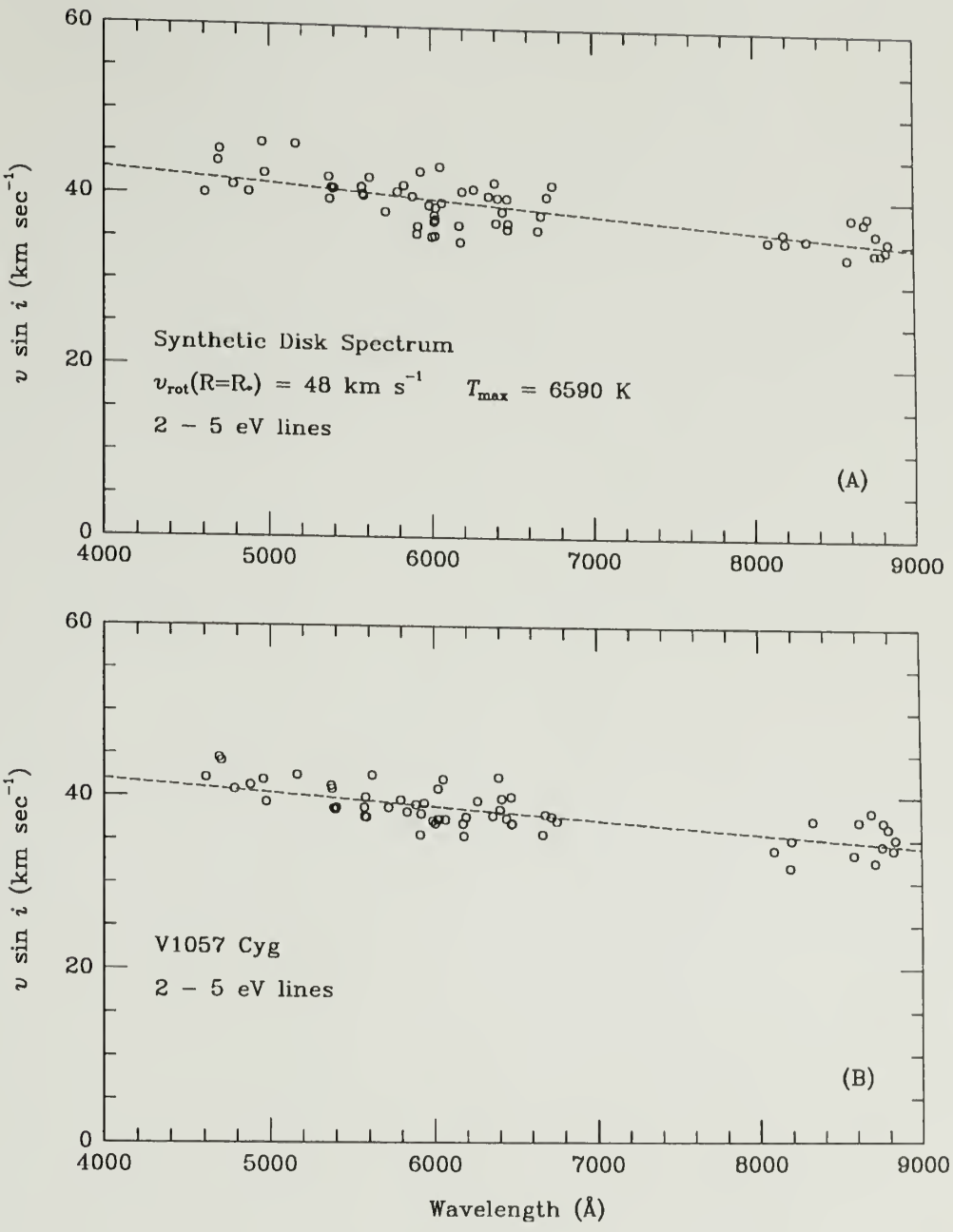

Figure 2. Predicted and observed linewidth *vs.* wavelength relationships for V1057 Cyg. The prediction of linewidth variation as a function of wavelength for the synthetic V1057 Cyg spectrum is illustrated in the top panel. The lower panel shows the observed linewidth *vs.* wavelength relationship. We believe the agreement between prediction and observation (see Table 8) is strong evidence for differential rotation in V1057 Cyg. The dashed lines are linear least-squares fits to the data. Only those lines having lower excitation potential between 2 and 5 eV have been included (see text). For the V1057 Cyg synthetic disk spectrum, $T_{max} = 6590$ K, and $v_{max} = 48$ km s^{-1}.

to the increase in absorption linewidths apparent from our 1986 October, 1986 December, 1988 November, and 1989 December spectra.

Figure 2b is the corresponding graph for V1057 Cyg itself. Points for the same lines as for the synthetic spectrum have been plotted. The slope of $-1.57 \pm 0.19\,\mathrm{km\,s^{-1}}/1000$ Å and intercept of $48.3 \pm 1.2\,\mathrm{km\,s^{-1}}$ agree with model prediction well within the uncertainties. We take this to be strong evidence for differential rotation arising in a circumstellar disk, in the spectrum of V1057 Cyg.

Z Canis Majoris

The Z CMa model prediction for the 4000–9000 Å region linewidth *vs.* wavelength correlation is presented in Figure 3a. The synthetic spectrum was calculated using T_{max} = 7200 K and $v_{max} = 115\,\mathrm{km\,s^{-1}}$. Due to the large rotational velocity, there are few relatively unblended lines in the spectrum of Z CMa. Therefore, we have included all measured lines, regardless of lower excitation potential. Omission of lines with extreme values of LEP yields only marginally different quantitative results.

The slope in Figure 3a is $-4.17 \pm 0.48\,\mathrm{km\,s^{-1}}/1000$ Å, and the intercept is $114.2 \pm 3.2\,\mathrm{km\,s^{-1}}$. This represents a 21.4% predicted decrease in linewidth over the 4000–9000 Å range, which compares favorably with the linewidth decrease of 23.7% estimated from the half power radii in the model weight table (Table 5). The results for linewidth *vs.* wavelength for Z CMa itself appear in Figure 3b. The slope, $-4.30 \pm 0.44\,\mathrm{km\,s^{-1}}/1000$ Å, and intercept, $116.0 \pm 2.9\,\mathrm{km\,s^{-1}}$, are in excellent agreement with model prediction.

In making a case for Z CMa's membership in the FU Ori class, Hartmann *et al.* (1989) did *not* claim evidence for differential rotation based on their cross-correlation analysis. They showed that the 2.3 μm CO absorption linewidths in Z CMa are much narrower than predicted by the accretion disk model, (0.2 times the 6200 Å region linewidths, compared to the model predicted ratio of ~0.5), and are blue-shifted by $25\,\mathrm{km\,s^{-1}}$ from the local interstellar velocity. Those CO observations, and the large infrared excess (see Hartmann *et al.* 1989, Figure 9)

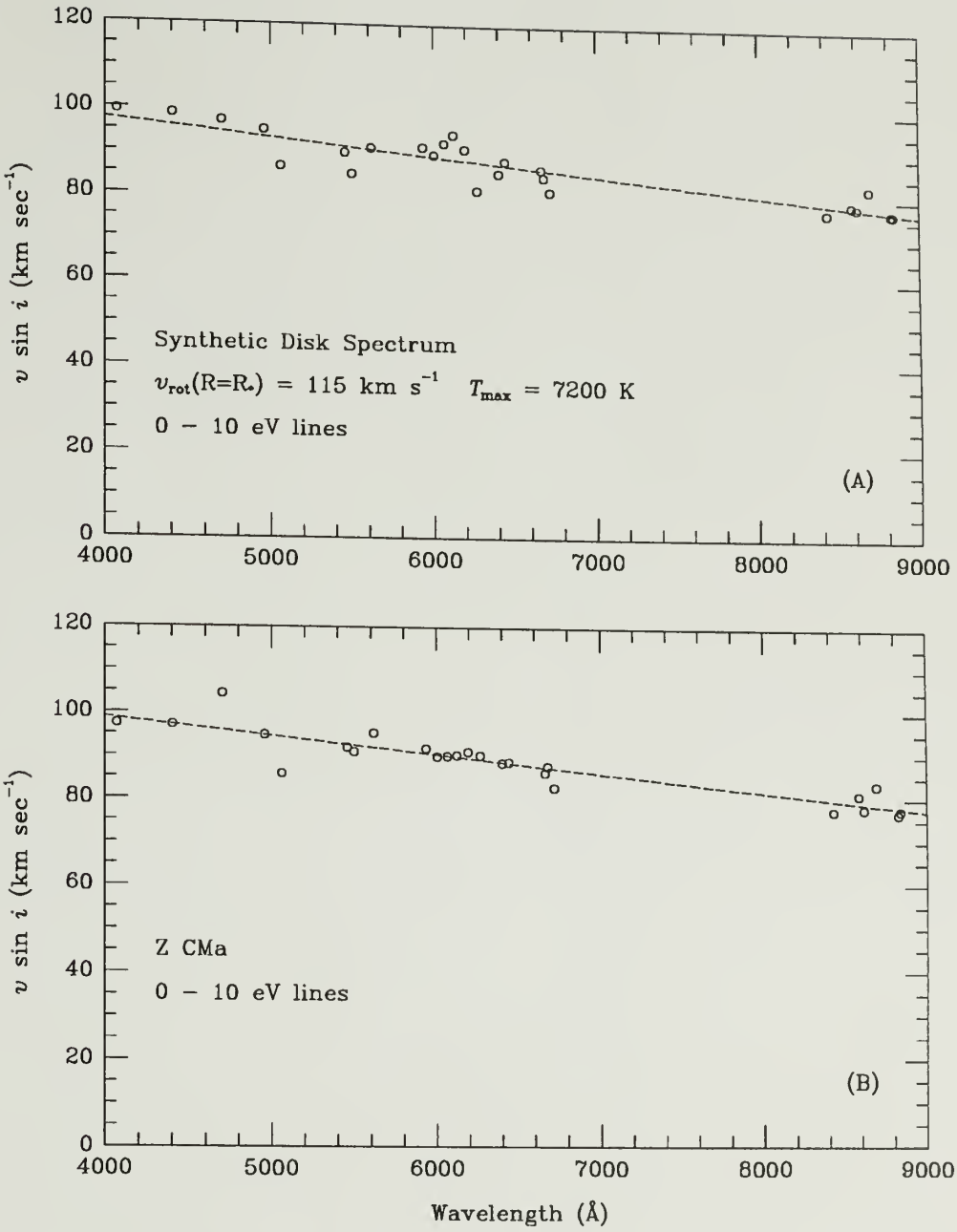

Figure 3. Predicted and observed linewidth *vs.* wavelength relationships for Z CMa. There is no restriction on LEP values, due to the small number of unblended lines present in this broad-lined object ($v_{rot} \sim 90\,\mathrm{km\,s^{-1}}$). As in V1057 Cyg, we take the excellent agreement between theory and observation here to be strong evidence for differential rotation in Z CMa. For the Z CMa synthetic disk spectrum, $T_{max} = 7200\,\mathrm{K}$, and $v_{max} = 115\,\mathrm{km\,s^{-1}}$.

make it clear that a differentially rotating, flat, thin classical accretion disk is not a complete description of Z CMa. Nevertheless, we regard the impressive agreement between our model

prediction and observation as strong evidence for differential rotation in Z CMa. In Chapter 7 we discuss an additional contribution to the Z CMa spectrum from a dense, cool wind.

FU Orionis

Model prediction of the linewidth *vs.* wavelength correlation for FU Ori, shown in Figure 4a, is much the same as for V1057 Cyg and Z CMa, with the exception of the rotational velocity scale. The synthetic spectrum was calculated using T_{max} = 7200 K and v_{max} = 85 km s^{-1}. The slope in Figure 4a is -2.36 ± 0.43 km s^{-1}/1000 Å, and the intercept is 77.4 ± 2.9 km s^{-1}.

Results for FU Ori itself, shown in Figure 4b, are strikingly different from the model and from V1057 Cyg and Z CMa. There is essentially no slope present. The formal result is -0.30 ± 0.30 km s^{-1}/1000 Å for the slope, and 62.0 ± 2.0 km s^{-1} for the intercept. Were it not for some reasonable explanation, to be discussed in Chapter 6, this would be a tremendous embarrassment, especially for the prototype of the class!

Cross-Correlation Results

In the studies that provided the first good evidence that FU Ori objects are luminous accretion disks, Hartmann and Kenyon (HK2, HK3) used cross-correlation techniques (Tonry and Davis 1979) to demonstrate the linewidth *vs.* wavelength relationship in FU Ori and V1057 Cyg. Although that method makes the search for a linewidth *vs.* lower excitation potential correlation impossible, because it uses all lines simultaneously, it has advantages over the method used in the preceding analysis. In particular, the cross-correlation method is not sensitive to line strength, but to the relative strengths of corresponding features in object and template spectra, and can be used in regions where there are blended features. It yields essentially the average line profile for the range of wavelength being analyzed.

Hartmann and Kenyon (HK2, HK3) relied on cross-correlations at only two wavelengths in their demonstration of the linewidth *vs.* wavelength relationship: the 6170 Å and 2.3 μm

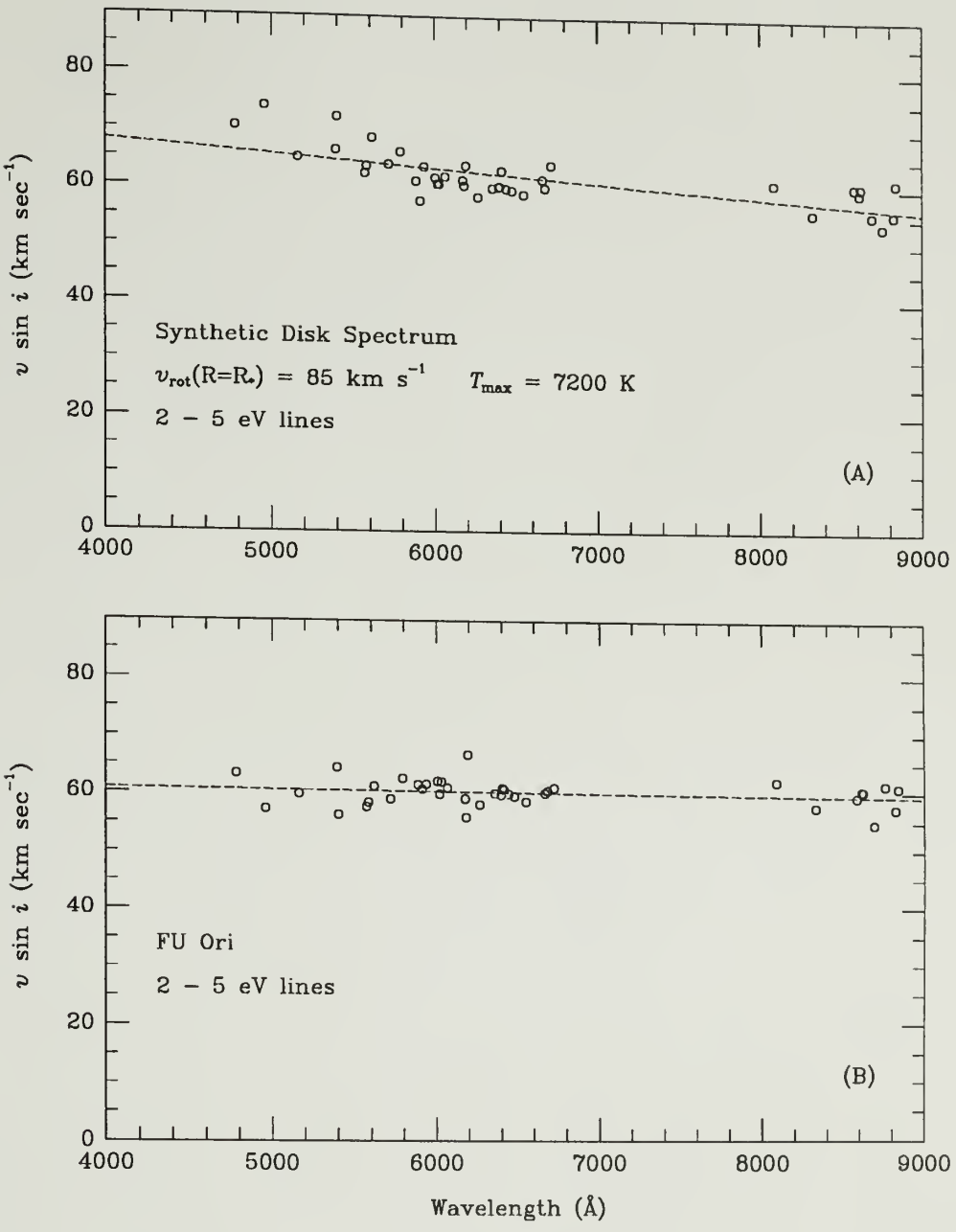

Figure 4. Predicted and observed linewidth *vs.* wavelength relationships for FU Ori. Note that there is essentialy no correlation in FU Ori itself, in contrast to the model prediction (see Table 8). Possible explanation for this disagreement will be given in Chapter 6. For the FU Ori synthetic disk spectrum, T_{max} = 7200 K, and v_{max} = 85 km s^{-1}.

(CO absorption) regions. At 5200 Å, results were inconsistent with disk model prediction, and were discounted on the grounds that wind contributions to the spectra may be affecting results

in the blue region of the spectrum. Here we present for each program object an example cross-correlation peak from each wavelength segment of our 1988 November observations, and reach similar conclusions. The wavelength regions shown were selected because they do not contain obvious wind features perturbing the line spectrum.

V1057 Cygni

Figure 5 shows the central portion of the cross-correlation function for V1057 Cyg in the 4610 Å, 6485 Å, and 8825 Å regions (solid), and for our T_{max} = 6590 K, v_{max} = 48 km s^{-1} synthetic spectrum (dotted). The template spectral types are G0 Ib, G2 Ib, and G8 Ib for panels A, B, and C, respectively, consistent with the variation of spectral type with wavelength observed in FU Ori objects.

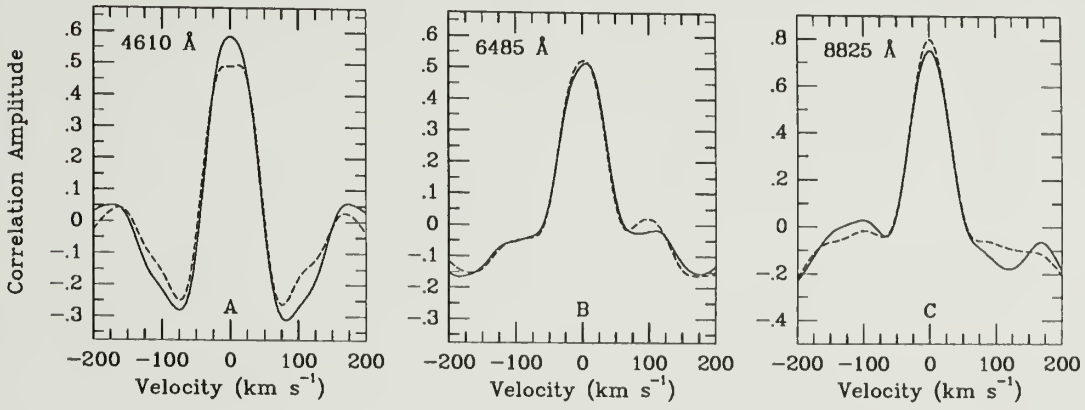

Figure 5. Cross-correlation functions for V1057 Cyg and synthetic spectra. In each case, about 400 pixels of an echelle order, selected to avoid obvious non-disk components (*e.g.*, shell features) has been cross-correlated with a standard star template. The spectral types of the templates are G0 Ib, G2 Ib, and G8 Ib for panels A, B, and C, respectively, consistent with the observation that spectral type varies with wavelength in FU Ori objects. Linewidths differ somewhat among the templates, so direct comparison of cross-correlation peak widths may not be useful, since V1057 Cyg rotates relatively slowly.

Because typical linewidths in V1057 Cyg are only ~35 km s^{-1}, and the template rotational velocities are ~10–15 km s^{-1}, the line doubling predicted by the disk model is not apparent. Wind features may be masking line doubling further. Only in the 4610 Å region

synthetic spectrum does a hint of doubling appear, by virtue of the slightly broader model lines at shorter wavelengths.

Z Canis Majoris

Analogous to Figure 5, Figure 6 shows the cross-correlation function for three Z CMa echelle orders and corresponding synthetic disk spectra (T_{max} = 7200 K, v_{max} = 115 km s^{-1}). The standard star templates are the same as for V1057 Cyg in Figure 5. In this case it is not clear how best to measure the widths of the cross-correlation peaks, in view of their different characters. We chose instead to measure the separation of the two peaks as a diagnostic of differential rotation. The separations are 123.4 km s^{-1}, 109.5 km s^{-1}, and 86.3 km s^{-1}, respectively. This result complements Figure 3 in providing clear evidence of differential rotation in Z CMa.

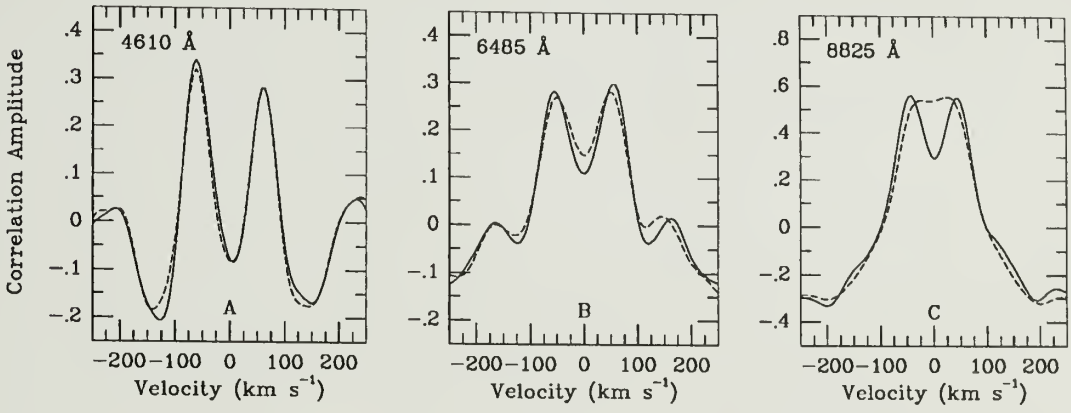

Figure 6. Cross-correlation functions for Z CMa and synthetic spectra. In each case, about 400 pixels of an echelle order, selected to avoid obvious non-disk components (*e.g.*, shell features) has been cross-correlated with a standard star template. The templates are the same as in Figure 5. The peculiarities of the cross-correlation peak profiles lead us to use the separation of the peaks to quantify differential rotation in this case. The separations in these figures are 123.4 km s^{-1}, 109.5 km s^{-1}, and 86.3 km s^{-1}, for A, B, and C, respectively. So, for regions not obviously disturbed by wind features, there is strong evidence for differential rotation in Z CMa. The decrease in doubling of the model at longer wavelengths is caused by the overall narrowing of the model, combined with use of broader lined standards at longer wavelengths (see Table 6).

FU Orionis

For FU Ori the situation is not as encouraging, from the standpoint of wanting observation to match model prediction. Figure 7 shows the cross-correlation function for FU Ori (solid) and our best model (dotted). FU Ori rotates sufficiently rapidly that line doubling is apparent in the model in all three panels, and in FU Ori itself in the latter two. At the short wavelengths represented by panel A, no doubling is present in FU Ori. We believe wind contributions to the spectrum are particularly strong in the spectrum of FU Ori, and cause this short wavelength mismatch.

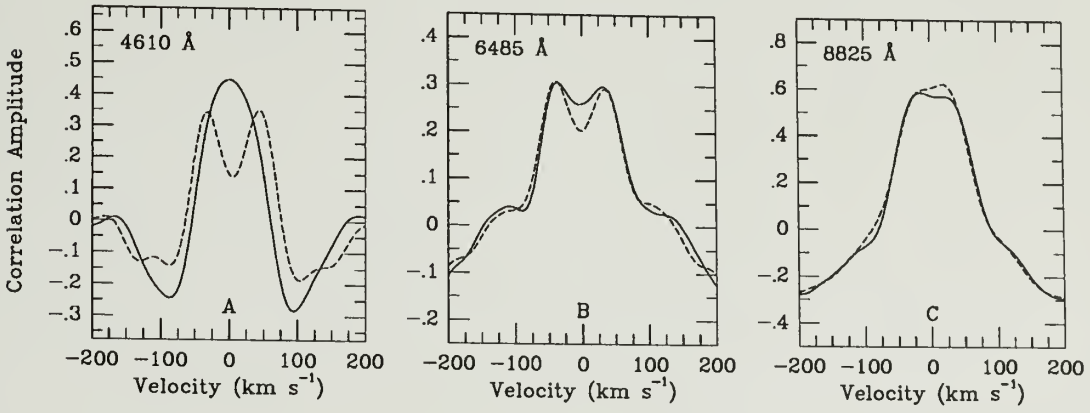

Figure 7. Cross-correlation functions for FU Ori and synthetic spectra. The model spectra were calculated with T_{max} = 7200 K and v_{max} = 85 km s^{-1}. Note the complete mismatch, and slight blueshift of FU Ori, in the 4610 Å panel. We believe wind contributions to spectral lines and gravity mismatch strongly perturb the line profiles at these short wavelengths (see Chapters 6 and 7).

Linewidth Versus Excitation Potential Results

As discussed in Chapter 4, the accretion disk model predicts that a correlation should be found between the widths of absorption lines and the lower excitation potential of the transitions involved. Herbig, in a recent review talk, described a search he had made for such a correlation in early Lick spectrograms of FU Ori and V1057 Cyg. He found no correlation. He found the same negative result with more recent, higher quality data (Herbig 1989). This

effect was also searched for by Welty *et al.* (1990), who detected marginal linewidth *vs.* LEP correlations in 12 km s^{-1} resolution echelle spectra of V1057 Cyg: 1.10 ± 0.44 km s^{-1} eV^{-1} (1986 December, 5820–7640 Å), and 1.16 ± 0.35 km s^{-1} eV^{-1} (1986 October, 7500–9300 Å). We have secured multi-epoch, high signal-to-noise spectra spanning most of the 4000–9000 Å region, and are able to investigate more completely the question of the existence and repeatability of this correlation.

We have shown that linewidth decreases significantly over the 4000–9000 Å region in the spectra of V1057 Cyg and Z CMa. To detect a variation of linewidth with excitation potential, we must restrict the range of wavelength to be considered. The simplest way to restrict wavelength is to consider the three observational data sets (3985–4920 Å, 4940–6830 Å, 8030–9000 Å) separately. Because a large number of plots would otherwise be involved (data and models for three objects in three wavelength ranges), we will present results graphically only for the 4940–6830 Å data. Complete results appear in Table 9.

V1057 Cygni

From our T_{max} = 6590 K, v_{max} = 48 km s^{-1} synthetic spectrum, the predicted linewidth *vs.* LEP relationship is shown in Figure 8a. The slope of the least squares fit is 0.99 ± 0.29 km s^{-1} eV^{-1}. We see that, even for the synthetic spectrum, the correlation is not particularly strong. Figure 8b shows the observed linewidth *vs.* LEP relationship. The slope is 0.77 ± 0.18 km s^{-1} eV^{-1}. By itself this 4.3σ result appears significant, but the marginal agreement with model prediction is troubling.

In the far-red region (8030–9510 Å) the situation is different. Measurement of the model spectrum yields a slope of 0.89 ± 0.18 km s^{-1} eV^{-1}, and the slope for the V1057 Cyg spectrum is 0.84 ± 0.24 km s^{-1} eV^{-1}. In the blue region (3985–4920 Å), there are too few lines (6) in our list for us to draw any firm conclusions. Complete results for all three wavelength ranges appear in Table 9.

Table 9. Linewidth *vs.* excitation potential results. We present here the slopes and intercepts of least squares fits to the measured linewidth, excitation potential pairs for our program objects and corresponding models in each wavelength range observed in the 1988 November observing runs. The T Tauri star DG Tau, and α Per, for which we expect no correlation, are included for comparison. In column 2, (λ_1), (λ_2), and (λ_3) refer to the 3985–4920 Å, 4940–6830 Å, and 8030–9510 Å spectral regions, respectively. There are no entries for Z CMa, FU Ori, and DG Tau in the blue spectral region because there are only two or three lines that are neither blended nor corrupted by bad pixels. The number of lines involved is given in column 7, and the linear correlation coefficient for the data appears in column 8. If there is a Figure that corresponds to an entry, its number appears in column 1.

Figure	Data Set	Slope ($km\,s^{-1}\,eV^{-1}$)	σ_{slope}	Intercept ($km\,s^{-1}$)	σ_{int}	n[a]	r[b]
	V1057 Cyg Model (λ_1)	1.32	1.00	37.9	3.1	6	0.553
	V1057 Cyg (λ_1)	1.23	0.67	38.7	2.1	6	0.679
8a	V1057 Cyg Model (λ_2)	0.99	0.29	36.1	0.9	63	0.404
8b	V1057 Cyg (λ_2)	0.77	0.18	36.1	0.6	63	0.471
	V1057 Cyg Model (λ_3)	0.89	0.18	32.8	0.7	22	0.735
	V1057 Cyg (λ_3)	0.84	0.26	33.1	1.0	22	0.577
9a	Z CMa Model (λ_2)	0.65	1.04	86.9	2.8	16	0.164
9b	Z CMa (λ_2)	0.62	0.78	88.2	2.1	16	0.208
	Z CMa Model (λ_3)	0.33	1.41	77.8	3.4	6	0.117
	Z CMa (λ_3)	0.63	1.60	77.6	3.9	6	0.193
10a	FU Ori Model (λ_2)	1.06	0.58	59.5	1.7	42	0.274
10b	FU Ori (λ_2)	0.64	0.32	58.2	0.9	42	0.302
	FU Ori Model (λ_3)	2.75	0.69	50.5	1.8	11	0.799
	FU Ori (λ_3)	2.13	0.57	53.5	1.5	11	0.778
	DG Tau (λ_2)	–0.32	0.59	21.8	1.8	19	–0.132
	DG Tau (λ_3)	–0.19	0.25	20.1	1.0	34	–0.137
	α Per (λ_1)	–0.11	0.28	18.2	0.8	7	–0.172
	α Per (λ_2)	–0.12	0.13	16.8	0.5	52	–0.123
	α Per (λ_3)	–0.05	0.14	16.1	0.6	42	–0.058

[a] n is the number of lines in the data set.
[b] r is the linear correlation coefficient for the data.

We wish to compare our result with that of Welty *et al.* (1990), who found similar results with 1986 October and 1986 December spectra of V1057 Cyg. For proper comparison, we must determine slopes for identical line lists. For the 36 lines in common in the 5820–6830 Å region, their result would be $0.85 \pm 0.24\,km\,s^{-1}\,eV^{-1}$, and ours would be $0.76 \pm 0.21\,km\,s^{-1}\,eV^{-1}$. For the 15 lines in common in the 8030–9300 Å region, their result would be $1.32 \pm 0.42\,km\,s^{-1}\,eV^{-1}$, and ours would be $1.27 \pm 0.37\,km\,s^{-1}\,eV^{-1}$. We take this

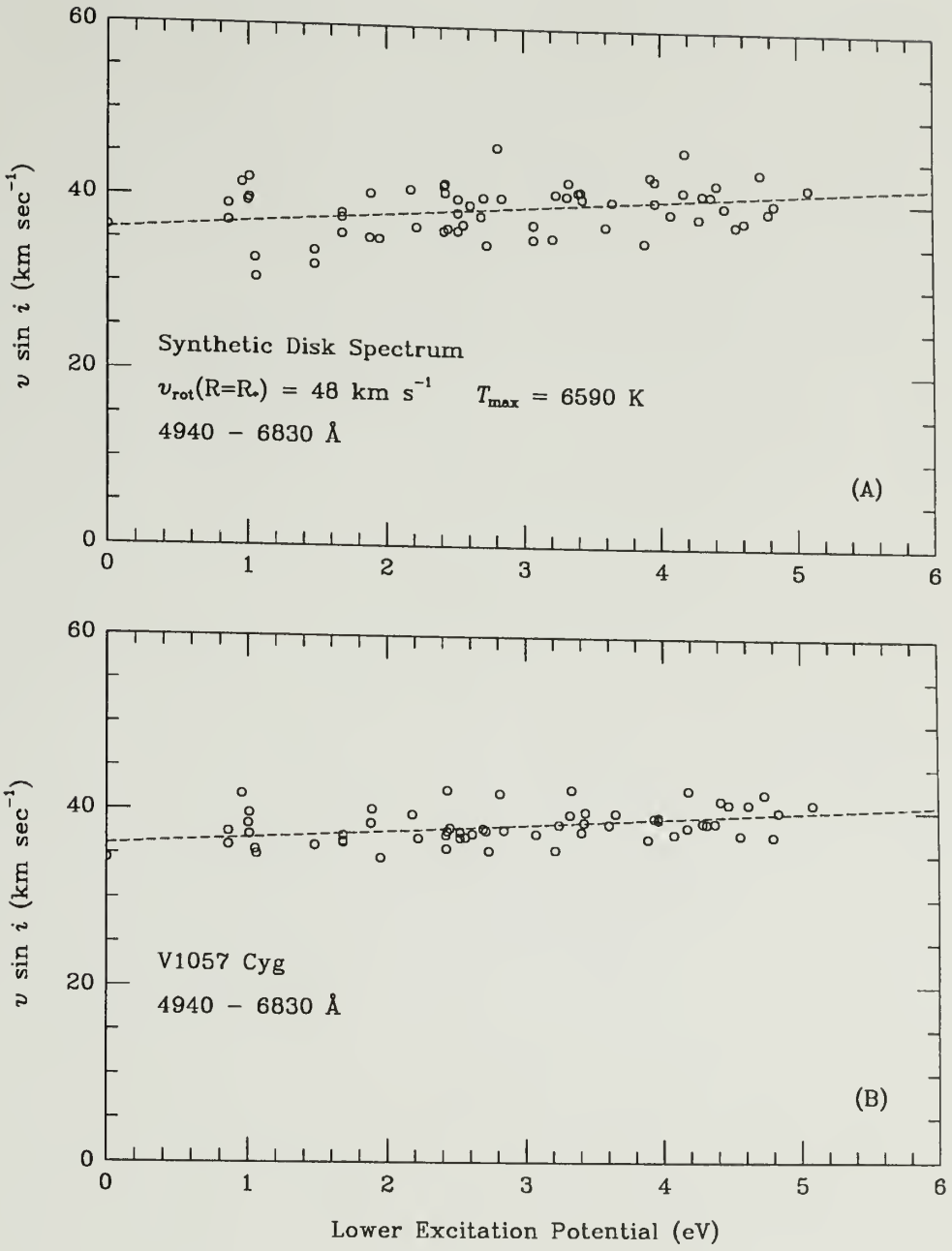

Figure 8. Predicted and observed linewidth *vs.* LEP relationships for V1057 Cyg. The agreement between prediction and observation is marginal, but it is clear that a correlation is present. This result is consistent with that of Welty *et al.* (1990) who analyzed spectra obtained two years earlier.

repeatability as further evidence that a linewidth *vs.* LEP correlation exists in the spectrum of V1057 Cyg.

Z Canis Majoris

The 4940–6830 Å linewidth *vs.* LEP model prediction from our T_{max} = 7200 K, v_{max} = 115 km s^{-1} synthetic spectrum is shown in Figure 9a. The slope is 0.65 ± 1.04 km s^{-1} eV^{-1}. For Z CMa itself (Figure 9b), the slope is 0.62 ± 0.78 km s^{-1} eV^{-1}. The uncertainties are large primarily because only 16 points are involved. The close agreement between predicted and observed slopes is probably fortuitous.

There are even fewer unblended lines in the blue and far-red regions. Results based on them are highly uncertain, and do not merit further discussion. We believe firmer results on the existence of a linewidth *vs.* LEP correlation in Z CMa will be extremely difficult to obtain, because the extensive line blending will remain a serious hindrance.

FU Orionis

In view of our linewidth *vs.* wavelength results for FU Ori, it would not be unexpected if a linewidth *vs.* LEP correlation does not exist in the spectrum of this object. The prediction for 4940–6830 Å (from the T_{max} = 7200 K, v_{max} = 85 km s^{-1} synthetic spectrum, and shown in Figure 10a) is a slope of 1.06 ± 0.58 km s^{-1} eV^{-1}, and the slope from the FU Ori spectrum is 0.64 ± 0.32 km s^{-1} eV^{-1} (Figure 10b). So it appears that a correlation is present, though agreement with the model prediction is not good.

As is the case for Z CMa, there are too few unblended lines in our blue and far-red spectra to attempt to draw firm conclusions from those data. It is interesting, though, that prediction and observation agree, based on 11 points, that a large slope is present in the far-red region. They are, respectively, 2.75 ± 0.69 km s^{-1} eV^{-1} and 2.13 ± 0.57 km s^{-1} eV^{-1}.

In summary, we find evidence for a linewidth *vs.* excitation potential correlation in the red and far-red spectrum of V1057 Cyg. Similar correlations may be present in Z CMa and FU Ori. Line blending will continue to hamper efforts to make any firm conclusions for the latter two objects. In any case, the apparent subtlety of the effect as judged from

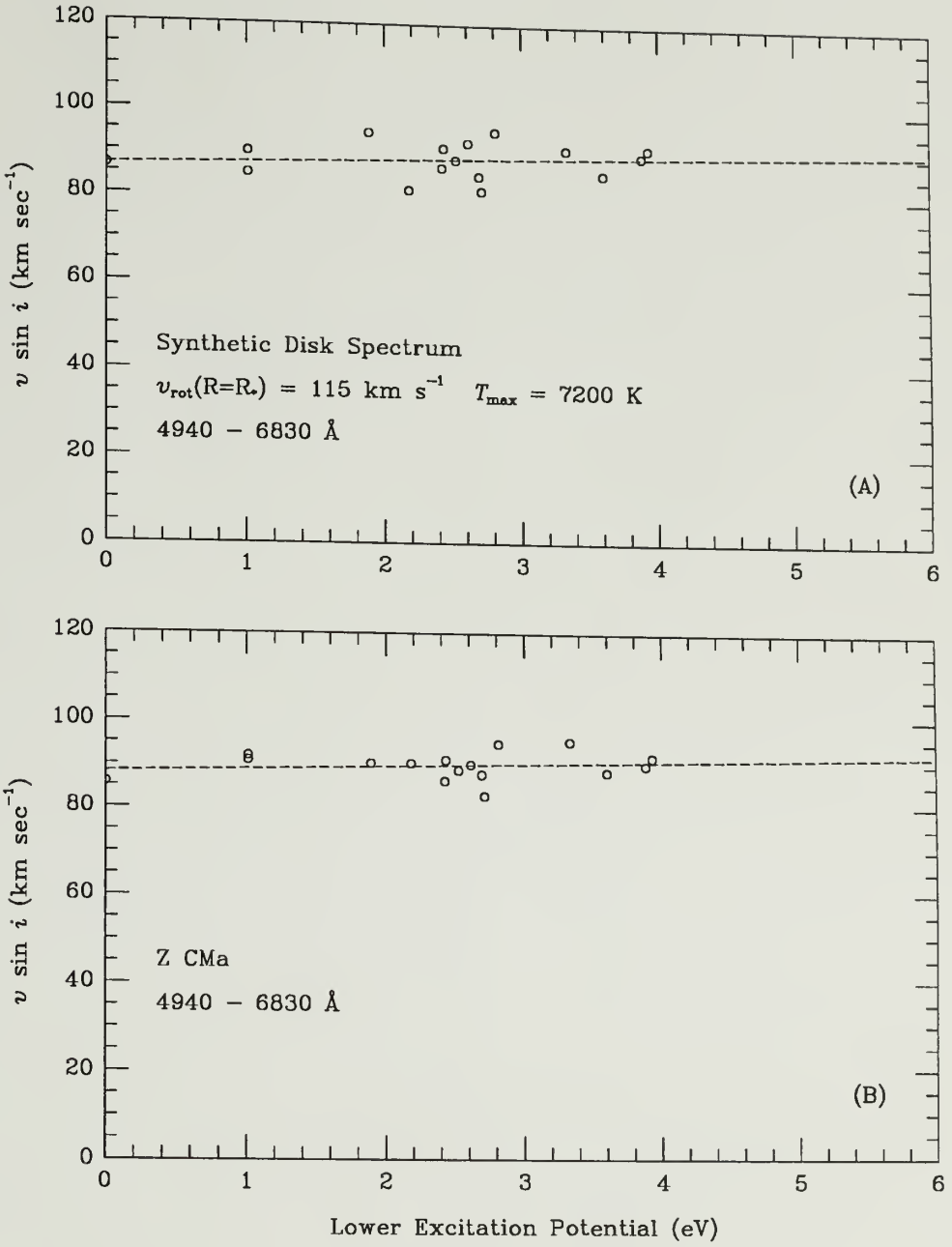

Figure 9. Predicted and observed linewidth *vs.* LEP relationships for Z CMa. Because only 16 unblended lines are available, the formal uncertainty is large for the slopes of the fitted lines. We can conclude only that results from observed and synthesized spectra are not inconsistent.

measurement of synthetic spectra, and the scatter that is present, render this effect less useful as a diagnostic of differential rotation than the linewidth *vs.* wavelength relationship.

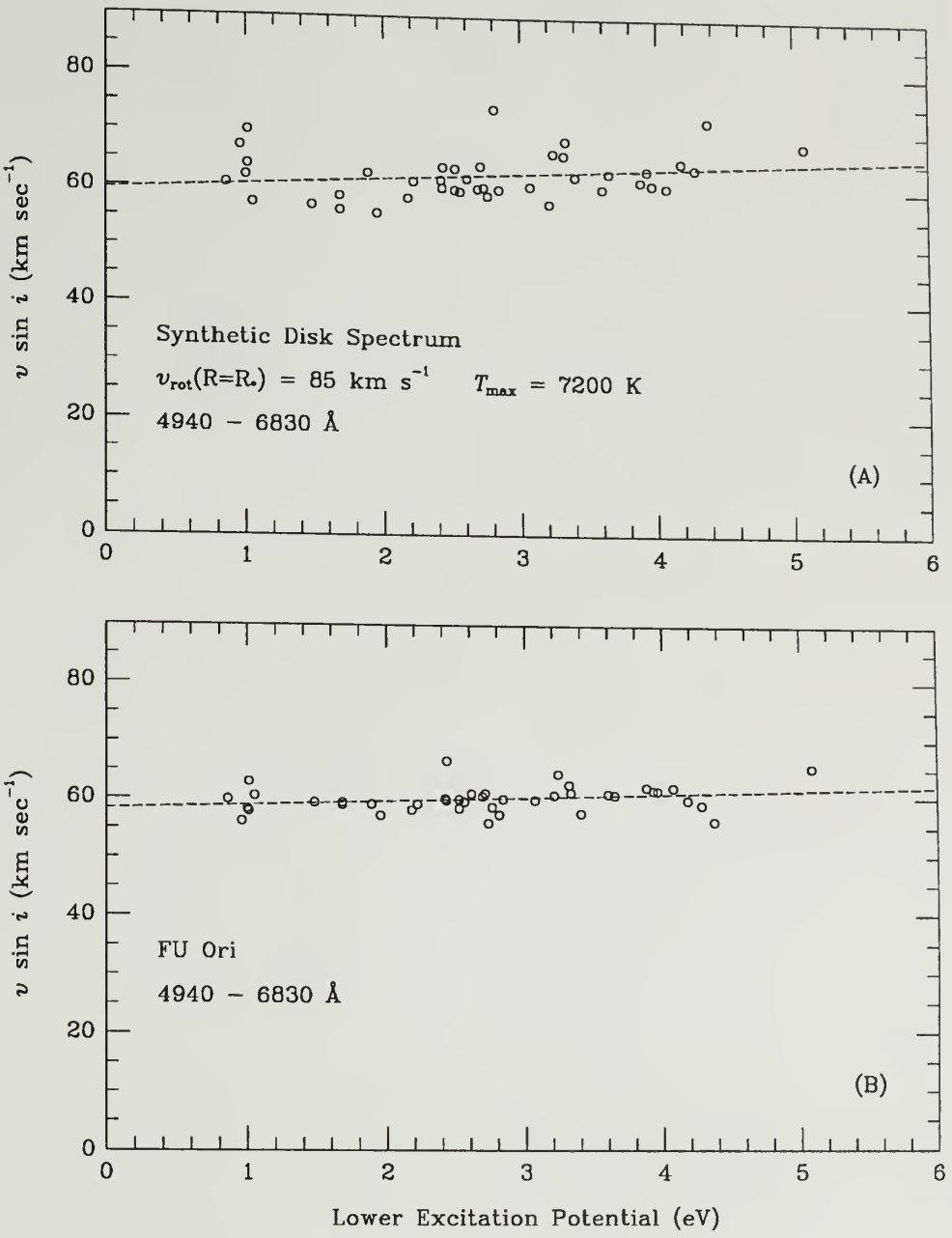

Figure 10. Predicted and observed linewidth *vs.* LEP relationships for FU Ori. As is the case for V1057 Cyg, a real correlation appears to be present in both observed and synthetic spectra, but the agreement is not impressive. For all three objects, it appears that the linewidth *vs.* LEP correlation is a subtle one, less useful as a diagnostic of differential rotation than the linewidth *vs.* wavelength correlation.

We have seen that a significant linewidth *vs.* wavelength correlation exists in both V1057 Cyg and Z CMa. That this relationship agrees so well with accretion disk model prediction provides strong kinematic evidence that those objects are in fact luminous accretion disks. For FU Ori the case is not good. A possible resolution to this dilemma is presented in Chapter 7. The search for a linewidth *vs.* lower excitation potential correlation has yielded some support for the accretion disk hypothesis. We wish to know whether these correlations are unique to the FU Ori objects, and if systematic errors may be ruled out as their origin.

The disk model assumes that accretion luminosity overwhelms all other contributions at wavelengths considered here, unlike other classes of pre–main-sequence (PMS) objects and normal stars. The likeliest candidates among optically visible PMS objects to possess the linewidth correlations observed in the FU Ori objects are those which presumably possess disks which are actively accreting, *i.e.*, the classical T Tauri stars (TTS). Many TTS have broad spectral energy distributions which are indicative of disks. In particular, the flat spectrum sources (DR Tau, DG Tau, *etc.*) are presumed to have substantial disks and disk accretion rates higher than in other TTS, but $\gtrsim 2$ orders of magnitude smaller than those demanded by the accretion disk model for the FU Ori objects. Many of these objects have prominent emission line spectra, but no absorption lines are apparent at moderate and low resolution ($\gtrsim 10\,\mathrm{km\,s^{-1}}$). They are therefore known as "continuum+emission" TTS. Herbig's (1958, 1977) description of its pre-outburst spectrum suggests that V1057 Cyg may have been an object such as this.

DG Tau is a moderately veiled continuum+emission TTS (Welty *et al.* 1989, Hartigan *et al.* 1991). While luminosity from its disk may be a significant fraction of the total at optical wavelengths, we expect the observed absorption spectrum to be formed in the stellar photosphere. We therefore expect no correlation of linewidth with wavelength or with lower excitation potential. Since the rotational velocity of DG Tau is relatively small ($v \sin i \sim$

20 km s^{-1}), there should be no peculiarities which might be introduced by a very rapidly rotating star (see Chapter 1). As far as possible, the same lines were measured in the spectrum of DG Tau as in V1057 Cyg. Because DG Tau was not observed in the far red in the 1988 November observing run, the far red lines were measured in a spectrum obtained in 1989 December. The observing set ups were the same for the two runs, and there is, to our knowledge, no time variation of linewidths in DG Tau, so this should not affect our results. A plot of linewidth *vs.* wavelength for DG Tau appears in Figure 11a. As expected, no correlation is observed; the slope of the fit is -0.18 ± 0.29 km s^{-1}/1000 Å. Similarly, there is no apparent linewidth *vs.* lower excitation potential relationship (see Table 9).

Similar results are obtained for α Per, one of our F5 Ib standard stars. The fit to linewidth, wavelength points, shown in Figure 11b, is -0.09 ± 0.11 km s^{-1}/1000 Å. Complete results for the linewidth *vs.* LEP test appear in Table 9; for the 4940–6830 Å region the fitted slope is -0.12 ± 0.13 km s^{-1} eV^{-1}. We have checked several other TTS and standard stars; none seem to posess any significant linewidth *vs.* wavelength or linewidth *vs.* excitation potential correlations.

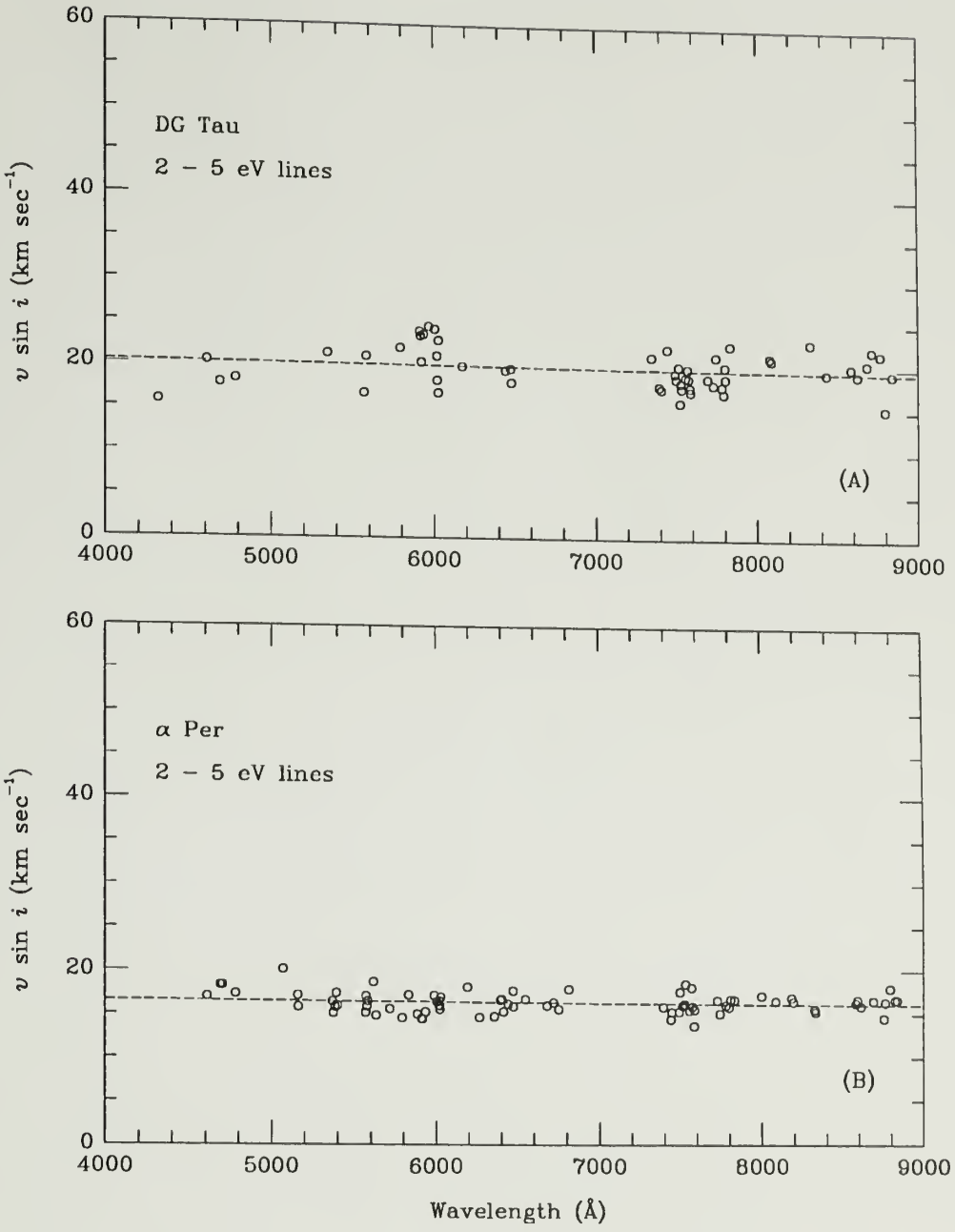

Figure 11. Linewidth *vs.* wavelength plot for DG Tau and α Per. Although a significant fraction of the flux from DG Tau probably arises from an accretion disk and boundary layer (see Hartigan *et al.* 1991), it does not dominate the spectrum as FU Ori disks do. So we expect no obvious signatures of differential rotation in DG Tau, or in α Per, a supergiant standard star.

CHAPTER 6

SYNTHETIC SPECTRUM SUBTRACTION: GOODNESS OF FIT

Subtraction of Synthetic Disk Spectra

We have taken our investigation of the applicability of the accretion disk model to the FU Ori objects further by subtracting synthetic (model) disk spectra from object spectra. From the resulting residual spectra we hope to determine several important properties of our program objects: best values and acceptable limits for basic disk parameters (T_{max}, v_{max}), radial velocities, and information about non-disk (*e.g.*, wind) components that may be present in the FU Ori systems. In the remainder of this section we simply present spectra in selected regions of the optical region for which the synthetic spectra accurately reproduce object spectra. In the following section we present an objective method for assessing the overall goodness of fit, and present our results for that test, including determination of the best model parameters.

V1057 Cygni

Figure 12 shows examples of how well our synthetic spectra fit the observed spectrum of V1057 Cyg in two 40 Å sections. The solid line is a section of the V1057 Cyg spectrum. Offset vertically by different constants, but at the same scale, are the corresponding synthetic disk spectrum, a broadened supergiant standard for comparison, and the residual spectrum (object minus model). The artificial broadening of the standard assumes the rotational broadening for a spherical star, and a standard limb-darkening law with limb-darkening coefficient of 0.6 (see Gray 1976).

In Figure 12 it is clear that the accretion disk model is a better description of V1057 Cyg at these wavelengths than a single, normal rotating star. While the model line doubling is not strong, due to use of relatively broad lined standards ($v \sin i \sim 10 - 15\,\mathrm{km\,s^{-1}}$) to

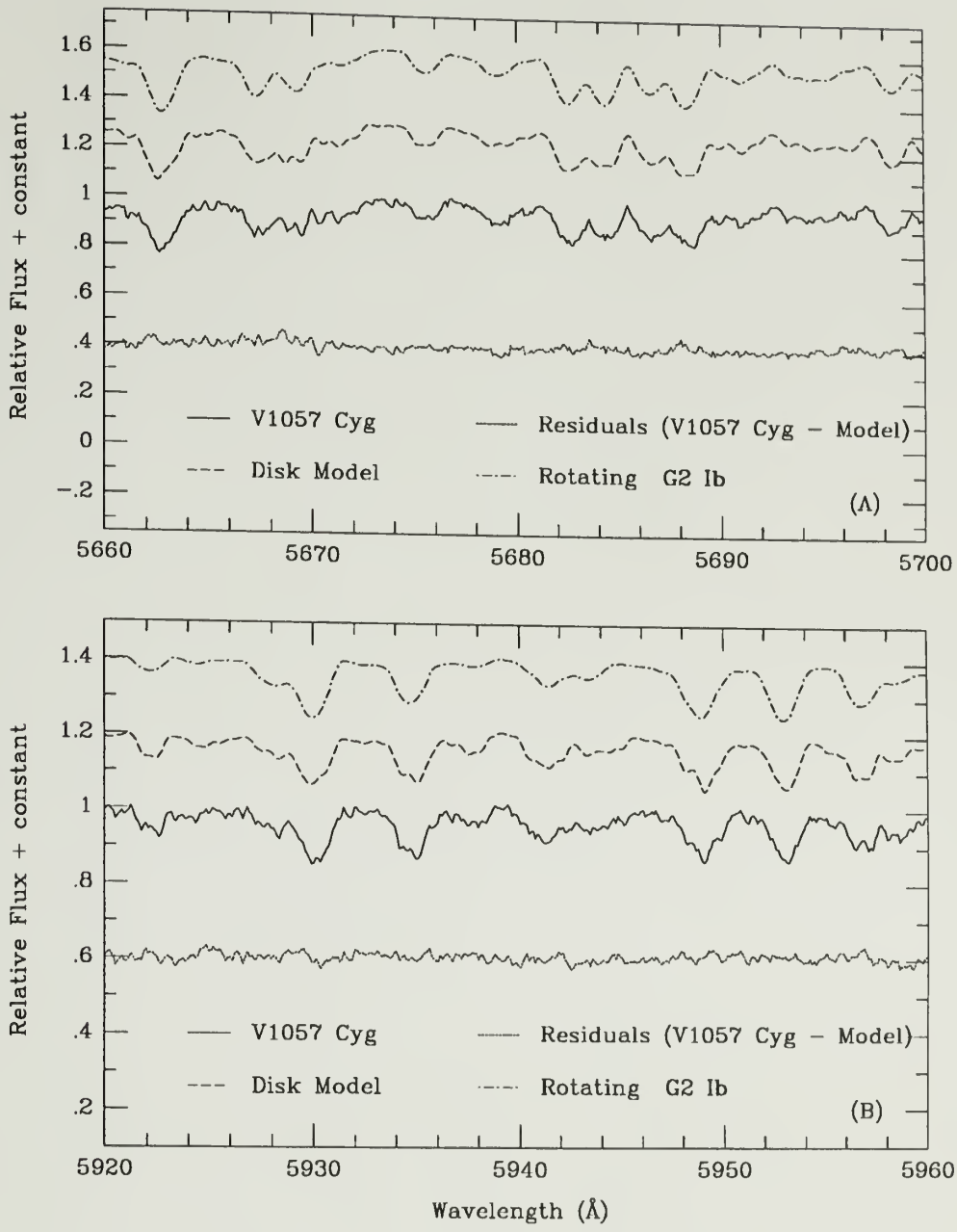

Figure 12. V1057 Cyg data, model, residuals, and rotating G2 Ib star. At these wavelengths the synthetic spectrum provides an excellent fit to the observations. Because the projected rotational velocity of V1057 Cyg is not exceptionally large ($v_{rot} \sim 35\,\mathrm{km\,s^{-1}}$), the doubling of absorption profiles is not strong, even in the synthesized spectrum. Even so, the model offers a better representation of the data than a single rotating star (standard star spectrum artificially broadened assuming a spherical star and a standard limb-darkening law [Gray 1976]). The features at λ5934 Å, λ5949 Å, λ5949 Å, and λ5956 Å in particular, have profiles better matched by the disk model. In neither section are there any large residual features. The high frequency wiggles are reflections of the noise in the observed spectrum.

model a relatively narrow lined FU Ori object (typical $v \sin i \sim 35\,\mathrm{km\,s^{-1}}$), synthetic disk line profiles are superior those of a rotating star. Profiles of features at λ5922 Å, λ5934 Å, λ5949 Å, and λ5956 Å are obviously better matched by the disk model profiles.

For these wavelength regions there are no poor fits. The high frequency wiggles reflect the noise in the V1057 Cyg spectrum. Small errors in continuum normalization, and small departures of the model from the intrinsic object spectrum may be present, but there are no large residual features. In the next section we propose an objective method for identifying residual features.

Z Canis Majoris

If we consider Z CMa, whose projected rotational velocity is ~2.4 times that of V1057 Cyg, a much clearer picture emerges. The large rotational broadening permits easy differentiation between disk model and rotating star as representations for the spectrum of Z CMa. Figure 13 shows clearly the inability of the single rotating star to reproduce the line spectrum, while the disk model does quite well. The region from 5682 Å to 5690 Å in particular illustrates the capacity of the model for matching the object spectrum in a region of complicated line blending. Only very weak features appear in the residual spectrum.

FU Orionis

The case for FU Ori is very different. The disagreement between data and model presented in Chapter 5 leads us to expect significant departures of the data from the model. In Figure 14a we show the spectra of FU Ori, the corresponding model disk, a rotating star, and the residuals. In this region, where the synthetic spectrum fits Z CMa so well (Figure 13a), several obvious residual features are present. In Figure 14b the fit to FU Ori is better, though not as good as the fit to V1057 Cyg and Z CMa in the same region (Figures 12a and 13b). Synthetic disk spectra fail badly to reproduce the observed spectrum of FU Ori from 4000 Å to 5500 Å, but at wavelengths longer than ~6000 Å, do as well as for V1057

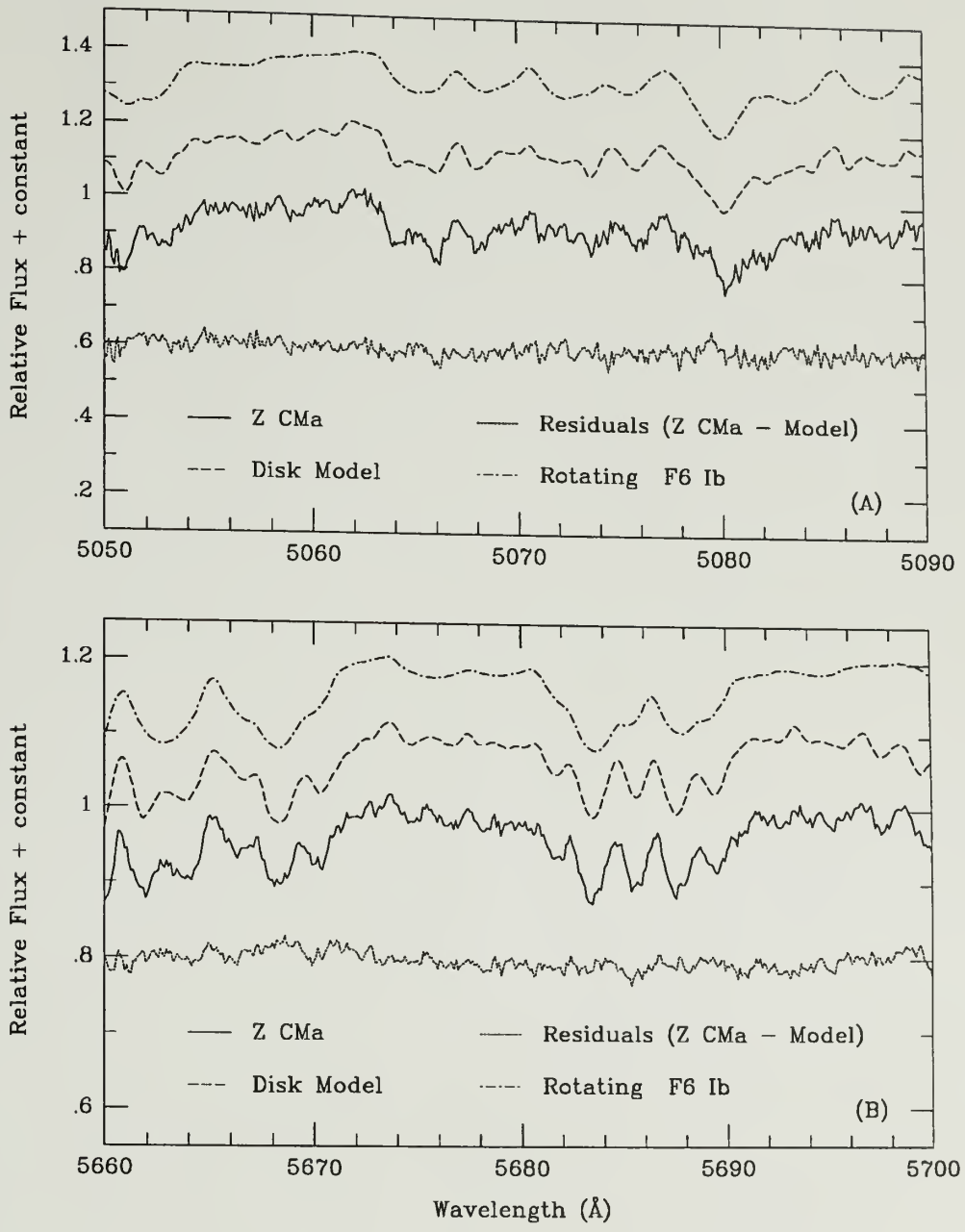

Figure 13. Z CMa data, model, residuals, and rotating F6 Ib star. The large projected rotational velocity of Z CMa ($v_{rot} \sin i \gtrsim 90\,\mathrm{km\,s^{-1}}$) enhances the observed line doubling. In these two regions the synthetic disk spectrum reproduces the observed line spectrum of Z CMa quite well. The rotating star (broadened to match overall linewidths) is unable to match most features. Even line strengths are poorly represented by the rotating star. In these panels, this is most obvious in the feature at 5698 Å. The lower panel in particular, illustrates the model's ability to reproduce the observed line spectrum in fairly blended regions, where the rotating star completely fails. Some weak residual features are apparent. Only stronger residual features, which appear at other wavelengths, will be discussed in any depth.

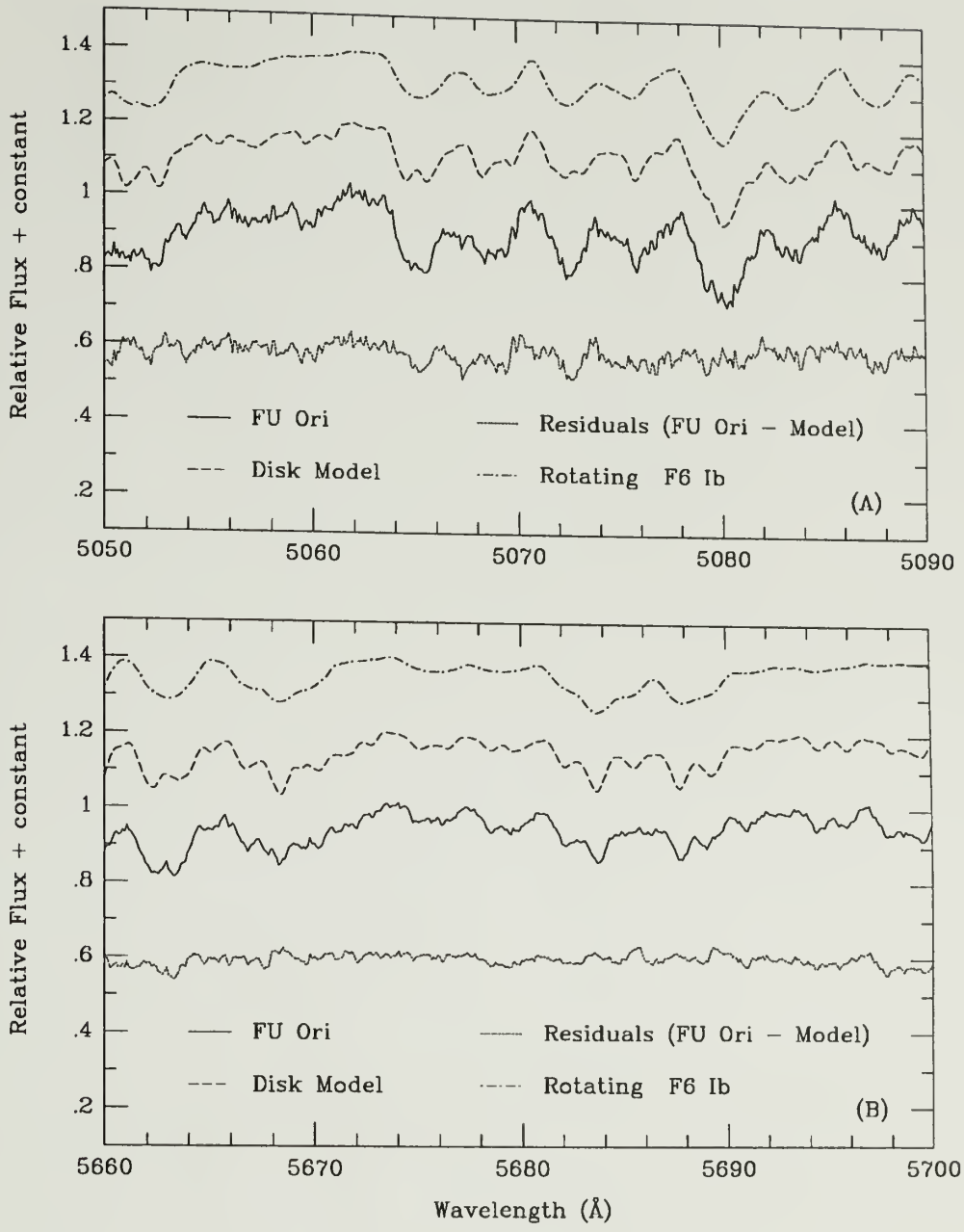

Figure 14. FU Ori data, model, residuals, and rotating F6 Ib star. The projected rotational velocity of FU Ori ($v_{rot} \sin i \sim 60\,\mathrm{km\,s^{-1}}$) is sufficient to produced significant doubling in synthetic line profiles. Even so, the accretion disk model is not able to adequately reproduce FU Ori's line spectrum at these wavelengths. We believe a strong non-disk component, *e.g.*, wind contribution, is present. We also believe the surface gravity of FU Ori's disk is lower than that of the standard stars (generally class Ib, see Table 6) used for spectrum synthesis (see Chapter 7). Still, the disk model provides a better match than a rotating star model. The residual spectrum of FU Ori will be discussed in Chapter 7.

Cyg and Z CMa. Quantitative results from our goodness of fit test for the entire wavelength range observed are presented in the next section. We note that a single rotating star does not provide a better representation of the FU Ori spectrum than the synthetic disk spectrum, and is clearly inferior to the disk model longward of 5500 Å.

The goodness of fit in Figures 12 and 13, while impressive, may be fortuitous. As discussed in Chapter 4, the models ideally should be, but have not been, constructed using standards whose linewidths are smaller than the instrumental resolution, and whose line strengths have not been strongly affected by effects such as microturbulence in the stellar atmosphere. A finer grid of such standards, spanning the full range required by the model, would be desirable. Also, the final model depends on the accuracy of the continuum normalization for the standards and the model program output. Nevertheless, our crude models do very well for V1057 Cyg and Z CMa, as their residual spectra indicate. It is clear that a single, normal rotating star is inadequate to account for the line profiles in any of our program objects.

Goodness of Fit: Method and Results

Not all regions of the Z CMa and V1057 Cyg spectra are matched by the model as well as the regions shown in Figures 12 and 13. There are, in fact, significant residual features in the difference spectra at some wavelengths. Figures 15 and 16 show some of these features for Z CMa and V1057 Cyg, respectively. We wish to determine disk model parameters which minimize the extent to which these features are present in our residual spectra, and to quantify the overall goodness of fit of our final, best models.

The method we have chosen to quantify the goodness of synthetic spectrum fit allows some subjectivity to remain, but has the advantage of being simple. We search each residual spectrum order for sets of consecutive pixels that each deviate from zero in the same direction by more than some threshold value. We leave identification and discussion of individual residual features selected in this way to Chapter 7. Next, we search the object spectra in

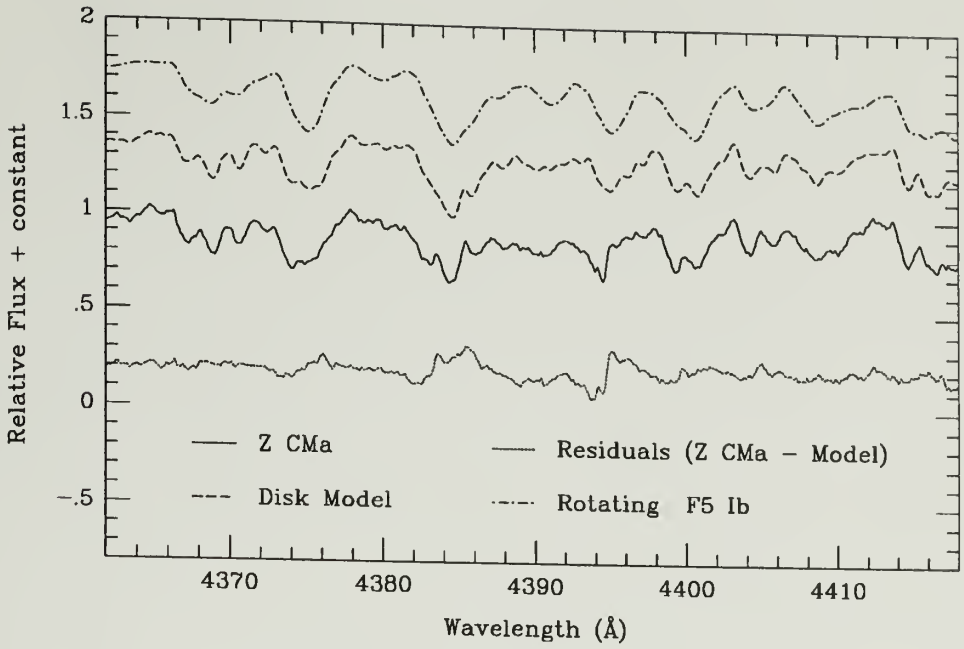

Figure 15. Z CMa data, model, residuals, and rotating F5 Ib star. In this region of the spectrum of Z CMa, significant residual features are common.

similar fashion for deviations from unity. Let n_r be the number of pixels in residual features, and let n_l be the number of pixels in absorption lines in the corresponding portion of object spectrum; then $f = 1 - (n_r/n_l)$ is our estimate of goodness of fit. This quantity is essentially the fraction of absorption lines that are well matched by the synthetic profiles. In some cases (*e. g.*, the Hα region) broad features in object spectra can cause f to be spuriously low (see Figure 17). In extreme cases negative values are possible. The subjectivity of this method lies in what threshold is used (what the value is, and whether it is the same for each spectral order), and in the number of consecutive pixels exceeding the threshold required to flag a residual feature.

To illustrate the method's sensitivity to residual features, we have calculated the goodness of fit estimate for the portions of Z CMa spectrum shown in Figures 13 and 15, requiring 6 consecutive pixels to deviate at least 0.02 from zero. The value of f is 1.00 for 5050–

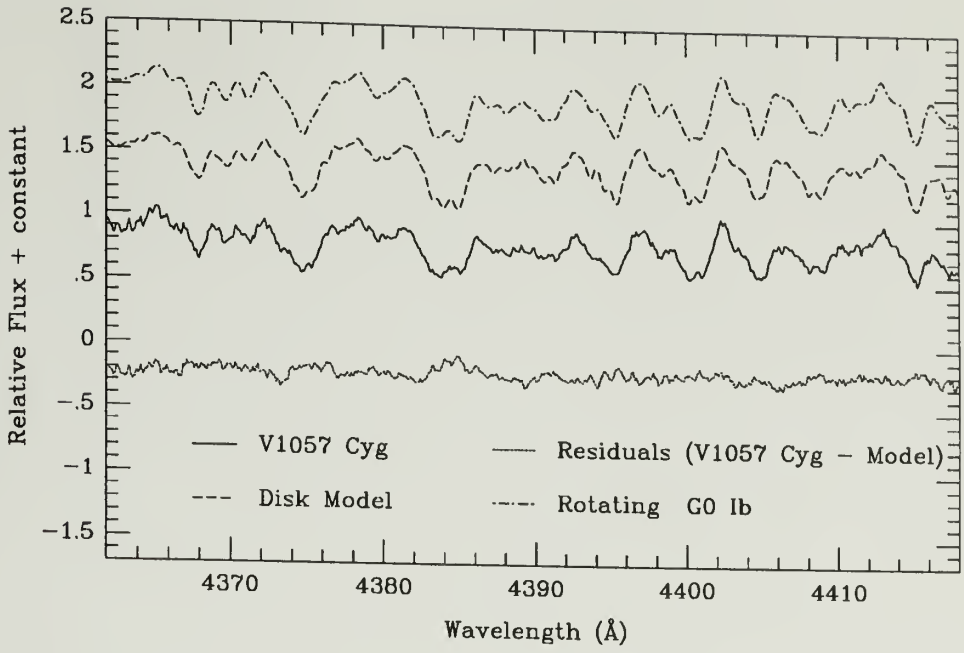

Figure 16. V1057 Cyg data, model, residuals, and rotating G0 Ib star. A few of the residual features seen in Z CMa (Figure 15) are apparent here too (*e.g.*, λ4374 Å and λ4384 Å). Residual features of Ti II lines that are strong in Z CMa (*e.g.*, λ4394 Å) are weak in the V1057 Cyg residual spectrum.

5090 Å, 1.00 for 5660–5700 Å, and 0.64 for 4362–4418 Å. $f < 1$ occurs in the first two cases if we relax the conditions for flagging features.

Complete results for our program objects appear in Table 10 and Figure 17. In these calculations we have used our best synthetic disk models (determination of model parameters is given in the next section), and define a residual feature as one having at least 6 consecutive pixels deviating at least 0.02 from zero. We use the same value for the threshold for all spectral orders, rather than, for example, some multiple of the rms noise, σ, for each order, so that we will not bias the results by requiring stronger (per pixel) residual features in orders that have higher noise levels. Even so, results for the relatively low signal-to-noise orders (the first half dozen or so in the 3985–4920 Å and 4940–6830 Å regions) are less reliable than for high SNR orders. The value of the threshold we used, 0.02, is equal to 5σ for

Table 10. Goodness of fit results. The goodness of fit is defined in the text. It is essentially the percentage of absorption lines that are well fit. Requirements for identification of residual features are that 6 or more consecutive pixels deviate from 0 by at least 0.02 (5σ for the highest signal-to-noise order, where σ is the rms noise in each spectral order.)

λ_{start}(Å)	λ_{end}(Å)	V1057 Cyg	Z CMa	FU Ori
3990	4030	0.69	0.60	0.33
4030	4060	0.65	0.70	0.43
4060	4090	0.77	0.53	0.22
4090	4120	0.53	0.33	0.24
4120	4150	0.69	0.61	0.36
4150	4185	0.60	0.65	0.19
4185	4212	0.67	0.68	0.27
4212	4240	0.49	0.44	0.08
4240	4273	0.73	0.45	0.18
4273	4305	0.34	0.20	0.06
4305	4328	0.38	0.27	0.06
4328	4362	0.42	0.31	0.19
4362	4403	0.57	0.51	0.20
4403	4440	0.68	0.52	0.20
4440	4475	0.52	0.61	0.15
4475	4510	0.60	0.49	0.29
4510	4545	0.66	0.45	0.17
4545	4585	0.57	0.27	0.24
4585	4625	0.69	0.66	0.24
4625	4665	0.78	0.50	0.12
4665	4700	0.93	0.76	0.42
4700	4740	0.53	0.52	0.25
4740	4780	0.70	0.58	0.28
4780	4835	0.75	0.56	0.37
4835	4875	0.41	0.38	0.29
4875	4916	0.69	0.36	0.00
4940	5000	0.90	0.78	0.39
5000	5050	0.82	0.74	0.54
5050	5090	0.84	0.98	0.74
5090	5140	0.73	0.87	0.51
5140	5190	0.71	0.50	0.47
5190	5236	0.72	0.73	0.50
5236	5286	0.90	0.66	0.64
5286	5336	0.89	0.71	0.36
5336	5388	0.86	0.80	0.55
5388	5440	0.84	0.78	0.69
5440	5490	0.79	0.71	0.40
5490	5540	0.84	0.90	0.71
5540	5600	0.95	0.92	0.65
5600	5655	0.98	0.92	0.56
5655	5710	0.89	0.97	0.82
5710	5770	0.98	0.97	0.89

Continued, next page.

Table 10 *(continued)*

λ_{start}(Å)	λ_{end}(Å)	V1057 Cyg	Z CMa	FU Ori
5770	5825	0.98	0.75	0.73
5825	5900	0.75	0.41	0.69
5900	5955	1.00	1.00	0.92
5955	6020	0.93	0.97	0.86
6020	6080	0.94	1.00	0.71
6080	6155	0.90	0.78	0.82
6155	6220	0.93	0.82	0.96
6220	6275	0.78	0.59	0.89
6320	6365	0.85	0.80	0.84
6365	6435	0.85	0.74	0.81
6435	6510	0.87	0.76	0.82
6510	6590	0.21	0.07	0.55
6590	6655	0.75	0.85	0.84
6664	6730	0.89	0.63	0.84
6745	6815	0.94	0.92	0.80
8030	8130	0.61	0.72	0.93
8395	8495	0.63	-0.10	0.69
8520	8630	0.44	0.35	0.80
8655	8765	0.34	0.35	0.77
8795	8905	0.63	0.60	0.87

our highest signal-to-noise order, and corresponds to a lower limit on strengths of residual features ranging from ~8 mÅ at 4000 Å, to ~17 mÅ at 9000 Å.

Several comments on the contents of Table 10 are in order. Sections of observed spectral orders were chosen to cover the entire range of wavelength observed, except for regions heavily contaminated by telluric features, without overlapping. In no case is the end of an order, corrupted by velocity shifts among input standards and convolution with the broadening function, included in the calculations.

The values of f are particularly small in the 4090 Å, 4305 Å, 4835 Å, and 6510 Å entries, indicating poor overall fit, due to the inclusion of Balmer lines in those sections. Similarly, the 5825 Å entry includes the Na I D lines. The 4273 Å and 4305 Å entries also have low values of f because strong CH features make proper continuum normalization of synthetic and object spectra extremely uncertain. The overall fit is quite good in the 4950–6820 Å region; the average f for the range is 0.85 for V1057 Cyg, 0.76 for Z CMa, and

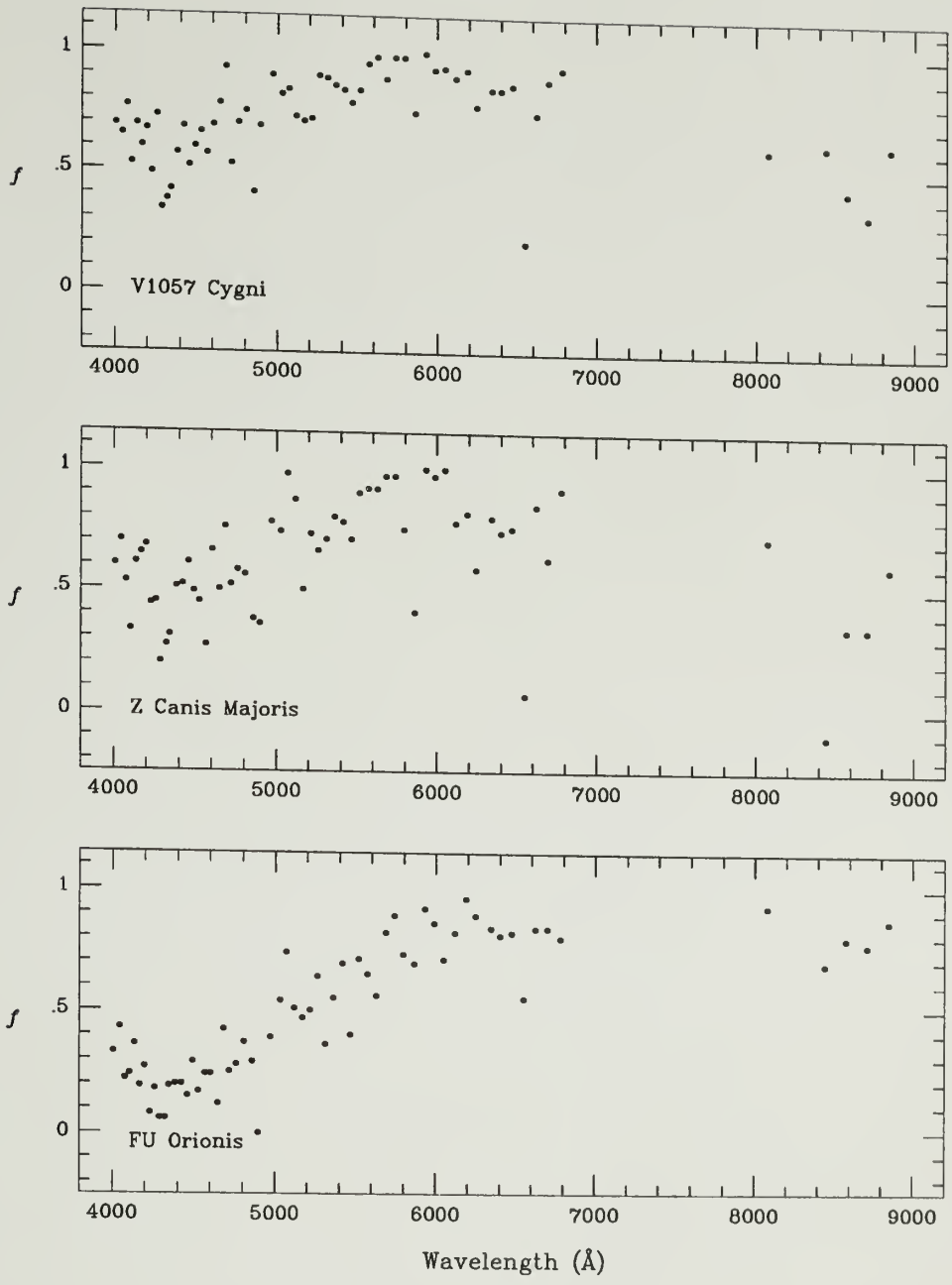

Figure 17. Goodness of fit, f, as a function of wavelength. These figures, which contain the information in Table 10, show that the goodness of fit, f, increases from $\lesssim 0.5$ at 4000 Å to $\gtrsim 0.8$ at 5000–6800 Å in V1057 Cyg and Z CMa. For FU Ori, $f \sim 0.1$ at 4000 Å, rising to $\gtrsim 0.8$ at 6000 Å and longward. Low points due to Na I D and Hα lines are apparent for all three objects. In the 8000–9000 Å region of V1057 Cyg and Z CMa we believe effects due to flared disks are responsible for the observed decline in f. The $f < 0$ point at 8445 Å in Z CMa has also been affected by the presence of Paschen emission lines. The upturn at the short wavelength end arises from the interaction of relatively high noise and the residual feature selection criterion.

0.68 for FU Ori. In the "blue" spectral region the overall fit is not as good because residual features are apparently more common at shorter wavelengths.

Determination of Best Model Parameters

The possibility that errors in model input parameters are responsible for producing the residual spectrum must be investigated before any interpretation of features is warranted. Our goodness of fit scheme allows us to determine the best values for model input parameters (T_{max}, v_{max}, and v_{rad}), assuming that having the best overall fits to the observed spectra implies that we have the best representations of the actual *disk* spectra. We have applied our goodness of fit test to a grid of synthetic spectra covering parameter space near the values used by KHH and Hartmann *et al.* (1989). Testing that region of parameter space is appropriate because their results have been shown to be reasonable approximations. We test regions of the spectrum that appear to be generally well fit (large value of f; 4940–6815 Å for V1057 Cyg and Z CMa, 5900–6815 Å for FU Ori) so our varying of parameters will *introduce* false residual features when parameter values are bad, and not simply alter profiles of real residual features. The synthetic disk spectra we have been considering to this point are those calculated using the best T_{max}, v_{max}, and v_{rad} determined here. The next three sub-sections describe the effects of errors in v_{max}, v_{rad}, and T_{max} individually, followed by summaries of the goodness of fit tests for each object. Additional discussion of temperature and gravity sensitivity of individual residual features will be given in Chapter 7.

Effects Due to Error in Rotational Velocity Normalization

If the rotational velocity normalization (v_{max}) is in error, a distinctive signature appears in the difference spectra. Figure 18 illustrates the effect. In it, we have subtracted two T_{max} = 6590 K synthetic spectra, having v_{max} = 45 km s^{-1} and 55 km s^{-1}, from another, which represents a "perfect" FU Ori object spectrum, whose only difference is that v_{max} = 50 km s^{-1}. This v_{max} = 50 km s^{-1} model is included for comparison. If lines in the synthetic

spectrum being subtracted are too broad, a profile similar to an impact crater cross section is produced (bottom), with a total equivalent width of zero. The effect of subtracting a synthetic spectrum whose lines are narrower than those of the "object" is essentially a "crater profile" upside down (middle).

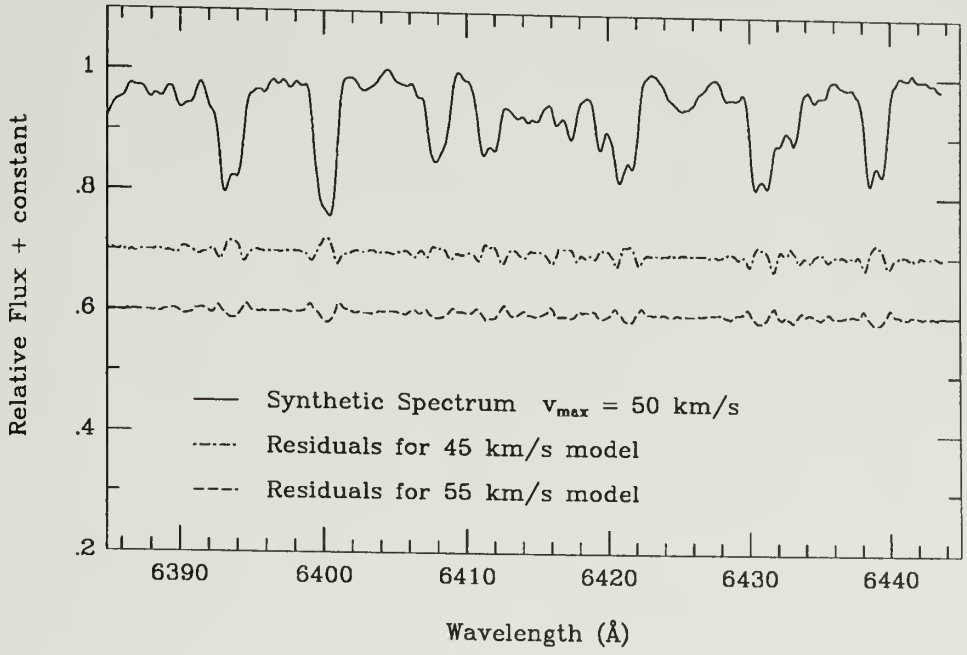

Figure 18. Simulation of rotational velocity error. We have subtracted from a v_{max} = 50 km s^{-1}, T_{max} = 6590 K model (top) two models differing only in v_{max} to illustrate the effect of rotational velocity scale normalization errors on residual spectra. Distinctive "crater profiles" appear in the residual spectra when the model rotates more rapidly than the "object" (bottom), and inverse "crater profiles" when the model rotates more slowly (middle).

In our residual spectra there are no "crater" profiles. There are few residual features that resemble the inverted crater profiles, and their absorption components are generally weak with respect to the central emission, *i.e.*, the total equivalent widths of such residual features is significantly non-zero. Thus it appears that error in rotational velocity scale is not a significant contributor to features in the difference spectra.

Effects Due to Error in Radial Velocity

In the case of a radial velocity error, a P Cygni-like residual feature is expected. Figure 19 shows that such residual profiles will have peculiar structure, because the synthetic disk profiles are relatively complex. In Figure 19 we have subtracted one synthetic spectrum with T_{max} = 7200 K and v_{max} = 50 km s^{-1} from another that differs only by a radial velocity shift. We have illustrated the effect of shifts of 5 km s^{-1} and 10 km s^{-1}. The minima and maxima for unblended residuals of this type occur at the velocities of the wings of the original lines. This is roughly the case for many of the residual features, especially in the Z CMa difference spectra. The structure of those residual features is not the same as the features caused here by radial velocity offset, but we wish to demonstrate further that such features in the residual spectra do not arise from radial velocity errors.

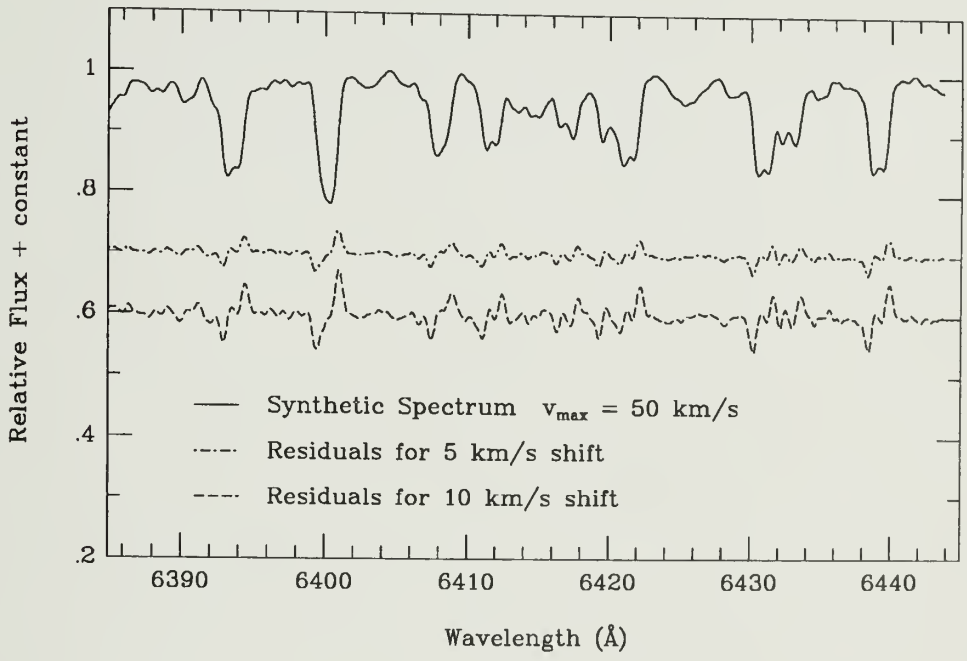

Figure 19. Simulation of radial velocity error. We have subtracted from a v_{max} = 50 km s^{-1}, T_{max} = 7200 K model (top) models differing only in a radial velocity shift to illustrate the effect of radial velocity error on the residual spectra. The two examples shown are for shifts of +5 km s^{-1} and +10 km s^{-1}.

In Figure 20 we demonstrate that radial velocity error is not responsible for P Cygni type residual features, or structure within such profiles. We plot, for the same wavelength range as in Figure 15, the Z CMa residual spectra for several models which differ only in the velocity shift applied. Each spectrum is labeled with the shift used, in $\mathrm{km\,s^{-1}}$. The shift we have used for our "best" Z CMa model in this region is $12.8\,\mathrm{km\,s^{-1}}$, which corresponds to the cloud velocity (see Chapter 3 for an explanation of the calibration of the shift). Regions where the fit to absorption lines is relatively good turn into totally unacceptable wiggles when large excursions from this value are employed. Even for errors several times the small range of acceptable shifts ($\sim 3\,\mathrm{km\,s^{-1}}$, allowing a 0.02 decline in f from its maximum value), the structure in features such as λ4394 Å persists.

Effects Due to Error in Disk Temperature Scale

The final input parameter for disk model calculation is the maximum disk temperature, T_{max}, which occurs at $R = 1.36 R_\star$ (LBP), and is used as the temperature of the innermost annulus in the synthesis of model spectra. The synthetic spectra in Figures 18 and 19 are otherwise identical models of T_{max} = 6590 K and 7200 K, respectively. We point out in particular the difference in the degree of blending of the features near λ6432 Å, and the degree of doubling of the line at λ6439 Å. The grid of models for the T_{max} tests use weight tables for 7980 K, 7500 K, 7200 K (Table 5), 7065 K, 6930 K, 6800 K, 6590 K (Table 4), and 6370 K.

Goodness of Fit Test Results for V1057 Cygni

The portion of our goodness of fit tests showing that input parameters for the V1057 Cyg model have been constrained appears in Table 11, in which f is given as a function of input parameters for the entire 4940–6815 Å range. These results suggest that $T_{max} \approx$ 6825 K $\pm$250 K, if we allow values of f within 0.02 of the maximum. We have chosen T_{max} = 6590 K as the best temperature because f is maximized for that value, and KHH

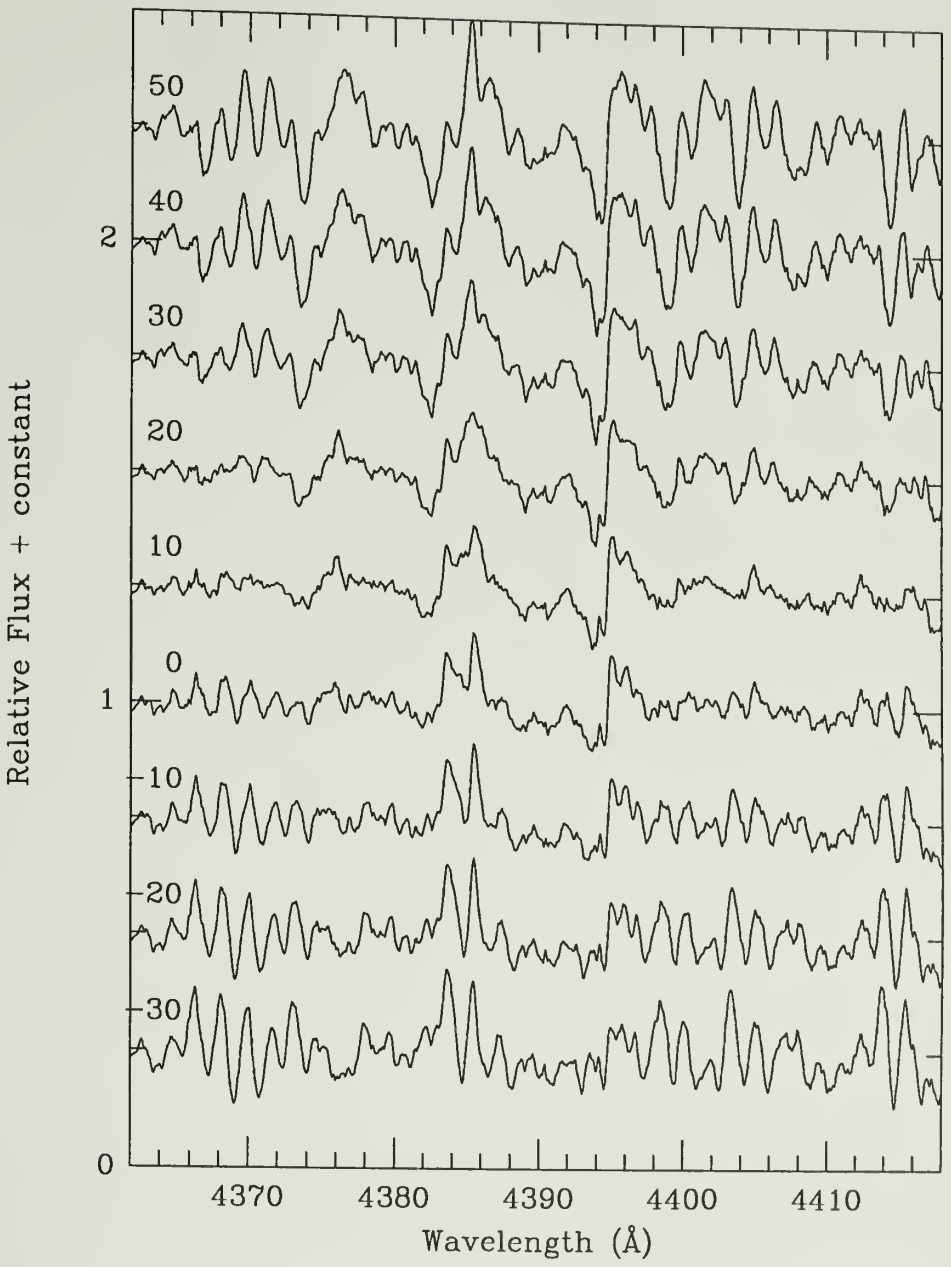

Figure 20. Z CMa residual spectra for different radial velocity models. Synthetic spectra with T_{max} = 7200 K and v_{max} = 115 km s^{-1}, differing only in radial velocity shift (inside left border) have been subtracted from the corresponding Z CMa spectrum. Very large radial velocity shifts would be required to obliterate the structure in lines such as λ4395 Å. Such shifts are clearly unacceptable in view of their effect on the overall fit.

found that a 6590 K model provides the best fit to the broadband energy distribution of V1057 Cyg from 4000 Å to $\sim$10 μm. Photometric changes from the time of their observations (late

Table 11. Goodness of fit test results for V1057 Cyg. For points in model parameter space whose f-value is near the maximum value found. The radial velocity shift (column 3) is with respect to the local interstellar gas (see Chapter 3). The maximum value of f is found for T_{max} = 6590 K, v_{max} = 48 km s^{-1}, and 0 km s^{-1} shift. Note that models with T_{max} up to 400 K higher, and v_{max} as much as 6 km s^{-1} higher fit almost as well.

T_{max} (K)	v_{max} (km s^{-1})	v_{rad} (km s^{-1})	f
6370	48	0	0.79
6370	51	0	0.79
6590	42	0	0.76
6590	45	0	0.81
6590	48	0	0.847
6590	51	0	0.830
6590	54	0	0.81
6800	45	0	0.81
6800	48	0	0.841
6800	51	0	0.839
6800	54	0	0.831
6930	45	0	0.81
6930	48	0	0.842
6930	51	0	0.839
6930	54	0	0.831
7065	45	0	0.81
7065	48	0	0.840
7065	51	0	0.834
7065	54	0	0.79
7200	48	0	0.79
7200	51	0	0.77
6590	48	−10	0.72
6590	48	−5	0.80
6590	48	+5	0.82
6590	48	+10	0.76

1984) until ours (1988 November) do not support an increase in disk temperature (Simon and Joyce 1988; S. Kenyon, private communication).

In terms of rotational velocity, we find that f is a maximum at v_{max} = 48 km s^{-1}, and that v_{max} = 51 km s^{-1} is acceptable, with values up to 54 km s^{-1} permitted for hotter models, allowing values of f no more than 0.02 below the maximum value. Our cross-correlation analysis (see Chapter 5) showed that 48 km s^{-1} is the best value for v_{max} for the 6590 K model. The value of v_{max} used by KHH (43.6 km s^{-1}, determined by cross-correlation analysis of their 1984 spectra) is clearly excluded. Our 1986, 1988, and 1989 spectra have

revealed that absorption lines in the spectrum of V1057 Cyg have increased through at least that period, consistent with the increase in v_{max} required here. This increase in linewidths with time will be the subject of a subsequent paper.

Using the 0.02 decline in f criterion, we find that the radial velocity of V1057 Cyg must be within $\sim$3 km s^{-1} of +15 km s^{-1}, the radial velocity of neighboring interstellar material. Table 11 shows results of v_{rad} tests only for T_{max} = 6590 K and v_{max} = 48 km s^{-1}; results for other values of these parameters show a similar trend, but with smaller values of f.

Goodness of Fit Test Results for Z Canis Majoris

In the case of Z CMa, we find a more limited set of acceptable parameter combinations (see Table 12). A model with T_{max} = 7200 K, v_{max} = 115 km s^{-1}, and zero velocity shift with respect to local material maximizes f in the 4940–6815 Å region. Our next hotter model (T_{max} = 7500 K) rotating $\sim$5% faster (v_{max} = 121 km s^{-1}) is almost as good. The actual maximum disk temperature and inner rotational speed are probably between these values, *i. e.*, $T_{max} \sim$ 7350 K $\pm$ 200 K, $v_{max} \sim$ 118 km s^{-1} $\pm$ 3 km s^{-1}. For this study, no appropriate weight table was available, so we have used the 7200 K, 115 km s^{-1} model which maximizes f here.

As is the case with V1057 Cyg, for all T_{max}, v_{max} pairs, the radial velocity of Z CMa is constrained to be within $\sim$3 km s^{-1} of the local interstellar gas. In Table 12 we have shown the v_{rad} test results only for the 7200 K, 115 km s^{-1} model.

Goodness of Fit Test Results for FU Orionis

FU Ori's maximum disk temperature also appears reasonably well constrained by our goodness of fit test results, shown in Table 13. If models for which f is within 0.02 of its maximum value are acceptable, T_{max} = 7200 K $\pm$ $\sim$350 K, in agreement with the FU Ori temperature scale determined by HK2.

Table 12. Goodness of fit test results for Z CMa. For points in model parameter space whose f-value is near the maximum value found. The radial velocity shift (column 3) is with respect to the local interstellar gas (see Chapter 3). The maximum value of f is found for T_{max} = 7200 K, v_{max} = 115 km s^{-1}, and 0 km s^{-1} shift. Note that the 7500 K, 121 km s^{-1} model fits almost as well. We do not currently have a weight table suitable for testing intermediate values.

T_{max} (K)	v_{max} (km s^{-1})	v_{rad} (km s^{-1})	f
6930	109	0	0.59
6930	115	0	0.63
7065	109	0	0.66
7065	115	0	0.73
7065	121	0	0.70
7200	109	0	0.67
7200	115	0	0.76
7200	118	0	0.73
7200	121	0	0.72
7500	115	0	0.69
7500	118	0	0.69
7500	121	0	0.75
7500	127	0	0.72
7980	121	0	0.64
7980	127	0	0.65
7200	115	−10	0.69
7200	115	−5	0.72
7200	115	−2	0.74
7200	115	+2	0.73
7200	115	+5	0.72
7200	115	+10	0.68

The goodness of fit is maximized for the 7200 K model when v_{max} = 85 km s^{-1}. Values as low as 80 km s^{-1} are almost as good. We have used 85 km s^{-1} as the best value because it maximizes f, and our cross-correlation analysis favors it over smaller values.

The FU Ori spectrum synthesis in KHH used v_{max} = 93 km s^{-1}. We have examined our FU Ori spectra obtained in 1986, 1988, and 1989 and find no significant change in linewidths. Although their spectra were obtained in 1984 with different instrumentation, we are puzzled by the difference in rotational velocity scale required, given the recent stability of FU Ori's line spectrum and photometry.

As for our other program objects, the radial velocity of FU Ori is constrained to be within ~3 km s^{-1} of the local interstellar gas.

Table 13. Goodness of fit test results for FU Ori. For points in model parameter space whose f-value is near the maximum value found. The radial velocity shift (column 3) is with respect to the local interstellar gas (see Chapter 3). The maximum value of f is found for T_{max} = 7200 K, v_{max} = 85 km s^{-1}, and 0 km s^{-1} shift. Note that models with T_{max} higher or lower by as much as ~350 K, and with v_{max} as low as 80 km s^{-1} are almost as good.

T_{max} (K)	v_{max} (km s^{-1})	v_{rad} (km s^{-1})	f
6590	85	0	0.78
6800	80	0	0.79
6800	85	0	0.80
6930	80	0	0.80
6930	85	0	0.814
6930	90	0	0.80
7065	75	0	0.80
7065	80	0	0.826
7065	85	0	0.821
7065	90	0	0.80
7200	70	0	0.78
7200	75	0	0.80
7200	80	0	0.826
7200	85	0	0.829
7200	90	0	0.817
7200	95	0	0.74
7500	75	0	0.79
7500	80	0	0.826
7500	85	0	0.828
7500	90	0	0.807
7980	80	0	0.68
7980	85	0	0.62
7200	85	−10	0.79
7200	85	−5	0.818
7200	85	+5	0.808
7200	85	+10	0.75

CHAPTER 7

ANALYSIS OF RESIDUAL FEATURES

Identification of Residual Features

The first step in analyzing the residual spectra is simply to compile a list of the residual featues for each program object. This is accomplished as part of the goodness of fit procedure described in Chapter 6. Tables 14, 15, and 16 are partial lists of the residual features found in V1057 Cyg, Z CMa, and FU Ori, respectively. Only those features whose equivalent widths are ≥ 125 mÅ are included for V1057 Cyg and Z CMa, and ≥ 200 mÅ for FU Ori. The corresponding complete lists are presented in the Appendix. In each case, six consecutive pixels each at least 0.02 from zero were required to flag a residual feature. Each entry includes the beginning and ending wavelengths of the feature (*i. e.*, only those wavelengths within which the feature is at least 0.02 from zero, not true extents), an indication of the type of feature (A for absorption, E for emission; lower case is used to indicate that the feature is an absorption or emission component of a P Cygni type feature, as judged by visual inspection of the residual spectrum), and identification information for relatively unblended features where possible. In some cases visual inspection of the residual spectrum clearly suggests that the *full* wavelength range given is not due to the line specified. We plot each of the identified features on a common velocity scale in Figures 21, 22, and 23.

The lists of residual features will be useful for answering several questions. In the following sections we will use them to discuss the appropriateness of using supergiants for spectrum synthesis (gravity sensitivity), and verify our choices of maximum disk temperatures. The peculiar profiles apparent in many of the residual profiles, of Z CMa in particular, will be the focus of cursory discussion of the properties of the winds driven by the FU Ori objects. This subject will be taken up in greater detail in a subsequent paper.

Table 14. Strong residual features in V1057 Cyg. All features found to have $W_\lambda \geq 125$ mÅ are listed here. Columns 1 and 2 give the wavelength range spanned by each feature. Column 3 gives an indication of the feature type: "A" for absorption and "E" for emission, with lower case indicating a component of a P Cygni feature. Column 4 gives the equivalent width of each feature, a number of which are blended. If a single spectral line seems to account for a feature, identification information is given in columns 5, 6, and 7. A "T" or "g" in column 8 indicates that a feature is particularly sensitive to temperature or gravity, respectively (see text).

λ_{start}	λ_{end}	Type	W_λ (Å)	λ	ID	RMT	Comment
3993.484	3994.322	A	0.138				
4004.800	4006.058	E	0.152	4005.25	Fe I	43	
4026.036	4027.503	A	0.251				
4029.970	4031.517	E	0.188	4030.76	Mn I	2	
4032.783	4034.541	E	0.183	4033.07	Mn I	2	
4062.881	4064.581	E	0.175	4063.61	Fe I	43	
4076.907	4078.253	E	0.149	4077.72	Sr II	1	
4097.967	4101.248	a	0.455	4101.75	Hδ		
4101.604	4106.312	e	0.693	4101.75	Hδ		
4212.680	4214.885	a	0.143				
4226.130	4228.115	e	0.197	4226.74	Ca I	2	T
4322.364	4324.846	a	0.254	4325.77	Fe I	42	
4336.305	4339.941	a	0.525	4340.48	Hγ		
4340.168	4346.229	e	0.762	4340.48	Hγ		
4383.742	4385.269	e	0.130	4383.56	Fe I	41	
4387.483	4390.233	A	0.167				
4405.309	4407.694	A	0.147				
4499.903	4502.797	A	0.155	4501.28	Ti II	31	
4545.086	4548.899	a	0.251	4549.64	Ti II	82	
4562.006	4564.072	A	0.140	4563.77	Ti II	50	
4726.938	4730.549	A	0.169				
4850.094	4860.870	a	2.262	4861.34	Hβ		
4861.039	4867.521	e	0.797	4861.34	Hβ		
4884.557	4887.445	A	0.144				
5050.301	5052.511	E	0.164	5051.64	Fe I	16	
5163.119	5165.097	a	0.172				
5225.745	5228.105	E	0.173	5227.19	Fe I	37	
5268.774	5270.424	E	0.166	5269.55	Fe I	15	
5327.369	5329.033	E	0.173	5328.05	Fe I	15	
5885.562	5888.934	a	0.918	5889.97	Na I D_2	1	
5889.139	5889.751	e	0.164	5889.97	Na I D_2	1	
5890.467	5891.387	e	0.214	5889.97	Na I D_2	1	
5891.898	5894.861	a	0.507	5895.94	Na I D_1	1	
5895.066	5895.679	e	0.177	5895.94	Na I D_1	1	
5896.395	5897.927	e	0.219	5895.94	Na I D_1	1	
6514.891	6517.516	E	0.125	6516.05	Fe II	40	T
6546.041	6560.988	a	7.303	6562.81	Hα		
6561.331	6571.486	e	2.460	6562.81	Hα		

Continued, next page.

Table 14 *(continued)*

λ_{start}	λ_{end}	Type	W_λ (Å)	λ	ID	RMT	Comment
6706.630	6709.316	A	0.241	6707.76	Li I	1	
8039.933	8042.156	E	0.136				
8411.301	8414.336	E	0.203	8412.36	Ti I	33	
8425.175	8427.343	E	0.161	8426.51	Ti I	33	
8433.847	8436.304	E	0.277	8434.97	Ti I	33	
8464.340	8466.941	E	0.131				
8494.400	8495.412	a	0.044	8498.06	Ca II	2	
8496.135	8499.604	e	1.557	8498.06	Ca II	2	
8539.850	8551.371	E	2.694	8542.13	Ca II	2	
8617.694	8621.092	A	0.132				
8660.294	8676.044	e	2.849	8662.19	Ca II	2	
8678.444	8684.444	E	0.362				
8687.294	8690.295	E	0.241	8688.64	Fe I	60	
8803.910	8807.868	E	0.199	8806.78	Mg I	7	
8822.787	8825.527	E	0.190	8824.23	Fe I	60	
8835.879	8839.837	E	0.213	8838.45	Fe I	339	

Gravity Sensitivity

Most FU Ori object spectral type determinations that include luminosity class assign class I or II to them (see Herbig 1977). There is some suggestion, however, that FU Ori objects (FU Ori in particular) may be characterized by gravity *lower* than that of supergiants (HK1, KHH). The structure of residual features that are particularly sensitive to gravity may enable us to better determine the appropriate luminosity class of the FU Ori objects. If an FU Ori *disk* has gravity *lower* than that of the standards used for spectrum synthesis, its absorption lines will generally be deeper than corresponding synthetic lines. In the absence of significant non-disk contributions, we therefore expect to find *absorption* features in the residual spectrum. No peculiar line shapes should be caused by such line strength mismatch alone.

We determine which spectral lines are particularly sensitive to gravity by comparing a supergiant and a giant of roughly the same temperature (to avoid temperature sensitive lines). Standards employed were observed during the 1988 November observing runs unless noted

Table 15. Strong residual features in Z CMa.

λ_{start}	λ_{end}	Type	W_λ (Å)	λ	ID	RMT	Comment
4024.483	4026.578	E	0.125	4025.13	Ti II	11	
4062.723	4065.273	e	0.204	4063.61	Fe I	43	
4065.486	4068.815	E	0.184				
4093.029	4100.090	a	1.611	4101.75	Hδ		
4100.304	4108.292	e	1.478	4101.75	Hδ		
4177.407	4181.027	E	0.280	4178.86	Fe II	28	
4221.556	4225.525	a	0.175	4226.74	Ca I	2	T
4226.407	4228.612	e	0.184	4226.74	Ca I	2	T
4232.140	4235.080	e	0.300	4233.17	Fe II	27	
4321.971	4324.903	a	0.260	4325.77	Fe I	42	
4327.805	4339.016	a	3.348	4340.48	Hγ		
4339.243	4346.514	e	1.170	4340.48	Hγ		
4350.832	4353.181	E	0.172	4351.92	Mg I	14	
4383.189	4386.167	E	0.232	4383.56	Fe I	41	
4387.695	4391.208	A	0.164				
4392.124	4394.491	a	0.197	4395.04	Ti II	19	
4394.644	4396.629	e	0.153	4395.04	Ti II	19	
4410.216	4419.451	E	0.566				
4440.458	4443.250	a	0.178	4443.81	Ti II	19	
4465.591	4467.918	a	0.202	4468.50	Ti II	31	g
4472.417	4474.822	E	0.173	4472.92	Fe II	37	
4474.941	4478.147	E	0.139				
4494.880	4500.823	a	0.463	4501.28	Ti II	31	
4531.034	4533.398	a	0.165	4533.97	Ti II	50	g
4545.625	4548.643	a	0.220	4549.64	Ti II	82	
4548.961	4551.264	e	0.229	4549.64	Ti II	82	
4554.839	4559.208	E	0.300				
4560.955	4563.259	a	0.154	4563.77	Ti II	50	
4577.875	4582.562	a	0.214	4583.84	Fe II	38	
4582.800	4584.865	e	0.190	4583.84	Fe II	38	
4608.500	4611.784	E	0.148				
4618.513	4622.357	E	0.155				
4704.678	4709.684	A	0.223				
4754.980	4759.202	A	0.145				
4785.133	4790.725	A	0.245				
4846.706	4860.092	a	5.522	4861.34	Hβ		
4860.260	4868.848	e	2.212	4861.34	Hβ		
4880.630	4886.830	A	0.284				
4889.293	4893.031	A	0.154				
4908.065	4911.803	A	0.172				
5014.311	5017.026	a	0.191	5018.43	Fe II	42	
5017.289	5022.458	e	0.836	5018.43	Fe II	42	
5158.813	5167.357	A	1.058				
5167.897	5170.686	e	0.425	5169.03	Fe II	42	
5171.044	5174.013	E	0.188				

Continued, next page.

Table 15 *(continued)*

λ_{start}	λ_{end}	Type	W_λ (Å)	λ	ID	RMT	Comment
5182.647	5184.355	e	0.129	5183.60	Mg I	2	
5196.894	5198.619	E	0.146	5197.58	Fe II	49	g
5226.029	5228.389	e	0.169	5227.19	Fe I	37	
5233.472	5235.377	E	0.155	5234.62	Fe II	49	g
5268.969	5270.895	e	0.131	5269.55	Fe I	15	
5315.362	5318.505	E	0.335				
5804.005	5810.276	A	0.217				
5878.217	5889.355	a	3.342	5889.97	Na I D_2	1	
5891.093	5895.283	a	1.523	5895.94	Na I D_1	1	
5896.203	5898.553	e	0.335	5895.94	Na I D_1	1	
6147.039	6150.981	E	0.221				
6237.810	6240.642	E	0.135	6238.38	Fe II	74	g
6246.742	6249.683	E	0.129	6247.56	Fe II	74	g
6429.957	6434.191	E	0.262				
6455.480	6458.073	E	0.188	6456.38	Fe II	74	
6514.906	6517.530	E	0.246	6516.05	Fe II	40	g
6538.411	6560.432	a	7.563	6562.81	Hα		
6560.774	6582.111	e	15.081	6562.81	Hα		
6705.828	6709.681	A	0.195	6707.76	Li I	1	
8410.841	8414.310	E	0.242	8412.36	Ti I	33	
8425.003	8427.460	E	0.128	8426.51	Ti I	33	
8433.241	8437.576	E	0.322	8434.97	Ti I	33	
8442.635	8448.994	E	1.015	8446.36	O I	4	
8464.457	8470.383	E	0.340	8468.43	Fe I	60	
8489.604	8495.239	a	0.517	8498.06	Ca II	2	
8495.528	8499.431	e	3.393	8498.06	Ca II	2	
8532.143	8538.198	a	0.316	8542.13	Ca II	2	
8538.789	8550.312	e	5.899	8542.13	Ca II	2	
8596.987	8599.499	E	0.150	8598.39	H I	9	
8654.867	8659.066	a	0.451	8662.19	Ca II	2	
8659.517	8668.218	e	4.887	8662.19	Ca II	2	
8687.269	8690.268	E	0.166	8688.64	Fe I	60	
8746.370	8752.971	E	0.379	8750.48	H I	9	
8804.493	8808.755	E	0.259	8806.78	Mg I	7	
8822.455	8825.804	E	0.185	8824.23	Fe I	60	
8859.294	8864.470	E	0.347	8862.79	H I	9	

otherwise. Of the standard star spectra available to us, the following were the best pairs for near equivalence in temperature and consistency among the three wavelength regions observed: ϵ Gem (G8 Ib) and β Gem (K0 III) for the 4000–4920 Å region, SAO 22820 (K0 Ib) and 46 LMi (K0 III; 1988 January) for the 5125–6830 Å region, and ϵ Gem (G8 Ib) and η

Table 16. Strong residual features in FU Ori.

λ_{start}	λ_{end}	Type	W_λ (Å)	λ	ID	RMT	Comment
4043.719	4046.039	a	0.250	4045.83	Fe I	43	
4075.741	4078.292	a	0.259	4077.72	Sr II	1	
4098.077	4101.500	a	1.005	4101.75	Hδ		
4101.786	4109.204	e	1.120	4101.75	Hδ		
4141.352	4144.371	a	0.289	4143.88	Fe I	43	
4174.639	4178.042	A	0.339				
4212.941	4216.174	a	0.521	4215.54	Sr II	1	
4221.761	4227.861	A	0.845	4226.74	Ca I	2	
4229.037	4233.814	A	0.532				
4235.211	4239.841	A	0.414				
4244.830	4247.643	A	0.427				
4247.791	4251.123	A	0.371				
4251.937	4256.602	A	0.671	4254.35	Cr I	1	
4270.373	4272.150	a	0.215	4271.77	Fe I	42	
4272.951	4275.413	A	0.367	4274.81	Cr I	1	
4287.574	4290.334	A	0.300	4289.73	Cr I	1	
4322.180	4327.820	A	0.729	4325.78	Fe I	42	
4336.348	4340.135	a	1.133	4340.48	Hγ		
4340.666	4343.998	e	0.504	4340.48	Hγ		
4344.453	4346.346	E	0.219				
4372.559	4375.231	a	0.284	4375.94	Fe I	2	
4378.973	4384.165	A	0.505	4383.56	Fe I	41	
4387.678	4392.031	A	0.307				
4392.565	4395.772	A	0.422	4395.04	Ti II	19	
4402.889	4409.814	A	0.765				
4432.824	4436.594	A	0.278				
4440.053	4444.475	a	0.362	4443.81	Ti II	19	
4453.861	4460.532	A	0.503				
4465.729	4469.996	A	0.586				
4487.591	4491.892	A	0.257				
4492.830	4497.444	A	0.335				
4498.147	4502.057	A	0.447	4501.28	Ti II	31	
4510.763	4515.885	A	0.443				
4516.595	4518.959	A	0.227				
4524.160	4529.992	A	0.414	4528.63	Fe I	68	
4530.544	4536.375	A	0.684				
4538.582	4542.128	A	0.235				
4544.812	4550.135	A	0.718				
4553.232	4554.821	A	0.228				
4561.335	4564.433	A	0.330	4563.77	Ti II	50	
4570.550	4572.457	a	0.215	4571.98	Ti II	82	
4581.194	4584.292	a	0.201	4583.84	Fe II	38	g
4585.014	4587.977	A	0.274				
4593.184	4598.710	A	0.467				
4599.432	4608.002	A	0.638				

Continued, next page.

Table 16 *(continued)*

λ_{start}	λ_{end}	Type	W_λ (Å)	λ	ID	RMT	Comment
4624.780	4629.947	A	0.323				
4635.276	4641.816	A	0.451				
4642.058	4652.716	A	0.759				
4653.847	4657.479	A	0.227				
4678.058	4682.779	A	0.240				
4704.085	4710.732	A	0.421				
4711.717	4716.396	A	0.249				
4726.326	4730.511	A	0.276				
4755.044	4759.929	A	0.276				
4763.737	4769.036	A	0.311				
4787.785	4793.126	A	0.297				
4854.938	4861.000	a	1.988	4861.34	Hβ		
4861.252	4868.155	e	0.730	4861.34	Hβ		
4880.101	4906.178	A	1.792				
4906.518	4912.293	A	0.423				
4967.129	4973.467	A	0.377				
4974.422	4979.284	A	0.300				
5015.866	5018.844	a	0.537	5018.45	Fe II	42	
5162.118	5169.583	A	0.862				
5170.392	5173.360	A	0.419	5172.20	Mg I	2	
5180.465	5184.422	A	0.876	5183.62	Mg I	2	
5203.587	5209.033	A	0.421				
5222.284	5227.185	A	0.273				
5294.169	5303.043	A	0.537				
5313.397	5317.095	a	0.275	5316.62	Fe II	49	
5364.248	5371.998	A	0.514				
5477.969	5481.873	A	0.222				
5557.678	5563.505	A	0.218				
5885.752	5889.330	a	1.558	5889.97	Na I D_2	1	
5890.249	5891.986	e	0.270	5889.97	Na I D_2	1	
5892.292	5895.358	a	1.387	5895.94	Na I D_1	1	
5896.176	5898.118	e	0.260	5895.94	Na I D_1	1	
6555.041	6561.772	a	2.233	6562.81	Hα		
6562.000	6570.215	e	1.723	6562.81	Hα		
6704.514	6709.417	A	0.385	6707.76	Li I	1	
8493.363	8496.109	a	0.200	8498.06	Ca II	2	
8496.398	8499.288	e	0.957	8498.06	Ca II	2	
8537.316	8540.418	a	0.377	8542.13	Ca II	2	
8540.713	8550.020	e	2.279	8542.13	Ca II	2	
8657.571	8660.422	a	0.303	8662.19	Ca II	2	
8660.722	8668.821	e	1.845	8662.19	Ca II	2	

Cyg (K0 III, 1989 December) for the 8030–9000 Å region. Note that the 4940–5125 Å range is not represented because we have no appropriate class III standard at those wavelengths.

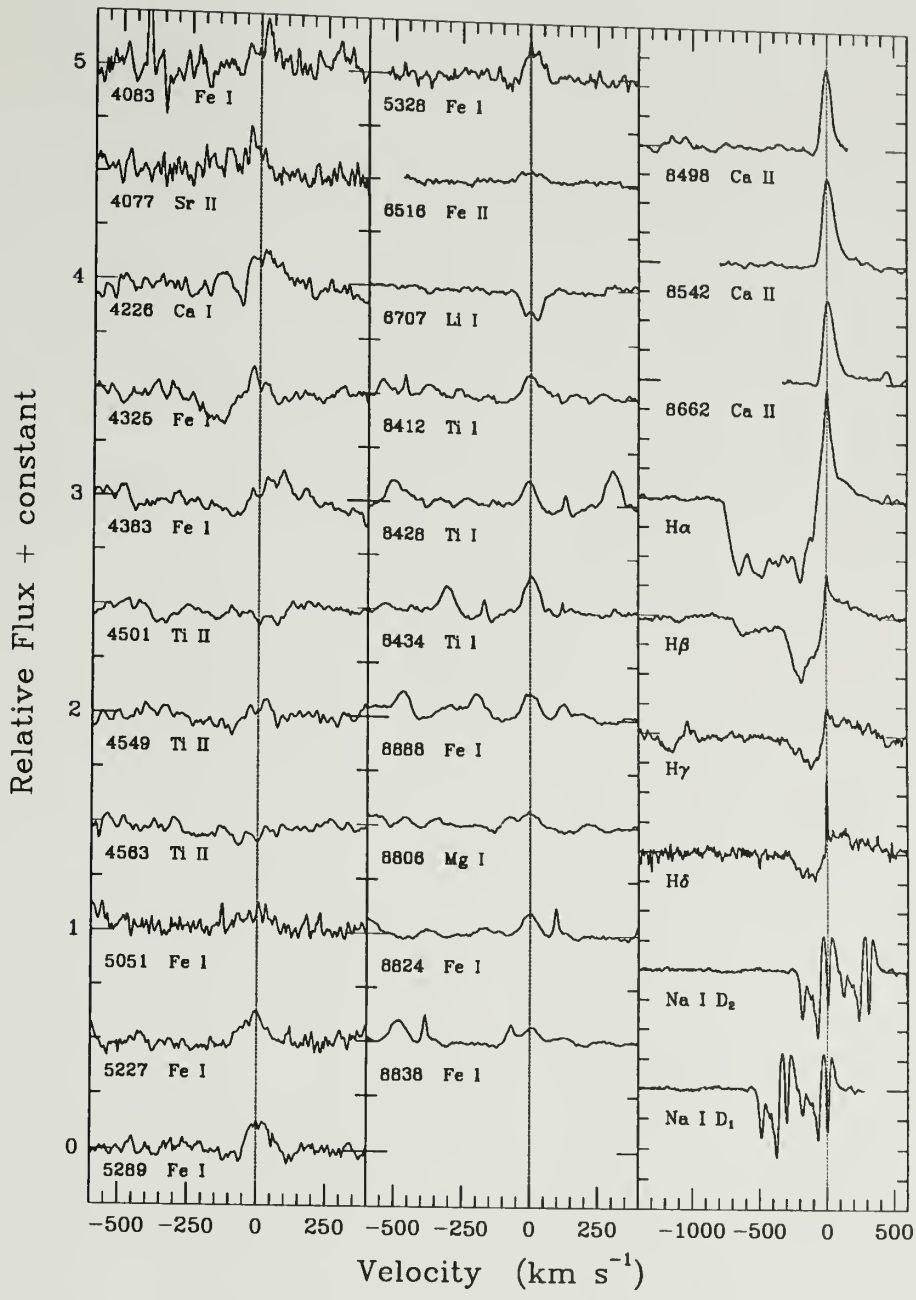

Figure 21. Strong features in the residual spectrum of V1057 Cyg. The λ4005 Å, λ4030 Å, and λ4033 Å lines are not included because the very poor signal-to-noise destroys any useful visual impression of those lines. Note that the vertical scale in the third panel is such that features are separated by the full continuum height.

We measure the equivalent widths of a sample of lines in each standard. The sample includes all the strong residual features for which we are confident of identifications (*i. e.*, those

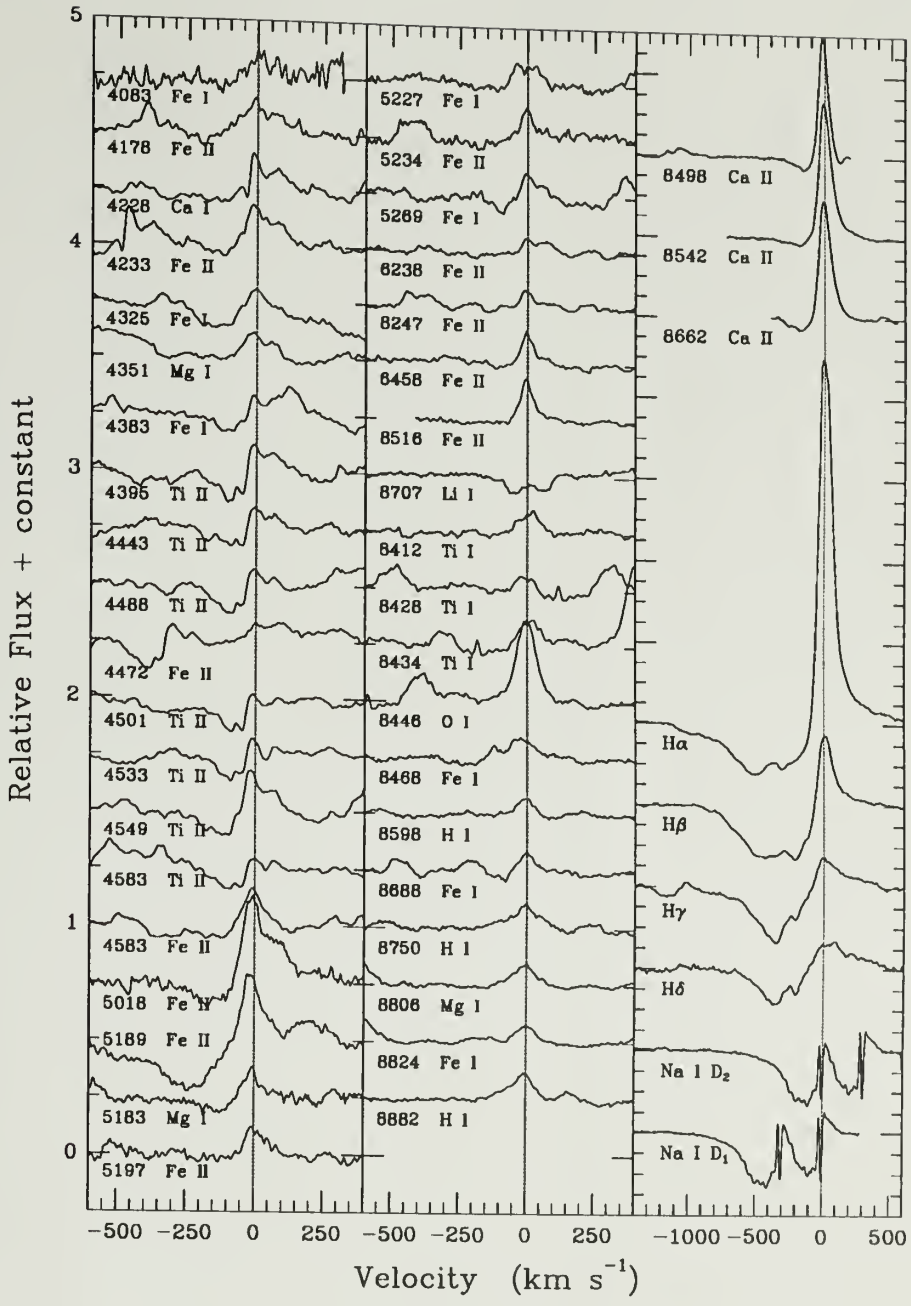

Figure 22. Strong features in the residual spectrum of Z CMa. The λ4025 Å lines is not included because poor signal-to-noise destroys any useful visual impression. In the third panel, the full continuum height is given by the separation of the major tick marks.

that appear in Figures 21, 22, and 23), and as a pseudo-control group, the lines represented in our linewidth *vs.* wavelength and linewidth *vs.* excitation potential plots. A particularly gravity sensitive spectral line is defined arbitrarily as one for which the ratio of equivalent

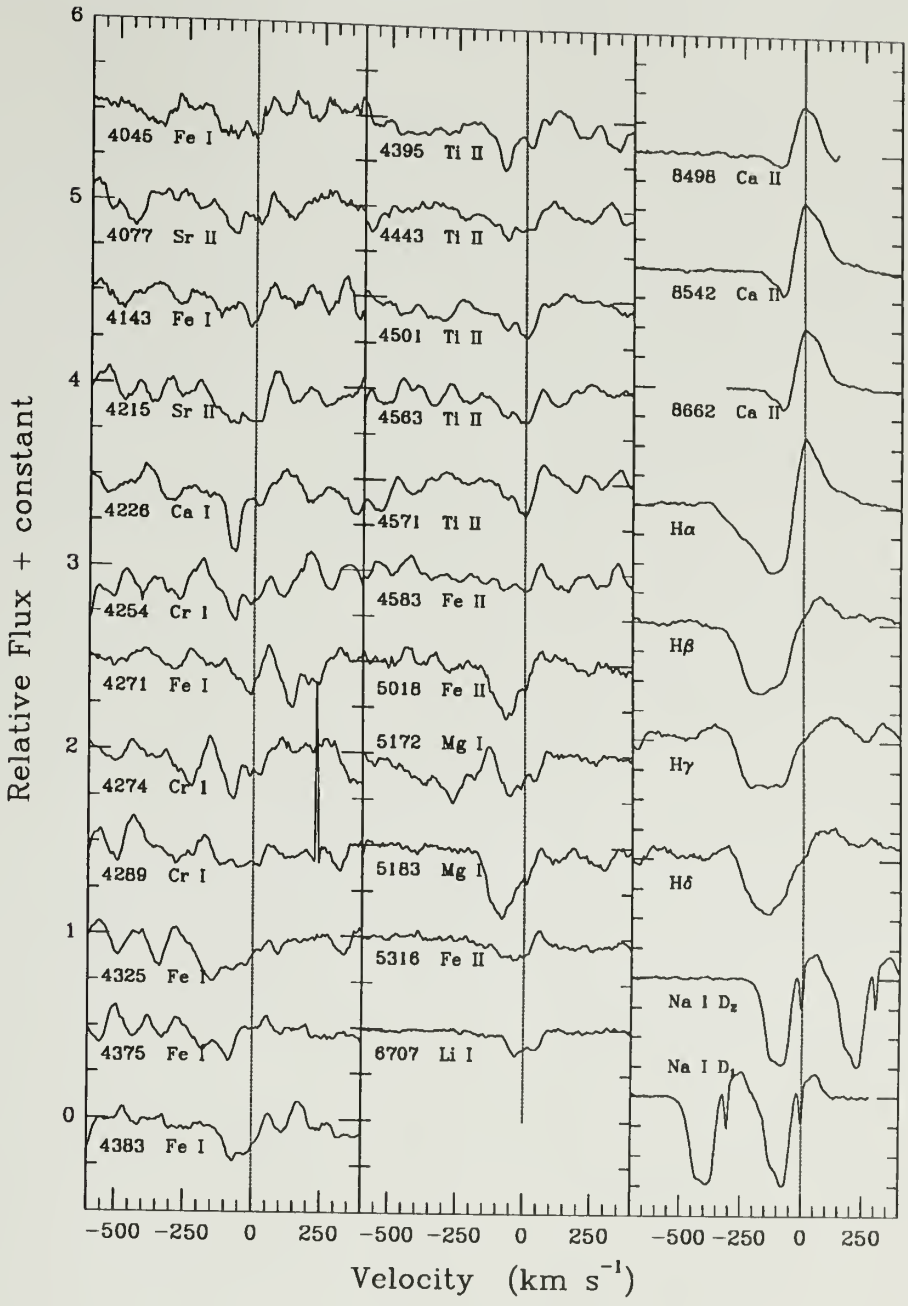

Figure 23. Strong features in the residual spectrum of FU Ori. In the third panel, the full continuum height is given by the separation of the major tick marks.

widths in the supergiant and the giant is greater than 3.0. We find a total of 17 such lines. The ratio for the majority of lines in the sample ranges from 1.5 to 2.5. In general, as one would expect, lines from ionized species tend to have a larger equivalent width ratio than

lines from neutral species. There are no lines in the sample that are significantly stronger in the giant than in the supergiant. All particularly gravity sensitive lines in the sample that correspond to strong residual features are indicated by a "g" in the last column in Tables 14, 15, and 16. We have not carried out this analysis for the complete Tables (Appendix) because we believe uncertainties in, for example, continuum normalization make such identifications less useful when weaker residual features are considered.

Very few of the lines most sensitive to gravity appear in the lists of strong residual features. The λ6707 Li I line, strong in the spectra of FU Ori objects (and in the residual spectra) because of their youth, is noted as being particularly sensitive to gravity in our analysis. This is due to an anomalously strong Li I line in the K0 Ib standard, so we have not flagged that line as gravity sensitive in the Tables. No lines in Table 14 (V1057 Cyg) are flagged as especially gravity sensitive. In Table 15 (Z CMa) 7 lines are flagged: 2 Ti II and 5 Fe II lines. Both Ti II lines have obvious P Cygni structure. The Fe II lines are emission only, at the systemic velocity, but are narrower than typical photospheric absorption lines. We believe they are weak, quiescent state versions of the strong emission lines seen during a small (0.5 mag) outburst in 1987 February (Hessman *et al.* 1991). Only one P Cygni feature in Table 16 (FU Ori) is identified as particularly gravity sensitive. If our standard stars are of inapproprate gravity and the disk dominates the spectrum, we expect residual gravity sensitive features to have profiles similar to those of disk absorption lines. Thus we find no evidence from this analysis that the surface gravity of our program objects differs radically from the stars we used for spectrum synthesis.

The relative proportions of absorption and emission residuals give us additional information. Since most absorption lines are stronger in lower gravity stars, an absorption residual would suggest that the object has lower surface gravity than the synthetic spectrum. Shortward of 6000 Å in V1057 Cyg and Z CMa there is a slight preference for emission residuals. Longward of 6000 Å, non-P Cygni residuals are almost exclusively emission features. While this suggests these objects possess gravity higher than that of supergiants, especially

at longer wavelengths, it may be that physical conditions which violate the assumpions of the disk model are responsible for the presence of residual emission features. For example, Kenyon and Hartmann (1987) note that outer portions of a flared disk may lack a significant temperature gradient perpendicular to the disk midplane due to additional surface heating from the inner disk. So a flared disk can account for the observed behavior: the inner portion produces lines more readily than the outer regions, so far-red lines would appear weak with respect to corresponding synthetic lines, producing emission residuals, while the match at shorter wavelengths is better.

The behavior in FU Ori is different. Of the 57 strong, non-P Cygni residuals in Table 16, 56 are absorption features. Roughly 67% of all features in the corresponding complete list are in absorption (50% in V1057 Cyg and Z CMa). While this suggests gravity lower than that of supergiants, as Hartmann and Kenyon (HK1) suggest is the case, it is not conclusive. Strong absorption in the FU Ori wind may be responsible.

Temperature Sensitivity

Although we have used our goodness of fit test to determine the best T_{max} values to use in synthetic disk calculations, we can test our results further by analysis similar to that for gravity sensitivity. With the supergiants in the previous section, we used β Aqr (G0 Ib), SAO 22740 (G2 Ib), and μ Per (G0 Ib) for the 3985–4920 Å, 4940–6830 Å, and 8030–9000 Å regions, respectively. To flag an especially temperature sensitive line, we require an equivalent width ratio greater than 2.75. We find 17 such lines in the sample of 180, while most lines have a ratio between 1 and 2. We remove the λ6707 Li I line from consideration for the same reason as above. Features in Tables 14, 15, and 16 which correspond to the strongly temperature dependent lines are indicated by a "T" in the last column.

Only 2 of the 17 most temperature sensitive lines appear in the strong residual feature lists. The λ4226 Ca I line appears as a P Cygni residual in V1057 Cyg and Z CMa, and the λ6516 Fe II line is in emission in the V1057 Cyg residual spectrum. So we find no significant

evidence that we have made an error in disk temperature scale normalization for any of our program objects, in agreement with results in Chapter 6.

Description of Residual Features

All the analysis of the residual spectra to this point has led to the conclusion that the features present in the residual spectra of our program objects are intrinsic to those systems, and not due to errors in disk model parameters or to peculiar sensitivity to physical conditions in the sources. The presence of obvious wind signatures in the Na I D, Balmer, and infrared Ca II triplet, and the P Cygni structure of many of the residual features leads us to interpret the residual features as additional signatures of the powerful FU Ori winds. We wish to know whether they hold any information that can be used to better determine the properties of those winds. Here we offer descriptions of trends seen in the residual features in each object, and in the next section offer a suggestion for the origin of those trends. Detailed treatment is left to a subsequent paper.

V1057 Cygni

As noted above, most of the far-red residual features in V1057 Cyg are emission features centered at the systemic velocity, suggesting more than anything else, departure from simple disk model assumptions in the outer disk. We will therefore ignore those features. At the shortest wavelengths meaningful structure is apparent in the strongest residuals. Many of them (*e.g.*, the first 8 in Figure 21) have two distinct peaks at $\sim\pm30\,\mathrm{km\,s^{-1}}$, and many have P Cygni absorption extending to $\sim-200\,\mathrm{km\,s^{-1}}$. This double peaked structure and blue absorption become less apparent toward longer wavelengths.

In the Na I D and Balmer lines, the model subtraction has enhanced the P Cygni appearance of the lines. We note the very distinct components present in the Na I D lines (the zero velocity features are probably of interstellar origin), and the decrease in maximum wind speed through the Balmer series, probably a signature of wind acceleration.

Z Canis Majoris

The higher signal-to-noise ratio in our Z CMa spectra, and relative strength of residual features allows a more detailed description of this object's residual spectrum. The gross description is similar to that for V1057 Cyg: at short wavelengths there are many P Cygni profiles with doubled emission, changing to pure emission features at longer wavelengths. The details are different, however, and additional structure is present in some lines.

In Figure 24 we show the average of all the unblended (as judged by visual inspection and comparison with line lists) residual features for two Fe I multiplets. The upper profile (5 lines from Fe I multiplet 43, $\lambda \sim 4300$ Å) shows a distinct pair of emission peaks, at $-5\,\mathrm{km\,s^{-1}}$ and $+64\,\mathrm{km\,s^{-1}}$. The blue absorption extends to $-200\,\mathrm{km\,s^{-1}}$, and the red wing to $+110\,\mathrm{km\,s^{-1}}$. In the middle profile (9 lines from Fe I multiplet 15, $\lambda \sim 5400$ Å) the distinct red emission has become a shoulder on the main $0\,\mathrm{km\,s^{-1}}$ peak. The blue absorption extends to $-170\,\mathrm{km\,s^{-1}}$, and the red wing to $+90\,\mathrm{km\,s^{-1}}$. Many of the other residual features follow the same basic pattern.

The bottom profile in Figure 24 is the average of the Ti II lines in Figure 22 ($\lambda \sim 4500$ Å). Here we see the doubled emission, but additional structure is present within the blue absorption. It is structure such as this that we believe may ultimately enable us to determine the structure of the Z CMa wind.

The behavior of the Balmer lines is similar to that in V1057 Cyg in indicating the acceleration of the wind to very high velocity.

FU Orionis

Because of the uncertainty in the origin of the residuals in FU Ori (gravity mismatch or wind), and because of the severe blending apparent even in the features we have tentatively identified (see Figure 24), we are not at this time in a position to discuss any constraints on wind properties in FU Ori. We will, however, point out some trends apparent in the residuals.

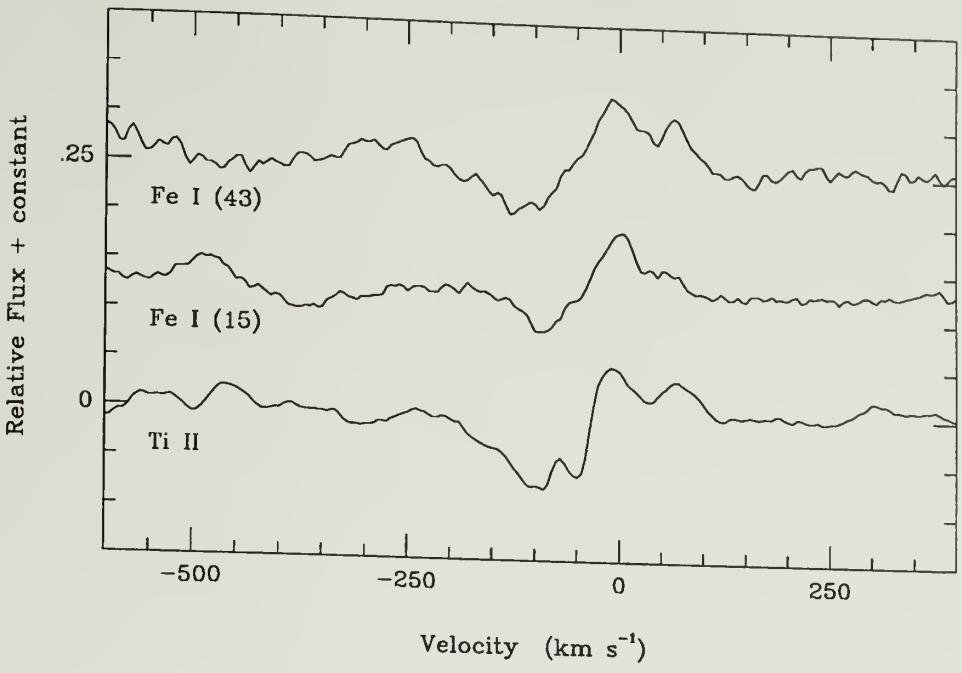

Figure 24. Z CMa residual Fe I and Ti II lines. Here we plot the average of 5 Fe I, multiplet 43 (top), 9 Fe I, multiplet 15 (middle) residuals, and the average of all 7 strong Ti II residuals (bottom). Note the P Cygni structure, double emission peak, and the structure in the blue absorption in the Ti II lines.

Herbig (1977) identified a number of "shell" features, displaced $\sim$80 km s^{-1} blueward, in spectra of FU Ori. Several of these are apparent in our residual spectrum: λ4077, λ4215, λ4226, λ4254, λ4274, λ4395, λ5018, and λ5183. This component is apparent in several other of our residuals (see Figure 24). Most of the features in the first two panels of Figure 24 also have an emission peak at $\sim$+65 km s^{-1}.

Constraint of Wind Properties

The first possibility to consider is that the wind is an accelerating radial outflow, arising from the central star itself. Wind lines formed against the background continuum of the inner disk may have different characteristics than those formed against the outer disk, due to different column densities of material and different velocities of material along lines of

sight to different parts of the disk. However, it is difficult to imagine any way to produce the structure seen in many of the residual features.

Another simple geometry to consider is that of a wind arising from the surface of the disk, and accelerating in the z direction (normal to the disk midplane). With this non-diverging velocity structure, it is difficult to understand any structure in lines at red-shifted velocities, since only blue-shifted material would be seen. This initial objection is removed if the disk wind is allowed to diverge somewhat so that the inclination of the system to our line of sight allows for red-shifted outflow. In this case, the situation is not too unlike a radial outflow, in terms of line profiles that might be produced.

If we consider that the velocity stucture of a disk wind will probably initially have a *rotational component*, more complicated line profiles may result. In particular, in this scenario wind absorption may be similar to line formation in the disk itself: rotation of "annuli" in the wind may produce doubled absorption. Such lines will be blue shifted by $v_z \cos i$, where v_z is the z-component of the wind velocity, which will vary with height z above the disk and with distance from the rotation axis.

Calculation of wind profiles assuming these and other configurations is beyond the scope of the present work. In particular, the latter case above will be a complex computational problem. We plan to persue such calculations in future work.

CHAPTER 8

CONCLUSIONS

Summary of Results and Conclusions

We have used high resolution, high signal-to-noise optical spectra to investigate the applicability of the accretion disk hypothesis to the FU Ori objects. That hypothesis suggests that in outburst, FU Ori objects are self-luminous accretion disks, whose light dominates at optical and near-infrared wavelengths. Such a disk ideally has a characteristic radial temperature gradient, $T(R) \propto R^{-3/4}$, and a Keplerian rotation curve. If each point of such a disk radiates as a star of type appropriate to the local temperature, the net line spectrum should contain signatures of its temperature and velocity structure.

We have investigated predicted correlations between linewidth and both wavelength and lower excitation potential in synthetic and observed FU Ori object spectra. Strong evidence has been found for linewidth *vs.* wavelength correlation in good agreement with model prediction for V1057 Cyg and Z CMa, but not for FU Ori itself. We emphasize that linewidth varies *continuously* with wavelength at optical wavelengths in the former two objects. In the case of FU Ori, we argue that a combination of strong wind components to spectral lines, and surface gravity lower than that of supergiants (used in calculation of synthetic spectra), conceals the underlying linewidth *vs.* wavelength relationship.

We find marginal correlation between linewidth and lower excitation potential in all three program objects. In the case of V1057 Cyg, we confirm earlier detection of this effect. In each case we find reasonable agreement with model prediction. Apparently linewidth variation with excitation potential is a subtle effect, which is less useful than the variation of linewidth with wavelength as a diagnostic of differential rotation.

Satisfied that the accretion disk model is an adequate first order approximation to the FU Ori object spectra, we subtracted our best synthetic (model) disk spectra from the observed

spectra to produce residual spectra. A goodness of fit quantity was defined (essentially the number of object line profiles that are fit well by the synthetic disk spectral lines) to determine quantitatively how well a given model reproduces an FU Ori object spectrum. We defined the best model for each object as that which maximizes the goodness of fit. For those best models, ~80% of spectral features are well fit (to ~10 mÅ accuracy) in regions of the spectrum not strongly affected by non-disk components (~5500–6800 Å). It is these best models that were used for the linewidth *vs.* wavelength and excitation potential comparisons, and for all subsequent analysis.

Based on their structure, as well as the goodness of fit testing, we verify that residual features present are intrinsic to the FU Ori systems, and not due to errors in model parameters or peculiar sensitivity to physical conditions. These residual features are interpreted as signatures of the powerful winds driven by FU Ori objects.

We argue that complex residual line structure, evident most clearly in Z CMa, is real and probably does not arise in a simple radial outflow arising from the central star (or innermost portions of the disk). The suggestion that the wind is ejected by the disk meets the same objections, unless we consider that the wind, in addition to vertical acceleration and possible divergence from the rotation axis, initially has a significant rotational component. We believe it may be possible to explain the complex residual (wind) profiles in that case. In this case it is also clear that FU Ori winds would carry large amounts of angular momentum away from these systems.

Directions for Further Study

Several interesting avenues for future work are suggested by this work. Changes in FU Ori object spectra with time will be important in further confirmation of the accretion disk hypothesis. In particular, the model predicts that absorption linewidths should increase as a disk cools. We have observed this effect in our spectra of V1057 Cyg (1986 October through 1989 December). Based on just four lines, we have also noticed an increase in Z

CMa's linewidths, from 1983 December to 1988 November. From our 1986 December to 1989 November spectra of FU Ori, no such linewidth increase is seen. We will report further in a subsequent paper.

We have pointed out that our modeling could be improved by more careful selection of standard stars, and by more complete spectral type coverage. Improved modeling and improved signal-to-noise data, especially of V1057 Cyg, will be important for better determination of the residual (wind) spectra of the FU Ori objects. Such study of other members of the class will also be instructive. Once better residual spectra are available, an in depth study of the residual features, including modeling of residual spectra, will be crucial for determination of the origin of the FU Ori winds: the star or the disk.

Other issues include deviations of real physical conditions from model assumptions. In particular, the problem of possible disk flaring and its effect on the disk's line spectrum, should be investigated. Whether the radial temperature distribution of a classical accretion disk (LBP) and Keplerian velocity distribution are appropriate are questions deserving attention.

Beyond testing various models for FU Ori objects and their outbursts, effort should continue to be made to detect more such objects. Discovery of all FU Ori objects will help determine the frequency of FU Ori eruptions, and their overall importance in building up the central stars involved. Detailed observation of FU Ori outbursts as they occur will be invaluable for constraining models for the outbursts of these fascinating objects.

APPENDIX

COMPLETE RESIDUAL FEATURE LISTS

The complete lists of residual features for our three program objects are presented here. Each entry includes beginning and ending wavelengths, type of feature (A for absorption, E for emission), the number of pixels comprising the feature, and equivalent width.

While many of the features listed in the Tables below are intrinsic to the FU Ori object systems, some probably are not. Errors in continuum normalization of standard stars input to the model, the final synthetic spectra, or object spectra may be responsible for some, especially broad, shallow features (identified by low ratio of equivalent width to range of wavelength). The crude method of constructing synthetic spectra (*e.g.*, using a fairly coarse grid of spectral types) may also be responsible for some features. In the case of FU Ori, gravity mismatch may be important as well. It must also be pointed out that many of the residual features listed below are blends, and that some features may have been missed by our goodness of fit algorithm. We therefore urge that any who would make use of these Tables exercise appropriate caution, especially when the weaker features are involved.

The residual features for V1057 Cyg, Z CMa, and FU Ori appear in Tables 17, 18, and 19, respectively.

Table 17. Complete list of residual features for V1057 Cyg.

λ_{start}	λ_{end}	Type	Pixels	W_λ (Å)
3991.249	3991.807	A	9	0.092
3992.087	3992.436	A	6	0.051
3993.484	3994.322	A	13	0.138
3997.605	3998.164	E	9	0.086
3998.863	3999.282	A	7	0.032
3999.841	4000.190	A	6	0.042
4001.727	4002.146	E	7	0.034
4003.054	4003.683	E	10	0.075
4004.800	4006.058	E	19	0.152
4008.014	4008.433	E	7	0.057
4009.062	4009.481	E	7	0.041
4013.881	4014.440	E	9	0.056
4014.719	4015.208	E	8	0.061
4020.028	4020.378	A	6	0.041
4026.036	4027.503	A	22	0.251
4029.179	4029.878	A	11	0.109
4029.970	4031.517	E	23	0.188
4032.009	4032.361	E	6	0.041
4032.783	4034.541	E	26	0.183
4034.892	4035.314	E	7	0.032
4035.947	4036.509	E	9	0.062
4039.181	4039.744	E	9	0.057
4043.540	4044.103	A	9	0.040
4045.157	4045.861	E	11	0.098
4046.001	4046.423	E	7	0.050
4047.267	4047.759	A	8	0.050
4055.986	4056.337	A	6	0.048
4058.025	4058.728	A	11	0.075
4062.881	4064.581	E	25	0.175
4067.202	4068.265	E	16	0.088
4069.611	4070.107	E	8	0.032
4075.207	4075.561	E	6	0.027
4076.057	4076.482	E	7	0.049
4076.907	4078.253	E	20	0.149
4087.037	4087.391	E	6	0.036
4097.967	4101.248	A	47	0.455
4101.604	4106.312	E	67	0.693
4106.455	4107.953	E	22	0.104
4108.880	4110.735	E	27	0.092
4111.662	4112.019	E	6	0.018
4114.872	4115.443	A	9	0.033
4115.585	4116.156	A	9	0.049
4118.938	4119.437	E	8	0.039
4125.780	4126.931	A	17	0.068
4127.866	4128.944	E	16	0.096
4131.317	4132.755	E	21	0.108

Continued, next page.

Table 17 *(continued)*

λ_{start}	λ_{end}	Type	Pixels	W_λ (Å)
4139.371	4140.521	A	17	0.085
4141.025	4141.744	A	11	0.043
4142.175	4142.607	A	7	0.034
4144.692	4145.052	A	6	0.030
4145.339	4145.843	A	8	0.031
4146.778	4147.281	A	8	0.035
4147.425	4148.144	A	11	0.071
4150.198	4150.560	E	6	0.024
4151.356	4151.719	E	6	0.034
4152.370	4152.732	E	6	0.022
4155.267	4155.629	E	6	0.015
4156.932	4157.512	E	9	0.052
4158.743	4159.322	A	9	0.038
4160.698	4161.929	E	18	0.082
4164.608	4165.115	A	8	0.024
4166.273	4166.708	E	7	0.023
4168.156	4169.097	A	14	0.054
4169.459	4169.894	A	7	0.028
4170.184	4170.618	E	7	0.026
4171.197	4171.560	E	6	0.031
4173.586	4174.456	E	13	0.061
4175.469	4176.121	A	10	0.037
4176.411	4176.917	A	8	0.035
4177.859	4179.379	E	22	0.106
4180.393	4180.973	A	9	0.023
4181.769	4182.131	A	6	0.020
4183.507	4184.086	E	9	0.063
4184.376	4184.738	E	6	0.030
4185.001	4185.365	A	6	0.032
4185.803	4186.387	A	9	0.029
4188.064	4188.502	E	7	0.027
4188.648	4189.158	A	8	0.028
4190.617	4190.982	E	6	0.021
4192.441	4193.170	A	11	0.029
4193.973	4194.483	A	8	0.024
4198.422	4198.933	E	8	0.031
4199.881	4201.267	A	20	0.100
4201.631	4202.580	E	14	0.057
4204.914	4205.497	E	9	0.038
4210.822	4211.187	A	6	0.032
4211.405	4211.770	A	6	0.022
4212.680	4214.885	A	31	0.143
4215.032	4216.722	E	24	0.105
4218.045	4219.442	A	20	0.092
4220.250	4220.618	A	6	0.020
4223.043	4223.778	A	11	0.049

Continued, next page.

Table 17 *(continued)*

λ_{start}	λ_{end}	Type	Pixels	W_λ (Å)
4223.925	4224.293	A	6	0.022
4224.513	4225.175	E	10	0.022
4225.322	4225.983	A	10	0.049
4226.130	4228.115	E	28	0.197
4229.438	4230.026	A	9	0.035
4230.614	4230.981	A	6	0.014
4231.496	4232.525	A	15	0.075
4232.966	4233.480	E	8	0.029
4240.568	4241.160	A	9	0.033
4245.084	4245.603	A	8	0.028
4248.046	4249.527	A	21	0.077
4249.897	4250.268	A	6	0.015
4253.155	4253.822	A	10	0.046
4255.006	4256.043	A	15	0.076
4257.524	4257.968	E	7	0.025
4259.005	4259.449	A	7	0.021
4261.522	4261.966	A	7	0.020
4267.594	4268.186	A	9	0.026
4268.408	4268.926	E	8	0.025
4271.296	4271.962	E	10	0.032
4274.924	4275.297	E	6	0.019
4276.118	4276.714	A	9	0.028
4279.102	4281.639	A	35	0.195
4281.788	4282.534	A	11	0.040
4284.176	4287.086	A	40	0.195
4287.608	4289.026	A	20	0.087
4289.399	4290.220	E	12	0.065
4290.667	4293.652	A	41	0.256
4293.875	4294.249	A	6	0.022
4294.622	4295.890	A	18	0.081
4296.487	4298.353	A	26	0.201
4298.576	4299.248	A	10	0.027
4299.472	4299.919	E	7	0.032
4300.143	4300.516	A	6	0.023
4300.964	4301.412	A	7	0.027
4301.635	4302.083	A	7	0.020
4303.127	4304.918	A	25	0.171
4304.992	4305.669	A	10	0.037
4306.121	4307.249	A	16	0.102
4308.376	4313.490	A	69	0.575
4313.641	4314.242	A	9	0.029
4318.303	4319.055	A	11	0.044
4319.206	4319.657	A	7	0.016
4321.612	4322.139	A	8	0.029
4322.364	4324.846	A	34	0.254
4325.222	4325.673	E	7	0.041

Continued, next page.

Table 17 *(continued)*

λ_{start}	λ_{end}	Type	Pixels	W_λ (Å)
4326.425	4327.553	A	16	0.053
4329.791	4330.321	E	8	0.049
4335.472	4335.927	A	7	0.024
4336.305	4339.941	A	49	0.525
4340.168	4346.229	E	81	0.762
4347.213	4347.592	A	6	0.016
4349.334	4350.395	E	15	0.045
4351.001	4352.440	E	20	0.091
4354.637	4356.910	A	31	0.122
4359.485	4361.379	A	26	0.094
4362.207	4362.588	A	6	0.021
4362.817	4363.352	A	8	0.038
4363.581	4364.116	A	8	0.038
4366.025	4366.865	A	12	0.046
4367.170	4367.552	E	6	0.014
4368.774	4369.385	E	9	0.024
4372.669	4373.738	A	15	0.101
4376.182	4376.563	E	6	0.020
4376.792	4377.480	A	10	0.038
4377.632	4378.014	A	6	0.018
4380.458	4380.916	A	7	0.028
4381.069	4382.825	A	24	0.114
4383.742	4385.269	E	21	0.130
4387.483	4390.233	A	37	0.167
4391.531	4393.517	A	27	0.104
4393.746	4394.356	A	9	0.043
4395.273	4395.655	E	6	0.019
4396.724	4397.105	A	6	0.026
4403.077	4404.308	A	17	0.083
4405.309	4407.694	A	32	0.147
4410.465	4411.003	A	8	0.022
4411.234	4411.696	E	7	0.017
4414.774	4415.775	E	14	0.040
4420.315	4421.162	A	12	0.036
4421.854	4422.778	A	13	0.038
4423.778	4424.625	A	12	0.043
4425.010	4426.010	A	14	0.051
4426.934	4427.934	E	14	0.060
4430.935	4431.320	E	6	0.017
4440.009	4440.552	A	8	0.024
4445.595	4446.060	A	7	0.023
4448.000	4448.388	E	6	0.016
4449.008	4449.707	A	10	0.033
4450.250	4450.637	A	6	0.022
4452.577	4453.740	A	16	0.059
4455.680	4457.231	A	21	0.074

Continued, next page.

Table 17 *(continued)*

λ_{start}	λ_{end}	Type	Pixels	W_λ (Å)
4457.930	4458.395	A	7	0.022
4459.792	4460.412	A	9	0.027
4461.343	4462.041	E	10	0.038
4462.429	4463.593	A	16	0.060
4464.446	4464.834	A	6	0.024
4465.144	4465.609	A	7	0.031
4466.230	4468.635	A	32	0.125
4469.256	4469.876	A	9	0.029
4470.264	4471.350	A	15	0.048
4471.505	4472.048	A	8	0.025
4473.134	4473.678	E	8	0.023
4474.375	4474.996	A	9	0.026
4479.024	4480.275	A	17	0.065
4481.449	4481.996	E	8	0.030
4483.951	4484.655	A	10	0.030
4485.280	4485.984	A	10	0.028
4486.531	4487.392	A	12	0.029
4492.162	4492.866	A	10	0.031
4495.290	4497.167	A	25	0.117
4498.026	4499.669	A	22	0.081
4499.903	4502.797	A	38	0.155
4506.550	4506.941	A	6	0.013
4509.365	4509.991	A	9	0.025
4511.980	4514.423	A	32	0.116
4517.103	4517.733	A	9	0.031
4517.970	4518.600	A	9	0.029
4520.413	4521.201	E	11	0.030
4523.329	4523.802	A	7	0.018
4526.008	4527.664	A	22	0.082
4528.767	4529.318	E	8	0.035
4532.471	4533.102	A	9	0.023
4533.811	4534.284	A	7	0.025
4534.835	4535.387	A	8	0.022
4540.037	4540.904	A	12	0.040
4542.244	4542.795	A	8	0.019
4545.086	4548.899	A	49	0.251
4549.773	4550.250	E	7	0.022
4552.792	4554.222	A	19	0.076
4557.161	4557.876	A	10	0.026
4559.544	4561.530	A	26	0.114
4562.006	4564.072	A	27	0.140
4564.310	4564.946	A	9	0.029
4565.343	4565.819	A	7	0.015
4566.534	4566.932	A	6	0.015
4570.586	4570.983	A	6	0.014
4571.619	4572.413	A	11	0.043

Continued, next page.

Table 17 *(continued)*

λ_{start}	λ_{end}	Type	Pixels	W_λ (Å)
4574.558	4575.193	A	9	0.032
4578.292	4579.245	A	13	0.046
4583.058	4583.455	E	6	0.098
4590.736	4591.137	A	6	0.019
4597.305	4598.186	A	12	0.038
4604.113	4605.075	A	13	0.032
4605.235	4607.798	A	33	0.116
4608.279	4608.919	E	9	0.022
4613.085	4614.126	A	14	0.043
4618.772	4619.813	A	14	0.040
4621.896	4623.258	A	18	0.069
4624.540	4625.021	A	7	0.026
4625.946	4626.834	A	12	0.046
4627.561	4628.207	A	9	0.019
4637.331	4638.219	A	12	0.043
4638.865	4640.480	A	21	0.068
4646.213	4647.747	A	20	0.046
4661.312	4662.443	A	15	0.035
4662.604	4663.008	A	6	0.019
4664.300	4664.704	A	6	0.014
4670.525	4671.339	E	11	0.028
4691.607	4692.015	E	6	0.013
4695.515	4696.166	E	9	0.025
4700.182	4700.674	A	7	0.020
4701.988	4702.891	E	12	0.036
4706.666	4707.733	A	14	0.041
4708.964	4710.195	A	16	0.045
4714.135	4716.104	A	25	0.094
4722.014	4723.163	A	15	0.043
4725.543	4726.774	A	16	0.055
4726.938	4730.549	A	45	0.169
4732.191	4732.683	A	7	0.018
4733.422	4734.899	A	19	0.062
4735.228	4737.443	A	28	0.099
4745.147	4745.644	A	7	0.022
4751.770	4752.350	A	8	0.018
4756.075	4757.152	A	14	0.046
4757.483	4759.884	A	30	0.116
4760.960	4761.540	A	8	0.023
4765.431	4767.087	A	21	0.075
4767.583	4768.991	A	18	0.056
4771.392	4771.971	A	8	0.016
4772.468	4773.048	A	8	0.025
4781.146	4781.563	A	6	0.014
4786.321	4786.821	A	7	0.028
4788.824	4790.160	A	17	0.046

Continued, next page.

Table 17 *(continued)*

λ_{start}	λ_{end}	Type	Pixels	W_λ (Å)
4790.410	4790.828	A	6	0.014
4799.424	4799.841	A	6	0.014
4800.509	4800.926	A	6	0.017
4806.852	4809.606	A	34	0.091
4810.524	4811.275	A	10	0.025
4814.947	4815.781	A	11	0.032
4828.384	4829.719	A	17	0.047
4831.054	4832.891	A	23	0.104
4838.307	4840.664	A	29	0.089
4842.685	4844.200	A	19	0.071
4850.094	4860.870	A	129	2.262
4861.039	4867.521	E	78	0.797
4869.037	4869.458	E	6	0.016
4874.593	4875.014	A	6	0.021
4875.043	4875.553	A	7	0.024
4880.310	4882.858	A	31	0.116
4884.557	4887.445	A	35	0.144
4904.349	4904.858	A	7	0.018
4907.322	4908.341	A	13	0.034
4908.681	4910.465	A	22	0.079
4913.523	4914.457	A	12	0.038
4941.698	4942.132	A	6	0.038
4943.782	4944.390	E	8	0.064
4956.459	4957.328	E	11	0.048
4981.553	4982.682	E	14	0.086
4993.969	4994.404	E	6	0.025
4999.933	5000.546	E	8	0.053
5000.983	5001.509	E	7	0.028
5012.197	5012.722	E	7	0.044
5012.985	5013.423	E	6	0.025
5013.949	5014.562	E	8	0.057
5016.665	5017.103	A	6	0.025
5017.278	5017.803	A	7	0.034
5018.679	5019.380	E	9	0.034
5019.906	5020.694	E	10	0.047
5040.755	5041.981	E	15	0.117
5050.301	5052.511	E	26	0.164
5062.941	5063.383	A	6	0.021
5067.095	5067.714	A	8	0.028
5071.161	5071.603	E	6	0.034
5079.205	5080.088	E	11	0.081
5086.718	5087.336	E	8	0.034
5092.010	5092.456	A	6	0.021
5094.059	5094.505	A	6	0.016
5098.781	5099.226	E	6	0.025
5100.028	5100.652	E	8	0.029

Continued, next page.

Table 17 *(continued)*

λ_{start}	λ_{end}	Type	Pixels	W_λ (Å)
5101.632	5102.344	E	9	0.032
5106.888	5107.422	E	7	0.043
5107.601	5108.491	E	11	0.051
5110.273	5111.075	E	10	0.067
5113.391	5113.925	E	7	0.028
5123.012	5124.437	E	17	0.116
5131.831	5132.544	E	9	0.042
5132.722	5133.524	E	10	0.054
5136.196	5137.087	E	11	0.053
5139.136	5139.760	E	8	0.044
5143.062	5143.602	E	7	0.043
5144.052	5145.311	A	15	0.063
5151.247	5151.697	E	6	0.025
5153.046	5154.305	E	15	0.077
5159.521	5160.061	A	7	0.033
5163.119	5165.097	A	23	0.172
5165.277	5165.997	A	9	0.041
5166.716	5167.616	E	11	0.067
5168.875	5170.044	E	14	0.071
5171.933	5172.382	E	6	0.018
5173.012	5173.461	E	6	0.029
5181.017	5182.006	A	12	0.060
5182.186	5182.635	A	6	0.042
5191.799	5192.253	E	6	0.033
5192.616	5193.251	E	8	0.033
5205.051	5206.503	E	17	0.093
5207.864	5208.590	E	9	0.039
5208.863	5209.317	E	6	0.030
5210.224	5211.223	E	12	0.053
5215.670	5217.032	E	16	0.073
5217.395	5217.849	A	6	0.027
5220.481	5220.935	A	6	0.024
5222.750	5223.385	A	8	0.030
5224.565	5225.019	A	6	0.016
5225.745	5228.105	E	27	0.173
5249.887	5250.346	E	6	0.019
5253.279	5253.921	A	8	0.026
5256.396	5256.947	E	7	0.024
5268.774	5270.424	E	19	0.166
5280.784	5281.701	A	11	0.050
5314.611	5315.628	A	12	0.044
5320.435	5321.082	A	8	0.024
5322.191	5322.654	A	6	0.015
5323.023	5323.578	A	7	0.109
5327.369	5329.033	E	19	0.173
5337.085	5337.646	E	7	0.023

Continued, next page.

Table 17 *(continued)*

λ_{start}	λ_{end}	Type	Pixels	W_λ (Å)
5345.303	5346.330	E	12	0.047
5362.205	5362.672	E	6	0.020
5370.609	5372.104	E	17	0.086
5373.785	5374.251	A	6	0.017
5380.228	5380.695	E	6	0.023
5383.123	5383.590	A	6	0.018
5386.017	5386.484	A	6	0.020
5396.293	5397.801	E	17	0.114
5398.367	5398.838	A	6	0.026
5403.269	5403.740	E	6	0.017
5404.872	5406.568	E	19	0.095
5429.003	5430.323	E	15	0.062
5433.811	5435.319	E	17	0.056
5441.037	5441.798	A	9	0.029
5443.131	5444.083	A	11	0.041
5444.845	5445.607	A	9	0.046
5446.274	5447.607	E	15	0.068
5454.653	5456.367	E	19	0.109
5464.270	5464.746	A	6	0.019
5475.982	5477.220	E	14	0.058
5477.410	5477.886	E	6	0.019
5483.123	5483.885	A	9	0.024
5497.448	5498.313	E	10	0.038
5501.870	5502.447	E	7	0.024
5504.466	5504.947	A	6	0.017
5507.062	5507.639	E	7	0.019
5509.081	5509.562	E	6	0.020
5513.119	5513.600	A	6	0.015
5525.714	5526.483	E	9	0.028
5531.098	5531.771	A	8	0.022
5533.886	5535.616	E	19	0.068
5545.256	5545.741	E	6	0.018
5597.513	5598.582	E	12	0.064
5629.268	5629.856	E	7	0.021
5657.017	5658.800	E	19	0.080
5667.916	5668.708	E	9	0.034
5687.731	5688.227	E	6	0.022
5698.333	5698.828	E	6	0.017
5704.772	5705.268	A	6	0.017
5708.736	5709.330	E	7	0.020
5755.131	5755.832	A	8	0.025
5813.196	5813.904	E	8	0.022
5852.859	5853.371	E	6	0.020
5885.562	5888.934	A	34	0.918
5889.139	5889.751	E	7	0.164
5890.467	5891.387	E	10	0.214

Continued, next page.

Table 17 *(continued)*

λ_{start}	λ_{end}	Type	Pixels	W_λ (Å)
5891.898	5894.861	A	30	0.507
5895.066	5895.679	E	7	0.177
5896.395	5897.927	E	16	0.219
5955.132	5955.758	E	7	0.021
5978.284	5978.909	E	7	0.018
5990.485	5991.006	E	6	0.018
5991.424	5992.049	E	7	0.024
6019.894	6021.053	A	12	0.038
6022.213	6022.846	A	7	0.025
6094.379	6094.913	A	6	0.017
6103.119	6104.184	A	11	0.047
6136.262	6137.541	E	13	0.061
6140.951	6141.803	E	9	0.031
6148.198	6150.435	E	22	0.109
6160.832	6161.693	E	9	0.034
6171.603	6172.142	A	6	0.017
6190.560	6192.499	E	19	0.099
6222.328	6223.090	E	8	0.026
6229.953	6231.586	E	16	0.055
6238.558	6240.192	E	16	0.077
6242.698	6243.460	E	8	0.033
6244.876	6245.639	E	8	0.027
6251.630	6252.175	E	6	0.018
6257.730	6259.038	E	13	0.058
6260.780	6261.652	E	9	0.032
6268.187	6269.276	E	11	0.039
6335.158	6336.149	E	10	0.030
6345.956	6348.050	E	20	0.082
6356.976	6357.527	E	6	0.016
6357.967	6359.069	E	11	0.047
6370.221	6370.890	E	7	0.026
6384.260	6384.929	E	7	0.028
6387.603	6388.606	E	10	0.032
6399.637	6400.862	E	12	0.058
6430.055	6432.729	E	25	0.102
6432.952	6433.509	E	6	0.022
6439.229	6439.905	A	7	0.028
6457.043	6457.720	E	7	0.023
6472.040	6472.942	A	9	0.029
6481.286	6482.188	E	9	0.025
6494.366	6495.493	E	11	0.038
6496.621	6497.410	E	8	0.025
6498.650	6499.214	E	6	0.022
6499.552	6500.341	A	8	0.030
6514.891	6517.516	E	24	0.125
6526.301	6527.328	E	10	0.035

Continued, next page.

Table 17 *(continued)*

λ_{start}	λ_{end}	Type	Pixels	W_λ (Å)
6532.577	6533.147	E	6	0.023
6537.483	6538.167	E	7	0.023
6543.074	6543.645	E	6	0.024
6546.041	6560.988	A	132	7.303
6561.331	6571.486	E	90	2.460
6572.170	6573.311	E	11	0.072
6573.767	6574.680	E	9	0.040
6578.788	6579.358	E	6	0.020
6580.613	6581.526	E	9	0.034
6582.896	6583.580	E	7	0.047
6592.035	6592.612	E	6	0.017
6593.189	6594.228	E	10	0.036
6598.613	6599.421	E	8	0.037
6605.769	6606.923	E	11	0.038
6609.000	6609.577	E	6	0.017
6624.464	6625.272	E	8	0.031
6642.930	6644.083	E	11	0.036
6651.008	6652.162	E	11	0.038
6699.041	6699.625	A	6	0.019
6706.630	6709.316	A	24	0.241
6750.509	6751.336	A	8	0.026
6784.650	6785.241	E	6	0.017
8039.933	8042.156	E	17	0.136
8043.267	8045.073	E	14	0.102
8046.879	8048.129	E	10	0.071
8050.769	8052.158	E	11	0.065
8053.270	8054.242	E	8	0.035
8062.994	8064.383	E	11	0.046
8067.300	8068.550	E	10	0.055
8069.106	8071.051	E	15	0.070
8073.968	8075.913	E	15	0.111
8083.137	8084.248	A	9	0.042
8089.110	8090.917	E	14	0.071
8092.444	8093.695	E	10	0.040
8094.111	8095.501	A	11	0.081
8106.614	8108.281	A	13	0.063
8116.061	8117.033	E	8	0.028
8117.450	8118.839	A	11	0.060
8396.415	8397.716	E	10	0.068
8401.184	8402.340	E	9	0.054
8404.508	8405.230	E	6	0.024
8408.699	8410.000	A	10	0.035
8411.301	8414.336	E	22	0.203
8425.175	8427.343	E	16	0.161
8428.065	8429.511	A	11	0.050
8430.667	8431.679	A	8	0.043

Continued, next page.

Table 17 *(continued)*

λ_{start}	λ_{end}	Type	Pixels	W_λ (Å)
8433.847	8436.304	E	18	0.277
8451.334	8452.057	A	6	0.021
8456.103	8457.403	E	10	0.050
8460.727	8462.605	A	14	0.094
8464.340	8466.941	E	19	0.131
8467.230	8469.254	E	15	0.123
8472.867	8474.890	A	15	0.076
8476.335	8477.491	E	9	0.041
8487.319	8488.909	E	12	0.061
8494.400	8495.412	A	8	0.044
8496.135	8499.604	E	25	1.557
8529.953	8530.691	E	6	0.022
8539.850	8551.371	E	79	2.694
8557.280	8558.609	A	10	0.049
8576.334	8577.221	A	7	0.028
8578.846	8579.880	A	8	0.033
8581.652	8582.687	E	8	0.041
8586.675	8587.561	A	7	0.029
8590.663	8591.845	E	9	0.044
8596.719	8597.605	E	7	0.029
8598.049	8598.787	E	6	0.022
8602.332	8604.104	E	13	0.063
8604.548	8605.435	E	7	0.028
8611.048	8612.377	E	10	0.047
8617.694	8621.092	A	24	0.132
8623.455	8624.785	A	10	0.041
8629.808	8630.546	A	6	0.027
8660.294	8676.044	E	106	2.849
8678.444	8684.444	E	41	0.362
8687.294	8690.295	E	21	0.241
8691.345	8692.995	E	12	0.095
8693.295	8694.795	E	11	0.047
8701.245	8704.245	E	21	0.118
8709.196	8710.396	E	9	0.039
8712.046	8714.146	E	15	0.085
8729.147	8731.098	E	14	0.067
8733.947	8735.748	E	13	0.089
8738.448	8739.498	A	8	0.030
8740.698	8742.348	E	12	0.049
8750.299	8752.698	E	17	0.106
8756.449	8757.649	E	9	0.042
8792.646	8793.711	E	8	0.041
8795.995	8797.061	E	8	0.039
8803.910	8807.868	E	27	0.199
8818.677	8819.590	E	7	0.034
8822.787	8825.527	E	19	0.190

Continued, next page.

Table 17 *(continued)*

λ_{start}	λ_{end}	Type	Pixels	W_λ (Å)
8826.745	8827.658	E	7	0.068
8835.879	8839.837	E	27	0.213
8841.512	8842.729	E	9	0.033
8858.865	8860.540	E	12	0.069
8861.605	8862.976	E	10	0.043
8866.325	8868.761	E	17	0.102
8878.198	8878.960	E	6	0.025
8883.223	8884.287	E	8	0.033
8890.376	8892.203	E	13	0.072
8902.858	8903.925	E	8	0.035

Table 18. Complete list of residual features for Z CMa.

λ_{start}	λ_{end}	Type	Pixels	W_λ (Å)
3991.652	3992.420	E	12	0.040
3997.729	3998.358	E	10	0.038
3998.498	3999.126	E	10	0.039
4000.523	4000.873	E	6	0.012
4001.851	4002.549	E	11	0.052
4002.759	4003.248	E	8	0.040
4005.273	4005.972	E	11	0.027
4007.858	4008.417	A	9	0.035
4009.813	4010.652	A	13	0.041
4010.792	4011.350	A	9	0.026
4011.490	4011.909	A	7	0.025
4012.189	4012.677	E	8	0.034
4013.027	4013.446	E	7	0.026
4015.681	4016.170	E	8	0.029
4020.990	4021.688	A	11	0.031
4024.483	4026.578	E	31	0.125
4027.765	4028.115	E	6	0.017
4030.376	4031.080	E	11	0.046
4034.243	4034.665	E	7	0.020
4035.298	4035.861	E	9	0.028
4036.775	4037.126	E	6	0.013
4039.938	4040.571	A	10	0.031
4041.555	4042.188	A	10	0.019
4043.383	4044.649	A	19	0.079
4045.282	4047.250	E	29	0.120
4055.688	4056.250	A	9	0.031
4057.586	4057.937	A	6	0.020
4061.731	4062.369	A	10	0.022
4062.723	4065.273	E	37	0.204
4065.486	4068.815	E	48	0.184
4071.082	4072.144	E	16	0.060
4075.828	4076.395	A	9	0.028
4076.820	4078.024	E	18	0.069
4078.378	4078.803	E	7	0.020
4079.016	4079.653	A	10	0.028
4083.903	4084.399	A	8	0.025
4084.966	4085.816	A	13	0.037
4091.745	4092.458	A	11	0.030
4093.029	4100.090	A	100	1.611
4100.304	4108.292	E	113	1.478
4109.719	4110.147	E	7	0.019
4110.504	4112.430	E	28	0.078
4113.500	4113.856	E	6	0.017
4117.280	4117.850	A	9	0.028
4120.011	4120.730	A	11	0.027
4121.521	4121.881	E	6	0.012

Continued, next page.

Table 18 *(continued)*

λ_{start}	λ_{end}	Type	Pixels	W_λ (Å)
4123.031	4124.254	E	18	0.050
4127.633	4128.855	E	18	0.045
4131.373	4132.523	E	17	0.062
4133.889	4134.608	A	11	0.031
4136.190	4136.550	A	6	0.013
4137.916	4138.994	E	16	0.041
4139.138	4139.929	E	12	0.033
4141.655	4143.453	A	26	0.086
4144.244	4144.891	E	10	0.025
4150.688	4151.050	A	6	0.012
4153.367	4154.598	A	18	0.054
4154.743	4155.178	A	7	0.012
4161.549	4162.925	E	20	0.059
4163.287	4164.808	E	22	0.061
4172.411	4173.786	E	20	0.098
4173.931	4174.366	E	7	0.017
4175.886	4176.321	A	7	0.025
4177.407	4181.027	E	51	0.280
4185.787	4187.318	A	22	0.067
4189.725	4190.090	A	6	0.010
4195.195	4195.560	A	6	0.013
4195.706	4196.070	A	6	0.016
4197.675	4198.842	A	17	0.050
4199.572	4200.083	A	8	0.017
4200.228	4200.958	A	11	0.028
4201.687	4202.271	E	9	0.024
4203.583	4204.021	A	7	0.017
4204.167	4204.604	A	7	0.015
4209.710	4210.221	A	8	0.016
4210.439	4210.877	A	7	0.013
4213.325	4214.354	A	15	0.065
4215.089	4216.926	E	26	0.099
4219.204	4219.792	A	9	0.019
4221.556	4225.525	A	55	0.175
4226.407	4228.612	E	31	0.184
4230.449	4231.699	A	18	0.041
4232.140	4235.080	E	41	0.300
4240.847	4243.957	E	43	0.192
4244.697	4246.252	A	22	0.112
4246.475	4247.067	E	9	0.048
4248.399	4249.955	A	22	0.068
4250.547	4251.953	E	20	0.057
4252.323	4253.212	A	13	0.039
4253.878	4254.544	E	10	0.054
4255.952	4256.322	A	6	0.015
4258.173	4258.543	E	6	0.016

Continued, next page.

Table 18 *(continued)*

λ_{start}	λ_{end}	Type	Pixels	W_λ (Å)
4259.876	4260.320	A	7	0.016
4261.356	4261.949	E	9	0.017
4269.501	4271.204	A	24	0.057
4271.574	4272.759	E	17	0.055
4273.116	4273.937	A	12	0.047
4274.310	4274.981	E	10	0.055
4279.010	4282.368	A	46	0.276
4282.890	4289.754	A	93	0.508
4290.649	4299.603	A	121	1.107
4300.125	4302.811	A	37	0.174
4303.109	4304.825	A	24	0.172
4304.825	4307.382	A	35	0.260
4307.608	4307.984	E	6	0.025
4308.285	4313.624	A	72	0.586
4314.676	4316.030	E	19	0.074
4318.963	4320.091	A	16	0.034
4321.971	4324.903	A	40	0.260
4325.354	4326.031	E	10	0.033
4326.783	4327.836	A	15	0.055
4327.805	4339.016	A	149	3.348
4339.243	4346.514	E	97	1.170
4350.832	4353.181	E	32	0.172
4356.437	4356.816	E	6	0.014
4357.649	4358.331	E	10	0.022
4358.482	4358.937	E	7	0.012
4359.467	4359.846	A	6	0.013
4372.651	4374.103	A	20	0.064
4374.942	4376.241	E	18	0.054
4381.280	4382.960	A	23	0.098
4383.189	4386.167	E	40	0.232
4387.695	4391.208	A	47	0.164
4392.124	4394.491	A	32	0.197
4394.644	4396.629	E	27	0.153
4397.928	4399.226	A	18	0.048
4400.523	4401.975	E	20	0.047
4404.291	4405.061	E	11	0.045
4410.216	4419.451	E	121	0.566
4428.685	4430.301	A	22	0.052
4432.918	4435.918	A	40	0.122
4437.766	4438.458	E	10	0.024
4440.458	4443.250	A	37	0.178
4443.483	4445.190	E	23	0.097
4451.163	4451.938	E	11	0.032
4454.343	4454.809	A	7	0.014
4458.377	4458.765	A	6	0.012
4463.187	4464.117	A	13	0.040

Continued, next page.

Table 18 *(continued)*

λ_{start}	λ_{end}	Type	Pixels	W_λ (Å)
4465.591	4467.918	A	31	0.202
4468.151	4468.927	E	11	0.044
4472.417	4474.822	E	32	0.173
4474.941	4478.147	E	42	0.139
4481.822	4482.682	E	12	0.049
4484.559	4485.340	A	11	0.021
4491.127	4491.909	E	11	0.033
4493.629	4494.255	A	9	0.019
4494.880	4500.823	A	77	0.463
4501.605	4502.153	A	8	0.019
4505.358	4506.609	A	17	0.040
4507.861	4508.643	E	11	0.048
4510.465	4514.169	A	48	0.121
4514.878	4515.745	E	12	0.041
4516.927	4517.952	A	14	0.042
4518.267	4519.055	A	11	0.023
4519.606	4520.552	E	13	0.053
4521.025	4523.311	E	30	0.105
4525.044	4527.802	A	36	0.106
4531.034	4533.398	A	31	0.165
4533.634	4534.186	E	8	0.035
4534.896	4535.368	E	7	0.017
4537.575	4538.441	E	12	0.028
4542.067	4542.934	E	12	0.032
4545.625	4548.643	A	39	0.220
4548.961	4551.264	E	30	0.229
4552.376	4553.647	A	17	0.043
4554.839	4559.208	E	56	0.300
4560.955	4563.259	A	30	0.154
4563.497	4564.053	E	8	0.022
4564.689	4565.086	E	6	0.014
4569.535	4570.806	A	17	0.062
4571.600	4572.314	E	10	0.035
4572.553	4573.347	E	11	0.025
4576.048	4576.842	E	11	0.028
4577.875	4582.562	A	60	0.214
4582.800	4584.865	E	27	0.190
4589.597	4589.998	E	6	0.020
4607.379	4608.180	E	11	0.024
4608.500	4611.784	E	42	0.148
4616.831	4618.112	E	17	0.055
4618.513	4622.357	E	49	0.155
4624.797	4625.847	A	14	0.037
4626.654	4627.866	A	16	0.051
4628.834	4630.853	E	26	0.104
4633.760	4634.486	E	10	0.023

Continued, next page.

Table 18 *(continued)*

λ_{start}	λ_{end}	Type	Pixels	W_λ (Å)
4636.585	4637.635	A	14	0.033
4638.039	4639.089	A	14	0.034
4644.821	4645.628	A	11	0.026
4646.032	4648.778	A	35	0.101
4650.715	4651.604	A	12	0.028
4652.895	4653.703	A	11	0.024
4653.864	4656.044	A	28	0.080
4656.206	4656.609	A	6	0.012
4661.292	4663.714	A	31	0.086
4667.983	4669.855	A	24	0.084
4673.600	4674.169	A	8	0.016
4679.053	4680.274	A	16	0.042
4680.519	4681.902	A	18	0.055
4694.844	4695.658	E	11	0.031
4696.228	4696.960	E	10	0.024
4702.133	4702.872	A	10	0.021
4703.693	4704.103	A	6	0.012
4704.678	4709.684	A	62	0.223
4713.541	4716.742	A	40	0.103
4727.000	4727.411	A	6	0.013
4727.821	4729.791	A	25	0.076
4732.910	4733.484	A	8	0.017
4734.469	4735.700	A	16	0.038
4735.864	4737.423	A	20	0.058
4737.588	4738.408	A	11	0.022
4753.159	4753.738	A	8	0.017
4754.980	4759.202	A	52	0.145
4761.354	4763.673	A	29	0.081
4764.500	4765.908	A	18	0.044
4766.156	4767.895	A	22	0.061
4771.951	4772.365	A	6	0.011
4778.657	4779.402	A	10	0.022
4782.045	4784.883	A	35	0.114
4785.133	4790.725	A	68	0.245
4791.392	4791.976	A	8	0.017
4797.234	4798.319	A	14	0.035
4798.736	4800.656	A	24	0.059
4812.590	4814.593	E	25	0.087
4825.275	4825.776	E	7	0.018
4828.029	4828.780	A	10	0.023
4830.032	4830.700	A	9	0.020
4831.284	4832.453	A	15	0.032
4835.846	4836.435	E	8	0.020
4846.706	4860.092	A	160	5.522
4860.260	4868.848	E	103	2.212
4880.630	4886.830	A	74	0.284

Continued, next page.

Table 18 *(continued)*

λ_{start}	λ_{end}	Type	Pixels	W_λ (Å)
4887.085	4888.699	A	20	0.069
4889.293	4893.031	A	45	0.154
4898.552	4899.741	A	15	0.037
4900.506	4901.440	A	12	0.030
4901.865	4904.328	A	30	0.096
4908.065	4911.803	A	45	0.172
4912.397	4913.502	A	14	0.037
4914.351	4914.776	A	6	0.013
4940.668	4941.103	A	6	0.021
4945.530	4945.965	A	6	0.034
4946.312	4946.746	A	6	0.030
4950.740	4952.303	A	19	0.070
4952.477	4952.998	A	7	0.029
4953.171	4953.692	A	7	0.030
4956.731	4957.166	A	6	0.017
4967.324	4968.019	A	9	0.027
4968.800	4969.495	A	9	0.035
4969.669	4970.103	A	6	0.018
4981.390	4982.519	E	14	0.041
4999.450	4999.885	E	6	0.026
5010.369	5010.895	A	7	0.026
5014.311	5017.026	A	32	0.191
5017.289	5022.458	E	60	0.836
5022.633	5023.246	E	8	0.031
5025.086	5025.611	E	7	0.025
5079.040	5079.570	E	7	0.022
5091.488	5091.933	A	6	0.018
5103.870	5104.672	A	10	0.034
5105.474	5106.632	A	14	0.050
5108.325	5109.750	A	17	0.066
5125.072	5125.518	A	6	0.020
5125.696	5126.141	A	6	0.019
5151.439	5151.889	E	6	0.014
5158.813	5167.357	A	96	1.058
5167.897	5170.686	E	32	0.425
5171.045	5174.013	E	34	0.188
5176.711	5177.161	A	6	0.016
5179.859	5182.197	A	27	0.121
5182.647	5184.355	E	20	0.129
5196.894	5198.619	E	20	0.146
5203.429	5203.883	A	6	0.020
5205.607	5206.062	E	6	0.020
5208.058	5208.602	E	7	0.027
5210.055	5210.781	E	9	0.028
5219.585	5220.220	E	8	0.025
5226.029	5228.389	E	27	0.169

Continued, next page.

Table 18 *(continued)*

λ_{start}	λ_{end}	Type	Pixels	W_λ (Å)
5233.472	5235.377	E	22	0.155
5235.780	5236.514	E	9	0.028
5236.789	5237.339	E	7	0.025
5237.706	5238.531	E	10	0.036
5239.906	5240.364	E	6	0.019
5246.507	5247.148	E	8	0.022
5255.400	5255.950	E	7	0.018
5267.319	5268.235	A	11	0.055
5268.969	5270.895	E	22	0.131
5271.903	5272.636	A	9	0.023
5273.370	5274.653	A	15	0.046
5275.387	5276.670	E	15	0.098
5281.254	5281.713	A	6	0.016
5283.546	5285.472	E	22	0.108
5296.781	5297.243	A	6	0.019
5299.092	5299.924	A	10	0.037
5300.664	5301.218	A	7	0.020
5301.958	5302.697	A	9	0.032
5302.975	5303.529	A	7	0.020
5315.362	5318.505	E	35	0.335
5321.094	5321.649	A	7	0.018
5322.758	5323.405	A	8	0.023
5325.994	5326.733	A	9	0.036
5327.473	5328.767	E	15	0.074
5335.977	5338.405	E	27	0.114
5340.366	5340.926	E	7	0.022
5361.937	5363.525	E	18	0.110
5369.407	5370.248	A	10	0.037
5370.995	5371.929	E	11	0.042
5375.664	5376.131	E	6	0.015
5396.400	5397.625	E	14	0.058
5399.040	5399.511	A	6	0.015
5403.847	5404.506	A	8	0.023
5405.261	5406.392	E	13	0.052
5421.380	5421.946	A	7	0.022
5422.134	5423.737	A	18	0.072
5424.774	5425.528	E	9	0.022
5429.205	5430.053	E	10	0.036
5444.287	5446.001	A	19	0.073
5446.572	5447.905	E	15	0.049
5448.762	5449.333	E	7	0.020
5450.952	5451.904	E	11	0.029
5454.951	5456.951	E	22	0.073
5461.711	5462.283	A	7	0.021
5462.568	5463.235	A	8	0.019
5475.042	5475.708	A	8	0.023

Continued, next page.

Table 18 *(continued)*

λ_{start}	λ_{end}	Type	Pixels	W_λ (Å)
5514.574	5515.055	E	6	0.020
5526.014	5527.168	E	13	0.052
5534.283	5535.725	E	16	0.093
5579.459	5580.916	A	16	0.049
5581.402	5581.984	A	7	0.018
5588.687	5589.464	A	9	0.023
5601.131	5601.916	A	9	0.030
5602.209	5602.896	A	8	0.026
5616.824	5617.314	A	6	0.015
5633.890	5634.675	A	9	0.024
5657.625	5658.814	E	13	0.045
5710.299	5711.000	A	8	0.028
5780.035	5780.743	A	8	0.027
5781.451	5781.957	E	6	0.017
5782.665	5783.170	E	6	0.019
5804.005	5810.276	A	63	0.217
5823.424	5823.930	A	6	0.015
5824.132	5825.144	A	11	0.037
5862.684	5863.399	E	8	0.020
5865.647	5867.385	E	18	0.053
5878.217	5889.356	A	110	3.342
5891.093	5895.283	A	42	1.523
5896.203	5898.553	E	24	0.335
5990.812	5991.958	E	12	0.057
6136.701	6137.980	E	13	0.051
6139.259	6140.645	A	14	0.066
6147.039	6150.982	E	38	0.221
6158.368	6160.307	E	19	0.066
6160.954	6162.354	E	14	0.053
6190.574	6192.405	E	18	0.096
6202.638	6203.392	A	8	0.022
6215.563	6216.317	E	8	0.021
6220.599	6221.362	A	8	0.024
6233.998	6234.542	A	6	0.016
6237.810	6240.642	E	27	0.135
6246.742	6249.683	E	28	0.129
6251.971	6252.733	E	8	0.022
6257.090	6259.269	E	21	0.079
6261.121	6262.101	E	10	0.031
6267.875	6268.746	E	9	0.025
6268.964	6269.726	E	8	0.023
6341.453	6342.996	A	15	0.050
6357.761	6359.745	E	19	0.057
6361.508	6363.932	E	23	0.098
6365.779	6367.339	A	15	0.046
6367.562	6368.342	A	8	0.029

Continued, next page.

Table 18 *(continued)*

λ_{start}	λ_{end}	Type	Pixels	W_λ (Å)
6392.743	6393.635	E	9	0.029
6399.317	6401.211	E	18	0.061
6416.476	6417.812	E	13	0.052
6429.958	6434.191	E	39	0.262
6440.258	6441.048	A	8	0.024
6449.279	6450.631	E	13	0.039
6455.480	6458.073	E	24	0.188
6467.770	6469.800	A	19	0.061
6470.025	6471.378	A	13	0.036
6472.619	6473.746	A	11	0.034
6481.752	6482.767	E	10	0.032
6514.907	6517.531	E	24	0.246
6538.411	6560.432	A	194	7.563
6560.774	6582.111	E	188	15.081
6592.858	6593.435	E	6	0.017
6614.093	6615.016	E	9	0.030
6624.364	6626.095	E	16	0.056
6644.906	6646.060	A	11	0.037
6705.828	6709.681	A	34	0.195
6714.701	6716.687	E	18	0.075
6718.204	6718.905	E	7	0.021
6753.242	6753.950	E	7	0.021
6783.720	6784.429	E	7	0.021
8046.438	8048.661	E	17	0.085
8068.247	8069.637	E	11	0.057
8070.331	8071.304	E	8	0.034
8075.193	8075.888	E	6	0.026
8090.891	8093.252	E	18	0.083
8129.510	8130.204	A	6	0.042
8393.354	8395.521	A	16	0.106
8410.841	8414.310	E	25	0.242
8425.003	8427.460	E	18	0.128
8433.241	8437.576	E	31	0.322
8437.865	8440.322	E	18	0.088
8442.635	8448.994	E	45	1.015
8464.457	8470.383	E	42	0.340
8489.604	8495.239	A	40	0.517
8495.528	8499.431	E	28	3.393
8532.143	8538.198	A	42	0.316
8538.789	8550.312	E	79	5.899
8550.606	8551.346	E	6	0.021
8579.115	8580.148	A	8	0.031
8596.987	8599.499	E	18	0.150
8610.873	8612.940	E	15	0.068
8617.815	8621.360	A	25	0.121
8623.575	8624.462	A	7	0.027

Continued, next page.

Table 18 *(continued)*

λ_{start}	λ_{end}	Type	Pixels	W_λ (Å)
8654.867	8659.066	A	29	0.451
8659.517	8668.218	E	59	4.887
8673.918	8676.018	E	15	0.092
8681.418	8683.969	E	18	0.104
8687.269	8690.268	E	21	0.166
8735.120	8736.170	E	8	0.029
8746.370	8752.971	E	45	0.379
8804.493	8808.755	E	29	0.259
8822.455	8825.804	E	23	0.185
8837.373	8839.962	E	18	0.111
8859.294	8864.470	E	35	0.347
8866.601	8868.123	E	11	0.049
8891.413	8892.326	E	7	0.028

Table 19. Complete list of residual features for FU Ori.

λ_{start}	λ_{end}	Type	Pixels	W_λ (Å)
3990.170	3990.589	A	7	0.054
3991.078	3991.777	A	11	0.057
3991.986	3992.405	A	7	0.026
3992.615	3993.243	A	10	0.030
3993.942	3994.431	A	8	0.029
3994.850	3995.828	A	15	0.048
3996.876	3997.225	A	6	0.013
3997.993	3998.343	E	6	0.018
3998.762	3999.251	A	8	0.024
3999.460	3999.949	E	8	0.060
4000.298	4000.997	A	11	0.044
4001.975	4003.163	E	18	0.130
4003.372	4004.140	E	12	0.044
4004.979	4005.677	A	11	0.090
4006.515	4007.284	A	12	0.053
4008.471	4008.960	A	8	0.022
4009.169	4009.798	A	10	0.046
4010.636	4011.824	A	18	0.100
4011.964	4012.662	A	11	0.087
4012.802	4013.291	E	8	0.045
4013.710	4014.408	A	11	0.047
4015.386	4015.875	E	8	0.022
4016.085	4016.434	E	6	0.027
4016.644	4017.691	A	16	0.065
4019.927	4020.695	A	12	0.073
4021.463	4022.232	A	12	0.071
4023.000	4023.699	A	11	0.065
4024.397	4025.096	A	11	0.060
4025.655	4026.144	E	8	0.034
4026.702	4027.261	A	9	0.032
4027.680	4028.658	A	15	0.090
4029.357	4029.776	A	7	0.050
4029.798	4030.853	A	16	0.088
4031.556	4033.665	A	31	0.150
4034.017	4034.720	A	11	0.072
4034.860	4035.423	E	9	0.036
4035.985	4036.759	E	12	0.050
4037.181	4038.446	E	19	0.065
4040.134	4041.399	A	19	0.085
4041.961	4042.313	E	6	0.027
4043.157	4043.579	E	7	0.014
4043.719	4046.039	A	34	0.250
4046.461	4046.883	E	7	0.029
4047.586	4048.360	E	12	0.057
4049.274	4049.906	E	10	0.041
4051.031	4051.945	E	14	0.077

Continued, next page.

Table 19 *(continued)*

λ_{start}	λ_{end}	Type	Pixels	W_λ (Å)
4052.859	4053.422	E	9	0.043
4054.266	4054.688	E	7	0.020
4060.087	4060.795	E	11	0.039
4061.008	4061.999	E	15	0.061
4062.141	4062.636	A	8	0.026
4063.912	4066.249	E	34	0.178
4066.532	4067.170	A	10	0.035
4067.524	4070.216	E	39	0.182
4070.358	4070.783	A	7	0.023
4070.925	4072.199	A	19	0.122
4072.412	4073.475	E	16	0.043
4073.900	4074.466	E	9	0.025
4074.821	4075.316	A	8	0.022
4075.741	4078.292	A	37	0.259
4079.000	4079.991	A	15	0.062
4080.842	4081.833	E	15	0.057
4083.321	4083.746	A	7	0.022
4087.500	4088.350	E	13	0.052
4091.016	4091.872	E	13	0.042
4092.300	4092.656	A	6	0.016
4093.013	4094.582	E	23	0.132
4096.508	4097.935	E	21	0.115
4098.077	4101.500	A	49	1.005
4101.786	4109.204	E	105	1.120
4109.917	4111.130	E	18	0.070
4111.344	4111.915	E	9	0.030
4113.198	4114.268	E	16	0.081
4115.410	4116.052	E	10	0.030
4117.549	4117.906	E	6	0.016
4118.405	4118.905	A	8	0.035
4122.656	4123.015	A	6	0.012
4124.022	4124.957	E	14	0.041
4125.820	4126.395	A	9	0.041
4126.754	4127.258	E	8	0.025
4128.121	4129.127	E	15	0.078
4131.141	4131.788	E	10	0.048
4132.003	4132.507	A	8	0.029
4132.723	4133.226	E	8	0.026
4133.441	4135.096	A	24	0.128
4135.311	4136.246	E	14	0.036
4136.677	4137.612	A	14	0.068
4138.691	4139.410	E	11	0.026
4139.698	4140.489	A	12	0.051
4141.352	4144.371	A	43	0.289
4144.587	4144.946	E	6	0.017
4145.378	4146.241	A	13	0.043

Continued, next page.

Table 19 *(continued)*

λ_{start}	λ_{end}	Type	Pixels	W_λ (Å)
4147.248	4148.039	A	12	0.054
4148.183	4148.614	E	7	0.040
4148.901	4149.764	A	13	0.105
4150.745	4151.686	E	14	0.079
4151.976	4152.338	A	6	0.018
4152.627	4153.496	E	13	0.073
4153.930	4154.582	A	10	0.045
4154.872	4155.886	E	15	0.091
4156.030	4156.754	A	11	0.063
4156.972	4157.841	E	13	0.058
4158.203	4158.565	E	6	0.013
4158.854	4159.216	A	6	0.018
4159.579	4160.158	E	9	0.033
4161.171	4161.678	A	8	0.026
4161.896	4163.054	E	17	0.098
4163.271	4164.140	A	13	0.081
4164.864	4165.806	A	14	0.063
4166.095	4166.530	E	7	0.022
4166.747	4167.978	A	18	0.096
4168.412	4170.150	A	25	0.110
4170.584	4170.947	A	6	0.014
4171.381	4172.540	A	17	0.099
4172.902	4174.060	A	17	0.071
4174.639	4178.042	A	48	0.339
4178.767	4179.491	A	11	0.056
4184.822	4186.208	E	20	0.098
4186.500	4187.594	A	16	0.063
4188.177	4188.907	E	11	0.046
4190.438	4190.949	E	8	0.025
4191.241	4191.824	A	9	0.030
4192.043	4193.283	E	18	0.076
4194.231	4194.596	E	6	0.014
4194.815	4195.835	A	15	0.051
4196.273	4196.857	A	9	0.025
4197.076	4197.659	E	9	0.037
4197.878	4198.972	A	16	0.078
4200.212	4201.160	A	14	0.071
4201.744	4202.473	A	11	0.048
4202.765	4203.203	E	7	0.026
4203.567	4203.932	A	6	0.018
4204.953	4205.391	A	7	0.023
4205.536	4206.338	E	12	0.069
4206.558	4207.068	A	8	0.028
4207.360	4208.308	E	14	0.076
4208.527	4209.183	A	10	0.039
4209.913	4210.788	A	13	0.055

Continued, next page.

Table 19 *(continued)*

λ_{start}	λ_{end}	Type	Pixels	W_λ (Å)
4211.838	4212.426	A	9	0.033
4212.941	4216.174	A	45	0.521
4216.395	4216.910	E	8	0.035
4217.204	4218.232	A	15	0.074
4218.600	4220.805	A	31	0.142
4221.025	4221.467	E	7	0.020
4221.761	4227.861	A	84	0.845
4229.037	4233.814	A	66	0.532
4234.035	4234.402	E	6	0.015
4235.211	4239.841	A	64	0.414
4239.794	4241.201	A	20	0.115
4241.942	4243.126	A	17	0.106
4243.349	4243.793	A	7	0.022
4244.830	4247.643	A	39	0.427
4247.791	4251.123	A	46	0.371
4251.937	4256.602	A	64	0.671
4257.046	4257.638	E	9	0.050
4257.860	4258.749	A	13	0.080
4259.045	4259.489	E	7	0.013
4259.859	4260.896	A	15	0.132
4261.562	4262.303	A	11	0.050
4262.451	4263.191	E	11	0.042
4264.376	4264.746	A	6	0.018
4265.634	4266.375	E	11	0.027
4266.967	4268.004	A	15	0.058
4269.188	4270.077	A	13	0.038
4270.373	4272.150	A	25	0.215
4272.372	4272.742	E	6	0.022
4272.951	4275.413	A	34	0.367
4276.010	4276.681	E	10	0.032
4277.129	4279.143	E	28	0.115
4279.367	4281.232	A	26	0.192
4281.381	4281.904	E	8	0.028
4282.127	4282.874	A	11	0.060
4283.097	4284.067	E	14	0.099
4284.366	4286.753	A	33	0.154
4287.574	4290.334	A	38	0.300
4290.856	4292.946	A	29	0.135
4293.543	4294.662	A	16	0.106
4295.408	4295.930	E	8	0.025
4296.229	4304.809	A	116	0.956
4304.809	4315.336	A	141	1.684
4315.562	4316.389	E	12	0.083
4317.367	4318.044	E	10	0.036
4318.270	4319.247	A	14	0.079
4320.149	4321.352	A	17	0.135

Continued, next page.

Table 19 *(continued)*

λ_{start}	λ_{end}	Type	Pixels	W_λ (Å)
4322.180	4327.820	A	76	0.729
4329.303	4329.833	E	8	0.024
4330.136	4330.818	A	10	0.043
4331.045	4333.393	E	32	0.119
4333.621	4334.000	E	6	0.013
4334.151	4336.196	E	28	0.198
4336.348	4340.135	A	51	1.133
4340.666	4343.998	E	45	0.504
4344.453	4346.346	E	26	0.219
4348.240	4349.982	E	24	0.101
4350.285	4352.331	A	28	0.133
4353.391	4353.770	E	6	0.016
4354.148	4356.420	A	31	0.141
4358.087	4360.663	A	35	0.159
4362.250	4364.006	A	24	0.107
4365.991	4366.602	A	9	0.025
4367.290	4368.129	A	12	0.061
4368.358	4369.046	E	10	0.058
4369.275	4369.962	A	10	0.033
4370.726	4371.489	A	11	0.036
4372.559	4375.231	A	36	0.284
4376.453	4376.834	E	6	0.020
4377.140	4377.598	A	7	0.017
4378.973	4384.165	A	69	0.505
4384.776	4385.463	A	10	0.042
4385.692	4386.456	E	11	0.058
4386.609	4387.296	A	10	0.037
4387.678	4392.031	A	58	0.307
4392.565	4395.772	A	43	0.422
4396.459	4397.376	E	13	0.045
4397.681	4398.827	A	16	0.082
4399.132	4401.423	A	31	0.189
4401.805	4402.721	E	13	0.072
4402.889	4409.814	A	91	0.765
4410.661	4411.508	A	12	0.029
4412.508	4413.201	E	10	0.041
4414.509	4415.740	A	17	0.157
4416.433	4418.510	A	28	0.195
4420.280	4420.973	A	10	0.033
4421.357	4424.282	A	39	0.196
4424.436	4425.975	A	21	0.104
4426.282	4426.667	E	6	0.018
4426.898	4427.591	A	10	0.035
4427.898	4428.360	E	7	0.027
4429.361	4430.900	A	21	0.113
4432.824	4436.594	A	50	0.278

Continued, next page.

Table 19 *(continued)*

λ_{start}	λ_{end}	Type	Pixels	W_λ (Å)
4436.748	4437.749	A	14	0.045
4440.053	4444.475	A	58	0.362
4445.018	4445.483	E	7	0.024
4446.259	4447.810	A	21	0.067
4448.042	4448.741	E	10	0.031
4448.973	4450.990	A	27	0.157
4452.154	4453.706	A	21	0.088
4453.861	4460.532	A	87	0.503
4461.075	4463.557	A	33	0.167
4463.868	4465.187	A	18	0.116
4465.729	4469.996	A	56	0.586
4470.151	4471.625	A	20	0.143
4473.409	4474.030	E	9	0.027
4474.417	4474.805	A	6	0.017
4475.549	4476.253	A	10	0.035
4476.644	4477.270	E	9	0.031
4478.599	4480.163	A	21	0.093
4483.525	4484.776	A	17	0.061
4485.480	4487.200	A	23	0.053
4487.591	4491.892	A	56	0.257
4492.830	4497.444	A	60	0.335
4498.147	4502.057	A	51	0.447
4503.230	4503.934	E	10	0.029
4506.123	4507.296	A	16	0.061
4507.531	4508.860	A	18	0.106
4509.817	4510.605	A	11	0.038
4510.763	4515.885	A	66	0.443
4516.595	4518.959	A	31	0.227
4519.511	4520.771	A	17	0.108
4521.560	4523.293	A	23	0.186
4524.160	4529.992	A	75	0.414
4530.544	4536.375	A	75	0.684
4538.582	4542.128	A	46	0.235
4543.783	4544.808	A	14	0.061
4544.812	4550.135	A	68	0.718
4550.294	4550.691	E	6	0.015
4551.724	4552.994	A	17	0.097
4553.232	4554.821	A	21	0.228
4555.219	4556.410	A	16	0.087
4556.648	4557.125	E	7	0.025
4558.079	4559.111	A	14	0.068
4559.985	4561.097	A	15	0.061
4561.335	4564.433	A	40	0.330
4565.068	4566.181	A	15	0.066
4567.134	4567.849	E	10	0.035
4570.550	4572.457	A	25	0.215

Continued, next page.

Table 19 *(continued)*

λ_{start}	λ_{end}	Type	Pixels	W_λ (Å)
4572.695	4573.965	E	17	0.089
4574.601	4574.998	A	6	0.016
4575.315	4575.951	E	9	0.030
4576.746	4577.699	E	13	0.061
4578.334	4578.890	A	8	0.021
4579.605	4580.479	A	12	0.038
4581.194	4584.292	A	40	0.201
4588.218	4588.618	E	6	0.149
4589.499	4590.460	A	13	0.068
4591.262	4592.864	A	21	0.124
4593.184	4598.710	A	70	0.467
4599.432	4608.002	A	108	0.638
4610.726	4611.847	A	15	0.049
4612.408	4614.090	A	22	0.115
4615.691	4617.053	A	18	0.073
4617.454	4617.934	E	7	0.026
4618.415	4619.456	A	14	0.071
4621.058	4621.619	E	8	0.025
4621.859	4623.381	A	20	0.080
4624.780	4629.947	A	65	0.323
4631.965	4634.630	A	34	0.138
4635.276	4641.816	A	82	0.451
4642.058	4652.716	A	133	0.759
4653.847	4657.479	A	46	0.227
4657.883	4658.287	E	6	0.015
4661.113	4664.343	A	41	0.149
4666.175	4669.105	A	37	0.197
4669.675	4670.489	A	11	0.031
4670.896	4671.628	E	10	0.031
4672.117	4675.454	A	42	0.143
4678.058	4682.779	A	59	0.240
4687.256	4688.070	A	11	0.032
4688.233	4688.640	A	6	0.015
4690.919	4691.733	A	11	0.033
4694.826	4696.536	E	22	0.062
4697.187	4697.594	E	6	0.012
4698.408	4698.977	A	8	0.020
4699.817	4701.705	A	24	0.103
4702.443	4703.675	A	16	0.078
4704.085	4710.732	A	82	0.421
4711.717	4716.396	A	58	0.249
4717.544	4718.283	A	10	0.026
4721.648	4723.700	A	26	0.073
4726.326	4730.511	A	52	0.276
4730.675	4731.907	A	16	0.075
4732.727	4734.451	A	22	0.091

Continued, next page.

Table 19 *(continued)*

λ_{start}	λ_{end}	Type	Pixels	W_λ (Å)
4735.354	4737.488	A	27	0.141
4739.812	4742.129	A	29	0.115
4742.460	4742.957	A	7	0.015
4744.282	4746.186	A	24	0.090
4751.402	4752.726	A	17	0.055
4753.554	4754.879	A	17	0.081
4755.044	4759.929	A	60	0.276
4760.591	4761.005	A	6	0.016
4761.171	4762.992	A	23	0.085
4763.737	4769.036	A	65	0.311
4771.105	4773.837	A	34	0.138
4775.907	4776.486	A	8	0.020
4779.301	4779.798	A	7	0.027
4779.857	4780.358	A	7	0.035
4781.443	4784.363	A	36	0.162
4785.031	4787.368	A	29	0.159
4787.785	4793.126	A	65	0.297
4796.214	4797.216	A	13	0.034
4797.633	4801.055	A	42	0.197
4804.393	4805.561	A	15	0.088
4806.479	4809.567	A	38	0.176
4809.984	4811.153	A	15	0.052
4814.825	4816.077	A	16	0.035
4818.747	4819.415	E	9	0.018
4823.087	4824.506	A	18	0.093
4828.178	4829.596	A	18	0.057
4830.765	4833.102	A	29	0.120
4836.921	4837.427	E	7	0.022
4838.353	4841.131	A	34	0.147
4842.057	4844.920	A	35	0.142
4847.529	4849.044	A	19	0.084
4854.938	4861.000	A	73	1.988
4861.252	4868.155	E	83	0.730
4868.576	4870.597	E	25	0.081
4870.849	4872.196	A	17	0.069
4872.786	4873.291	E	7	0.018
4873.543	4874.217	A	9	0.021
4875.175	4876.874	A	21	0.078
4877.043	4877.553	E	7	0.020
4877.723	4878.657	A	12	0.052
4878.912	4879.506	E	8	0.020
4880.101	4906.178	A	308	1.792
4906.518	4912.293	A	69	0.423
4912.463	4914.757	A	28	0.137
4939.779	4940.213	A	6	0.041
4941.168	4942.297	A	14	0.083

Continued, next page.

Table 19 *(continued)*

λ_{start}	λ_{end}	Type	Pixels	W_λ (Å)
4944.728	4946.725	A	24	0.125
4956.015	4956.797	E	10	0.037
4956.971	4958.012	A	13	0.095
4958.360	4958.968	E	8	0.028
4961.398	4961.833	A	6	0.017
4964.785	4966.782	A	24	0.127
4967.129	4973.467	A	74	0.377
4974.422	4979.284	A	57	0.300
4981.542	4982.410	A	11	0.031
4982.584	4983.105	A	7	0.021
4983.365	4984.060	A	9	0.030
4985.015	4985.883	A	11	0.060
4988.575	4989.704	A	14	0.045
4990.572	4991.614	A	13	0.052
4991.961	4992.916	E	12	0.056
4994.826	4995.782	E	12	0.038
4996.997	4997.431	A	6	0.020
5000.448	5001.061	E	8	0.034
5002.375	5002.813	E	6	0.016
5007.807	5008.595	E	10	0.044
5010.785	5011.485	E	9	0.052
5012.537	5012.975	E	6	0.023
5013.413	5014.289	A	11	0.035
5015.866	5018.844	A	35	0.537
5019.106	5019.895	E	10	0.041
5020.158	5020.946	E	10	0.035
5022.085	5022.786	A	9	0.030
5024.363	5025.063	A	9	0.030
5025.239	5025.764	A	7	0.019
5026.991	5028.479	A	18	0.066
5030.494	5031.107	A	8	0.023
5031.721	5032.247	E	7	0.029
5035.225	5036.364	A	14	0.066
5037.853	5039.692	A	22	0.092
5040.831	5041.707	A	11	0.045
5047.664	5049.766	A	25	0.121
5049.760	5050.467	A	9	0.037
5051.616	5052.147	A	7	0.025
5053.473	5054.091	A	8	0.024
5064.344	5065.493	A	14	0.060
5066.466	5067.791	A	16	0.063
5068.410	5069.294	A	11	0.046
5071.769	5072.830	A	13	0.068
5074.244	5075.039	A	10	0.032
5075.216	5075.658	A	6	0.020
5076.012	5076.542	A	7	0.028

Continued, next page.

Table 19 *(continued)*

λ_{start}	λ_{end}	Type	Pixels	W_λ (Å)
5098.325	5099.305	A	12	0.046
5101.175	5101.977	E	10	0.033
5103.135	5105.452	A	27	0.098
5107.144	5108.124	A	12	0.041
5109.727	5110.618	A	11	0.036
5111.063	5111.509	E	6	0.018
5114.449	5115.963	A	18	0.061
5120.417	5123.802	A	39	0.152
5124.604	5126.207	A	19	0.077
5126.474	5127.900	A	17	0.073
5128.523	5129.771	A	15	0.097
5130.572	5131.552	A	12	0.039
5136.629	5137.699	A	13	0.048
5138.055	5138.589	E	7	0.023
5138.946	5139.748	A	10	0.041
5140.174	5140.624	E	6	0.027
5143.322	5143.771	E	6	0.023
5146.379	5146.829	A	6	0.019
5147.729	5148.628	A	11	0.049
5152.585	5153.035	E	6	0.023
5162.118	5169.583	A	84	0.862
5170.392	5173.360	A	34	0.419
5180.465	5184.422	A	45	0.876
5184.872	5186.400	A	18	0.091
5187.030	5189.458	A	28	0.180
5191.516	5192.969	A	17	0.078
5194.965	5195.963	A	12	0.048
5196.689	5198.051	A	16	0.077
5198.323	5198.777	E	6	0.018
5200.956	5201.682	E	9	0.029
5201.954	5202.771	A	10	0.025
5203.587	5209.033	A	61	0.421
5222.284	5227.185	A	55	0.273
5227.548	5228.184	E	8	0.034
5229.545	5230.271	A	9	0.026
5232.359	5233.267	A	11	0.059
5234.083	5235.263	A	14	0.061
5240.525	5241.167	E	8	0.023
5246.759	5247.492	A	9	0.040
5249.693	5250.243	A	7	0.017
5254.368	5255.285	A	11	0.039
5255.743	5256.293	E	7	0.026
5261.611	5264.820	A	36	0.146
5268.029	5269.221	A	14	0.053
5269.587	5270.046	A	6	0.022
5271.054	5271.788	E	9	0.034

Continued, next page.

Table 19 *(continued)*

λ_{start}	λ_{end}	Type	Pixels	W_λ (Å)
5274.446	5276.372	A	22	0.099
5276.738	5277.563	E	10	0.047
5278.572	5279.305	E	9	0.028
5281.230	5282.239	A	12	0.055
5283.339	5284.348	A	12	0.045
5287.606	5288.993	A	16	0.048
5292.136	5293.984	A	21	0.079
5294.169	5303.043	A	97	0.537
5313.397	5317.095	A	41	0.275
5318.297	5322.734	A	49	0.196
5323.474	5324.490	A	12	0.054
5325.322	5328.743	A	38	0.169
5329.667	5330.314	A	8	0.023
5332.163	5333.272	A	13	0.048
5337.821	5338.568	E	9	0.031
5339.222	5339.783	A	7	0.023
5340.250	5340.997	A	9	0.025
5342.397	5343.891	A	17	0.051
5345.852	5346.319	A	6	0.019
5347.533	5350.241	A	30	0.109
5353.229	5353.789	A	7	0.018
5360.419	5361.913	A	17	0.056
5362.100	5363.313	A	14	0.065
5364.248	5371.998	A	84	0.514
5376.480	5377.974	A	17	0.050
5397.696	5398.355	E	8	0.026
5403.540	5404.671	A	13	0.054
5405.048	5406.368	A	15	0.072
5407.593	5408.065	A	6	0.015
5408.536	5411.741	A	35	0.120
5425.786	5426.917	E	13	0.048
5428.991	5430.028	A	12	0.048
5433.893	5435.118	A	14	0.044
5435.496	5437.569	A	23	0.082
5444.453	5445.596	A	13	0.046
5446.167	5447.215	A	12	0.049
5447.596	5448.167	E	7	0.026
5448.548	5449.595	E	12	0.034
5454.927	5455.879	A	11	0.039
5456.260	5457.022	E	9	0.027
5462.354	5463.496	A	13	0.047
5469.400	5471.304	A	21	0.062
5471.494	5475.589	A	44	0.176
5475.779	5477.303	A	17	0.102
5477.969	5481.873	A	42	0.222
5482.063	5483.873	A	20	0.073

Continued, next page.

Table 19 *(continued)*

λ_{start}	λ_{end}	Type	Pixels	W_λ (Å)
5486.539	5488.538	A	22	0.064
5489.746	5490.418	A	8	0.021
5490.611	5491.188	A	7	0.023
5492.245	5495.514	A	35	0.128
5496.764	5497.245	A	6	0.018
5507.435	5508.108	E	8	0.026
5512.146	5513.588	A	16	0.048
5528.009	5528.874	A	10	0.038
5531.565	5532.143	A	7	0.023
5533.296	5534.354	E	12	0.043
5535.315	5536.661	E	15	0.056
5553.889	5555.541	A	18	0.062
5556.609	5557.483	A	10	0.026
5557.678	5563.505	A	61	0.218
5565.448	5566.613	A	13	0.046
5568.944	5570.013	A	12	0.042
5571.955	5573.315	A	15	0.066
5576.715	5577.297	E	7	0.036
5588.272	5589.438	A	13	0.044
5593.518	5595.169	A	18	0.074
5598.471	5599.054	A	7	0.019
5600.224	5601.302	A	12	0.033
5602.087	5603.460	A	15	0.065
5614.837	5616.309	A	16	0.082
5617.093	5621.115	A	42	0.150
5623.469	5625.234	A	19	0.084
5625.626	5626.215	A	7	0.018
5626.607	5627.195	A	7	0.018
5632.688	5636.513	A	40	0.152
5636.807	5637.886	A	12	0.036
5655.024	5655.520	A	6	0.020
5657.897	5658.690	A	9	0.037
5660.870	5661.464	A	7	0.020
5661.959	5663.545	A	17	0.067
5684.945	5685.440	E	6	0.016
5697.131	5697.824	A	8	0.024
5698.815	5699.607	A	9	0.023
5700.301	5702.184	A	20	0.084
5710.775	5711.476	A	8	0.025
5727.291	5727.792	E	6	0.016
5751.915	5752.416	A	6	0.018
5752.916	5755.018	A	22	0.076
5780.313	5780.919	E	7	0.023
5781.223	5781.830	E	7	0.023
5784.662	5785.269	A	7	0.021
5789.820	5791.540	A	18	0.050

Continued, next page.

Table 19 *(continued)*

λ_{start}	λ_{end}	Type	Pixels	W_λ (Å)
5803.069	5807.317	A	43	0.193
5807.924	5809.138	A	13	0.037
5815.711	5816.318	A	7	0.017
5853.665	5854.278	A	7	0.021
5856.424	5858.876	A	25	0.097
5885.752	5889.330	A	36	1.558
5890.249	5891.986	E	18	0.270
5892.292	5895.358	A	31	1.387
5896.176	5898.118	E	20	0.260
5908.759	5909.275	A	6	0.018
5982.859	5984.110	A	13	0.036
5995.999	5998.397	A	24	0.080
6007.887	6008.930	A	11	0.032
6019.670	6021.674	A	20	0.085
6021.885	6022.517	A	7	0.020
6040.967	6041.811	A	9	0.028
6054.884	6056.465	A	16	0.056
6102.146	6103.425	A	13	0.051
6113.656	6114.828	E	12	0.035
6121.115	6122.714	A	16	0.053
6134.756	6135.289	E	6	0.014
6140.830	6142.322	A	15	0.073
6142.535	6143.281	E	8	0.022
6145.945	6146.691	E	8	0.026
6147.756	6150.527	E	27	0.124
6158.233	6159.957	E	17	0.068
6223.731	6225.255	E	15	0.049
6238.980	6239.961	E	10	0.038
6248.348	6249.873	E	15	0.048
6328.421	6329.303	A	9	0.036
6342.526	6343.958	A	14	0.051
6345.501	6346.603	E	11	0.046
6347.154	6348.697	E	15	0.056
6368.314	6368.872	E	6	0.018
6369.540	6371.657	E	20	0.093
6371.879	6372.771	E	9	0.040
6378.676	6379.345	E	7	0.022
6431.042	6432.379	E	13	0.054
6433.271	6433.939	E	7	0.026
6437.976	6439.667	A	16	0.055
6451.618	6452.520	E	9	0.025
6455.903	6456.805	A	9	0.027
6457.143	6458.271	E	11	0.047
6496.042	6497.621	A	15	0.075
6499.649	6500.890	A	12	0.043
6514.650	6515.905	E	12	0.044

Continued, next page.

Table 19 *(continued)*

λ_{start}	λ_{end}	Type	Pixels	W_λ (Å)
6516.476	6517.617	E	11	0.041
6537.355	6537.926	E	6	0.016
6549.678	6550.248	E	6	0.019
6553.215	6554.584	E	13	0.045
6555.041	6561.772	A	60	2.233
6562.000	6570.215	E	73	1.723
6597.331	6598.022	A	7	0.020
6613.371	6614.987	E	15	0.063
6624.334	6625.719	E	13	0.046
6632.990	6634.144	A	11	0.030
6704.514	6709.417	A	43	0.385
6747.423	6748.723	E	12	0.044
6755.457	6756.638	E	11	0.038
6789.360	6790.188	E	8	0.029
6793.495	6794.204	E	7	0.020
6795.621	6796.330	E	7	0.020
8046.580	8048.664	E	16	0.061
8084.364	8085.198	A	7	0.032
8086.448	8087.282	A	7	0.030
8111.314	8112.286	A	8	0.031
8128.956	8130.067	A	9	0.045
8397.259	8398.126	E	7	0.032
8411.277	8413.444	E	16	0.108
8419.226	8419.948	E	6	0.021
8425.729	8427.318	E	12	0.076
8433.533	8436.712	E	23	0.179
8438.591	8440.470	E	14	0.063
8443.649	8447.551	A	28	0.198
8464.459	8465.471	E	8	0.031
8466.049	8470.240	E	30	0.146
8474.432	8475.299	A	7	0.024
8493.363	8496.109	A	20	0.200
8496.398	8499.288	E	21	0.957
8537.316	8540.418	A	22	0.377
8540.713	8550.020	E	64	2.279
8597.729	8598.615	E	7	0.028
8603.933	8604.966	E	8	0.031
8657.571	8660.422	A	20	0.303
8660.722	8668.821	E	55	1.845
8674.371	8675.722	E	10	0.046
8676.771	8677.521	A	6	0.029
8681.722	8683.672	E	14	0.070
8685.172	8686.671	A	11	0.048
8688.472	8690.121	E	12	0.053
8712.771	8713.822	E	8	0.035
8751.322	8752.822	E	11	0.047

Continued, next page.

Table 19 *(continued)*

λ_{start}	λ_{end}	Type	Pixels	W_λ (Å)
8754.772	8755.823	A	8	0.031
8804.497	8805.715	E	9	0.037
8822.764	8825.808	E	21	0.117
8837.528	8839.964	E	17	0.097
8869.952	8871.019	A	8	0.032

REFERENCES

Basri, G. and Bertout, C. 1989, *Ap. J.*, **341**, 340.

Bastian, U. and Mundt, R. 1985, *Astr. Ap.*, **144**, 57.

Bechis, K. P. and Lo, K. Y. 1975, *Ap. J.*, **201**, 118.

Cabrit, S., Edwards, S., Strom, S. E., and Strom, K. M. 1990, *Ap. J.*, **354**, 687.

Cantó, J., Rodríguez, L. F., Calvet, N., and Levreault, R. H. 1984, *Ap. J.*, **282**, 631.

Carr, J., Harvey, P. M., and Lester, D. F. 1986, *Bull. AAS*, **18**, 1026.

Covino, E., Terranegra, L., Vittone, A. A., and Russo, G. 1984, *Astron. J.*, **89**, 1868.

Croswell, K., Hartmann, L., and Avrett, E. H. 1987, *Ap. J.*, **312**, 227.

Edwards, S. and Snell, R. L. 1982, *Ap. J.*, **261**, 151.

Eislöffel, J., Hessman, F. V., and Mundt, R. 1990, *Astr. Ap.*, **232**, 70.

Elias, J. 1978, *Ap. J.*, **224**, 453.

Finkenzeller, U. and Jankovics, I. 1984, *Astr. Ap. Suppl.*, **57**, 285.

Finkenzeller, U. and Mundt, R. 1984, *Astr. Ap. Suppl.*, **55**, 109.

Goodrich, R. W. 1987, *Pub. A.S.P.*, **99**, 116.

Graham, J. A. and Frogel, J. A. 1985, *Ap. J.*, **289**, 331.

Grasdalen, G. L. 1973, *Ap. J.*, **182**, 781.

Gray, D. F. 1976, *The Observation and Analysis of Stellar Photospheres*, (New York: Wiley).

Hartigan, P., Kenyon, S. J., Hartmann, L., Strom, S. E., Edwards, S., Welty, A. D., and Stauffer, J. 1991, in preparation.

Hartmann, L., Edwards, S., and Avrett, E. 1982, *Ap. J.*, **261**, 279.

Hartmann, L., Hewett, R., Stahler, S., and Mathieu, R. D. 1986, *Ap. J.*, **309**, 275.

Hartmann, L. and Kenyon, S. J. 1985, *Ap. J.*, **299**, 462 (HK1).

Hartmann, L. and Kenyon, S. J. 1987a, *Ap. J.*, **312**, 243 (HK2).

Hartmann, L. and Kenyon, S. J. 1987b, *Ap. J.*, **322**, 393 (HK3).

Hartmann, L., Kenyon, S. J., Hewett, R., Edwards, S., Strom, K. M., Strom, S. E., and Stauffer, J. R. 1989, *Ap. J.*, **338**, 1001.

Hartmann, L. and MacGregor, K. B. 1982, *Ap. J.*, **259**, 180.

Herbig, G. H. 1958, *Ap. J.*, **128**, 259.

Herbig, G. H. 1960, *Ap. J. Suppl.*, **6**, 337.

Herbig, G. H. 1966, *Vistas in Astronomy, Vol.* **8**, ed. A. Beer and K. A. Strand (Oxford: Permagon), p. 109.

Herbig, G. H. 1977, *Ap. J.*, **223**, 213.

Herbig, G. H. 1989, *ESO Workshop on Low Mass Star Formation and Pre-Main Sequence Objects*, ed. Reipurth, B. (ESO) p. 233.

Herbig, G. H. and Bell, K. R. 1988, *Lick Observatory Bull.*, No. 1111.

Hessman, F. V., Eislöffel, J., Mundt, R., Hartmann, L. W., Herbst, W., and Krautter, J. 1991, *Ap. J.*, in press.

Hippelein, H. H. 1973, *Astr. Ap.*, **25**, 59.

Hoffleit, D. 1939, *Harv. Bull.*, No. 911, p. 41.

Hoffleit, D. and Jaschek, C. 1982, *The Bright Star Catalogue*, (Yale University Observatory).

Jacoby, G. H., Hunter, D. A., and Christian, C. A. 1984, *Ap. J. Suppl.*, **56**, 257.

Kenyon, S., and Hartmann, L. 1987, *Ap. J.*, **323**, 714.

Kenyon, S., and Hartmann, L. 1988, *Pulsation and Mass Loss in Stars* ed. R. Stalio and L.A. Willson (Dordrecht: Kluwer), p. 133.

Kenyon, S. J., Hartmann, L., Imhoff, C. L., and Cassatella, A. 1989, *Ap. J.*, **344**, 925.

Kenyon, S. J., Hartmann, L., and Hewett, R. 1988, *Ap. J.*, **325**, 231 (KHH).

Kukarkin, B. V., Kholopov, P. N., Efremov, Y. N., Kukarkina, N. P., Kurochkin, N. E., Medvedeva, G. I., Perova, N. M., Fedorovich, V. P., and Frovlov, M. S. 1969, *General Catalog of Variable Stars* (Moscow: Academy of Science of USSR Press).

Kwan, J. and Tademaru, E. 1988, *Ap. J.*, **332**, L41.

Lada, C. J. 1985, *Ann. Rev. Astron. Astrophys.*, **23**, 267.

Larson, R. B. 1972, *M.N.R.A.S.*, **157**, 121.

Larson, R. B. 1980, *M.N.R.A.S.*, **190**, 321.

Leinert, Ch. and Haas, M. 1987, *Astr. Ap. (Letters)*, **182**, L47.

Levreault, R. M. 1988, *Ap. J. Suppl.*, **67**, 283.

Lo, K. Y, and Bechis, K. P. 1974, *Ap. J. (Letters)*, **190**, L125.

Lynden-Bell, D. and Pringle, J. E. 1974, *M.N.R.A.S.*, **168**, 603 (LBP).

Miller, G. E. and Scalo, J. M. 1979, *Ap. J. Suppl.*, **41**, 513.

Minn, Y. K. and Greenberg, J. M. 1973, *Astr. Ap.*, **22**, 13.

Moore, C. E. 1959, *A Multiplet Table of Astrophysical Interest*, (TN 36, PB 151395, Department of Commerce, Clearing House for Federal and Scientific Information, Springfield, VA).

Moore, C. E., Minnaert, M. G. J., and Houtgast, J. 1966, *NBS Monog. 61, The Solar Spectrum* 2935 Å *to* 8770 Å, (Washington, DC: Department of Commerce).

Mould, J. R., Hall, D. N. B., Ridgway, S. T., Hintzen, P., and Aaronson, M. 1978, *Ap. J. (Letters)*, **222**, L123.

Mundt, R., Stocke, J., Strom, S. E., Strom, K. M., and Anderson, E. R. 1985, *Ap. J. (Letters)*, **297**, L41.

Natta, A., Giovanardi, C., and Palla, F. 1988, *Ap. J.*, **332**, 921.

Payne-Gaposchkin, C. H. 1957, *The Galactic Novae*, (Amsterdam: North Holland Publ. Co.), p. 32.

Poetzel, R., Mundt, R., and Ray, T. P. 1989, *Astr. Ap. (Letters)*, **224**, L13.

Pringle, J. E. 1989, *M.N.R.A.S.*, **236**, 107.

Pudritz, R. E. and Norman, C. A. 1983, *Ap. J.*, **274**, 677.

Pudritz, R. E. and Norman, C. A. 1986, *Ap. J.*, **301**, 571.

Robinson, L. J. and Harwood, M. 1971 *Inf. Bull. Var. Stars*, No. 568.

Shakura, N. I. and Sunyaev, R. A. 1973, *Astr. Ap.*, **24**, 337.

Shanin, G. I. 1979, *Astr. Zh.*, **56**, 288.

Shu, F. H., Adams, F. C., and Lizano, S. 1987, *Ann. Rev. Astron. Astrophys.*, **25**, 23.

Shu, F. H., Lizano, S., Ruden, S. P., and Najita, J. 1988, *Ap. J.*, **328**, L19.

Simon, T., and Joyce, R. R. 1988, *Pub. A.S.P.*, **100**, 1549.

Smith, H. A., Thronson, H. A., Lada, C. J., Harper, D. A., Loewenstein, R. F., and Smith, J. 1982, *Ap. J.*, **258**, 170.

Stocke, J., *et al.* 1988, *Ap. J. Suppl.*, **68**, 229.

Strom, S. E., Strom, K. M., Yost, J., Carrasco, L., and Grasdalen, G. 1972, *Ap. J.*, **173**, 353.

Swenson, J. W., Benedict, W. S., Del Bouille L., and Roland, G. 1970, *The Solar Spectrum from* λ7498 *to* λ12016 (Liège: Société Royale des Sciences de Liège).

Tonry, J. and Davis, M. 1979, *Astron. J.*, **84**, 1511.

Torbett, M. V. 1984, *Ap. J.*, **278**, 318.

Uchida, Y. and Shibata, K. 1985, *Pub. Ast. Soc. Japan*, **37**, 515.

Vogel, S. N. and Kuhi, L. V. 1981, *Ap. J.*, **245**, 960.

Wachmann, A. A. 1939, *Beob. Zirk.*, **21**, 12.

Wachmann, A. A. 1954, *Zs. f. Ap.*, **35**, 74.

Weintraub, D. A., Sandell, G., and Duncan, W. D. 1989, *Ap. J.*, **340**, L69.

Welin, G. 1971a, *Astr. Ap.*, **12**, 312.

Welin, G. 1971b, *Inf. Bull. Var. Stars*, No. 581.

Welty, A. D., Strom, S. E., and Grasdalen, G. L. 1988, *Bull. AAS*, **20**, 1090.

Welty, A. D., Strom, S. E., Strom, K. M., Hartmann, L. W., Kenyon, S. J., Grasdalen, G. L., and Stauffer, J. R. 1990, *Ap. J.*, **349**, 328.

Wenzel, W. 1963, *Mitt. Ver. Sterne*, No. 730.

Wu, C.-C., *et al.* 1983, *IUE NASA Newsletter*, No. 22.